

2017-02-21

Novel Photovoltaic Devices using Ferroelectric Material and Colloidal Quantum Dots

Young Hun Paik
y.paik@miami.edu

Follow this and additional works at: https://scholarlyrepository.miami.edu/oa_dissertations

Recommended Citation

Paik, Young Hun, "Novel Photovoltaic Devices using Ferroelectric Material and Colloidal Quantum Dots" (2017). *Open Access Dissertations*. 1788.
https://scholarlyrepository.miami.edu/oa_dissertations/1788

This Open access is brought to you for free and open access by the Electronic Theses and Dissertations at Scholarly Repository. It has been accepted for inclusion in Open Access Dissertations by an authorized administrator of Scholarly Repository. For more information, please contact repository.library@miami.edu.

UNIVERSITY OF MIAMI

NOVEL PHOTOVOLTAIC DEVICES USING FERROELECTRIC MATERIAL AND
COLLOIDAL QUANTUM DOTS

By

Young Hun Paik

A DISSERTATION

Submitted to the Faculty
of the University of Miami
in partial fulfillment of the requirements for
the degree of Doctor of Philosophy

Coral Gables, Florida

May 2017

©2017

Young Hun Paik

All Rights Reserved

UNIVERSITY OF MIAMI

A dissertation submitted in partial fulfillment of
the requirements for the degree of
Doctor of Philosophy

NOVEL PHOTOVOLTAIC DEVICES USING FERROELECTRIC MATERIAL AND
COLLOIDAL QUANTUM DOTS

Young Hun Paik

Approved:

Sung Jin Kim, Ph.D.
Assistant Professor of Electrical
and Computer Engineering

Michael Wang, Ph.D.
Professor of Electrical
and Computer Engineering

Marc Knecht, Ph.D.
Associate Professor of Chemistry

Onur Tigli, Ph.D.
Assistant Professor of Electrical
and Computer Engineering

Fulin Zuo, Ph.D.
Professor of Physics

Guillermo Prado, Ph.D.
Dean of the Graduate School

PAIK, YOUNG HUN
Novel Photovoltaic Devices using Ferroelectric Material
and Colloidal Quantum Dots

(Ph.D., Electrical and Computer Engineering)
(May 2017)

Abstract of a dissertation at the University of Miami.

Dissertation supervised by Professor Sung Jin Kim.
No. of pages in text. (151)

As the global concern for the financial and environmental costs of traditional energy resources increases, research on renewable energy, most notably solar energy, has taken center stage. Many alternative photovoltaic (PV) technologies for ‘the next generation solar cell’ have been extensively studied to overcome the Shockley-Queisser 31% efficiency limit as well as tackle the efficiency vs. cost issues.

This dissertation focuses on the novel photovoltaic mechanism for the next generation solar cells using two inorganic nanomaterials, nanocrystal quantum dots and ferroelectric nanoparticles. Lead zirconate titanate (PZT) materials are widely studied and easy to synthesize using solution based chemistry. One of the fascinating properties of the PZT material is a Bulk Photovoltaic effect (BPVE). This property has been spotlighted because it can produce very high open circuit voltage regardless of the electrical bandgap of the materials. However, the poor optical absorption of the PZT materials and the required high temperature to form the ferroelectric crystalline structure have been obstacles to fabricate efficient photovoltaic devices.

Colloidal quantum dots also have fascinating optical and electrical properties such as tailored absorption spectrum, capability of the bandgap engineering due to the wide range of material selection and quantum confinement, and very efficient carrier dynamics called

multiple exciton generations. In order to utilize these properties, many researchers have put numerous efforts in colloidal quantum dot photovoltaic research and there has been remarkable progress in the past decade. However, several drawbacks are still remaining to achieve highly efficient photovoltaic device. Traps created on the large surface area, low carrier mobility, and lower open circuit voltage while increasing the absorption of the solar spectrum is main issues of the nanocrystal based photovoltaic effect.

To address these issues and to take the advantages of the two materials, this dissertation focused on material synthesis for low cost solution process for both materials, fabrication of various device structures and electrical/optical characterization to understand the underlying physics. We successfully demonstrated lead sulfide quantum dots (PbS QDs) and lead zirconate titanate nanoparticles (PZT NPs) in an aqueous solution and fabricated a photosensitive device. Solution based low-temperature process was used to fabricate a PbS QD and a PZT NP device. We exhibited a superior photoresponse and ferroelectric photovoltaic properties with the novel PZT NP device and studied the physics on domain wall effect and internal polarity effect.

PZT NP was mainly investigated because PZT NP device is the first report as a photosensitive device with a successful property demonstration, as we know of. PZT's crystalline structure and the size of the nanocrystals were studied using X-ray diffraction and TEM (Transmission electron microscopy) respectively. We observed < 100 nm of PZT NPs and this result matched with DLS (dynamic light scattering) measurement. We fabricated ferroelectric devices using the PZT NPs for the various optical and electrical characterizations and verified ferroelectric properties including ferroelectric hysteresis

loop. We also observed a typical ferroelectric photovoltaic effect from a PZT NP based device which was fabricated on an ITO substrate.

We synthesized colloidal quantum dots (CQD) with the inexpensive soluble process. Fabricated PbS QD was used for the hybrid device with PZT thin films. J-V measured and the result shows superior open circuit voltage characteristics compared to conventional PbS QD PV devices, and resulting the improvement of the solar cell efficiency. This Ferroelectrics and Quantum Dots (FE-QDs) device also the first trial and the success as we know of.

To my loving wife Julie
and
my daughters Liz (Jaeui) and Bridget (Jaewan)

ACKNOWLEDGEMENTS

I would like to thank all the people who have contributed to this work. I wish to express my gratitude to my advisor, Professor Sung Jin Kim, for his scientific guidance and encouragement throughout my Ph.D. program. I appreciate his guidance on how to do research and write papers.

I thank Professors Wang, Tigli, Knecht, and. Zuo for serving on my Ph.D. dissertation committee and for their valuable comments and suggestions.

I also thank Dr. Siddarth Rawal, Dr. Joshua Cohn, Dr. Jason Lee and Dr. Nicholas Merrill for their suggestions about my research and their advice.

I would also like to thank all the lab members, Hossein Shokri, Hui Lu, Kai Shen, Dr. Guomin Jiang, and Dr. Behzad Dogahe, Sukru U. Senveli, Alperen Toprak, and Randil Gajasinghe for their help over the beam years. Especially, I thank Hossein for the many discussions we had about scientific theories, experiment method, and ideas. Hossein is the source of many novel ideas.

A special thanks goes to Neal Ricks of Florida International University and Sarfaraz Beig for useful discussions and help with the work. In particular, I would like to thank my parents and father-in-law for their unconditional love and patience. Most of all, I miss my father in heaven. I am especially grateful to my wife, HyeGyoung (Julie), for her patience, enthusiastic support, and continuous understanding. My daughters, Liz Jaeui and Bridget Jaewan are a constant source of happiness. I am grateful for their support and their endless faith and love.

TABLE OF CONTENTS

LIST OF FIGURES.....	viii
LIST OF TABLES.....	xi
Chapter 1 Introduction	1
1.1. Background and Motivation.....	1
1.1.1 3 rd Generation Photovoltaics.....	1
1.1.2 Colloidal Quantum Dots.....	3
1.1.3 Ferroelectric Photovoltaics.....	4
1.2. Research Overview.....	7
1.3. Research Impact and Summary.....	8
1.4 Organization of the Dissertation.....	10
Chapter 2 Ferroelectricity.....	13
2.1 Ferroelectric Materials	14
2.1.1 Perovskite ABO ₃ Structure.....	17
2.1.2 P-E Hysteresis.....	21
2.1.3 Ferroelectric Domain and Domain Walls.....	23
2.1.4 Polarization Switching and Polarization-Electric Field Hysteresis Loops.....	25
2.2 Ferroelectric Photo Response	26
2.3 Perovskite PZT	32
2.3.1 Morphotropic Phase Boundary of PZT.....	32

Chapter 3 Quantum Dots.....	36
3.1 Quantum Dot Size Effect.....	36
3.1.1. QD Confinement.....	39
3.1.2. E_g Tunability of QD	40
3.1.3 Narrow Emission of QD	42
3.1.4 Photovoltaic Effect	43
3.1.5 Multiple Electron Generations (MEG).....	45
3.2 Colloidal Quantum Dots (CQD)	48
3.2.1. Advantages from CQD.....	48
3.2.2. PbS CQD.....	48
3.2.3. CQD Synthesis.....	51
3.3 Properties of PbS CQD	53
3.3.1. Material Properties of PbS CQD.....	54
3.3.2. Optical Properties of PbS CQD.....	55
3.3.3. Pb-Chalcogenide QDs for Photovoltaics.....	56
Chapter 4 Synthesis and Fabrication of Ferroelectric Thin Films and Nanoparticles	
.....	61
4.1 Fabrication Technique.....	62
4.2 Sol-Gel Method.....	66
4.3 Fabrication of PZT Sol-Gel Thin Film Devices.....	72
4.4 Fabricating PZT Nanoparticle Film Devices.....	75
4.5 Synthesis of PbS Quantum Dots.....	79
Chapter 5 Photovoltaic and Ferroelectric Properties of $\text{Pb}(\text{Zr}_{0.53}\text{Ti}_{0.47})\text{O}_3$ Thin Films	
under Dark and Illuminated Conditions.....	81
5.1 Overview.....	81
5.2 Background.....	81
5.3 Experiment.....	83

5.4 Results and Discussion	85
5.5 Conclusion	94
Chapter 6. Ferroelectric Devices using Lead Zirconate Titanate Nanoparticles.....	95
6.1 Overview.....	95
6.2 Background.....	95
6.3 Experiment.....	98
6.4 Results and Discussion	104
6.5 Conclusion	117
Chapter 7. Improvement of Efficiency of Ferroelectric PZT Photovoltaic Device with PbS Quantum Dots	118
7.1 Overview.....	118
7.2 Background.....	118
7.3 Experiment.....	120
7.4 Results and Discussion	126
7.5 Conclusion.....	135
Chapter 8. Summary and Future works.....	136
References.....	140

LIST OF FIGURES

Figure 1. 1 Principles of operation for a conventional solar cell and the ferroelectric alternative.....	6
Figure 1. 2 Overview of research.....	9
Figure 2. 1 Representation of the dipoles in a dielectric material placed in an electric field	16
Figure 2. 2 Perovskite ABO ₃ unit cell for PZT.....	19
Figure 2. 3 Schematic diagram of the phase transition in a ferroelectric material.....	20
Figure 2. 4 Hysteresis loop of a ferroelectric material.....	22
Figure 2. 5 Paraelectric polarization versus electric field.....	23
Figure 2. 6 Directions of tetragonal PZT ferroelectric polarization under Curie temperature.....	24
Figure 2. 7 Schematic diagram for the working principle of p-n junction and ferroelectric PV.....	29
Figure 2. 8 Band structure in dark conditions and under illumination of BFO film.....	31
Figure 2. 9 Perovskite structure from PZT atomic cells.....	33
Figure 2. 10 PbZrO ₃ -PbTiO ₃ phase diagram.....	34
Figure 3. 1 Density of states for electrons in bulk and various confined geometries.....	37
Figure 3. 2 (a) Typical room temperature band edge luminescence and absorption spectra for 3.5 nm CdSe crystallites (b) Emission maxima and sizes of quantum dots of different composition.....	41
Figure 3. 3 Typical measurements open-circuit voltage (V _{oc}), short-circuit current (J _{sc}), fill factor (FF).....	44
Figure 3. 4 Multiple exciton generation in CQDs.....	45
Figure 3. 5 QD synthetic apparatus employed in the preparation of CQDs.....	49
Figure 3. 6 Schematics of diagram of a general colloidal semiconductor quantum dot...50	50

Figure 3. 7 Absorption spectra of PbSe QDs as a function of nanocrystal diameter.....	56
Figure 4. 1 Schematic diagram of a typical laser deposition set-up.....	63
Figure 4. 2 Schematic diagram of MOCVD principle for the III-V semiconductors.....	65
Figure 4. 3 General schematic diagram of sol-gel formation and the resulting material and the devices in this thesis.....	68
Figure 4. 4 Spin coating method.....	73
Figure 4. 5 Cross section of the ferroelectric PZT capacitor.....	75
Figure 4. 6 Schematic diagram of the mechanism of PZT nanoparticle formation.....	77
Figure 4. 7 TEM image of final product from (a) PZT gel and (b) PZT sol after nanoparticle synthesis.....	78
Figure 5. 1 (a) PZT sol-gel synthesis method, (b) Sawyer-Tower circuit and peripheral equipment.....	84
Figure 5. 2 XRD pattern of sol-gel synthesized PZT(53:47) powder and PZT/FTO.....	86
Figure 5. 3 J–V characteristics and Schottky Junction of the ferroelectric FTO/PZT/Al devices.....	87
Figure 5. 4 (a) Photocurrent and (b) Energy band gap comparison of FTO/PZT/Al	89
Figure 5. 5 P-E hysteresis loop of FTO/PZT/Al capacitor.....	91
Figure 5. 6 Optical (a) transitivity, (b) absorption , and (c) plot of $[\alpha hv]^2$ vs. $h\nu$ in order to find energy bandgap of PZT.....	92
Figure 6. 1 Flow chart of sol-gel methods for bulk and nanoparticle PZT synthesis, and resulting Transmission Electron Microscopy (TEM) images.....	99
Figure 6. 2 Schematic diagram of the fabricated PZT device, and cross-sectional SEM images.....	103
Figure 6. 3 (a) XRD diffraction pattern of bulk PZT NPs (b) Measured DLS data and TEM images of (c) S2 and (d) S3 PZT NPs	105
Figure 6. 4 TEM images and SAED patterns of PZT NPs by different Zr and Ti ratio..	107
Figure 6. 5. Hysteresis of bulk-PZT-film and PZT NPs.....	109

Figure 6. 6 Displacement current of (a) bulk PZT film on ITO substrate, and (b) PZT NPs.....	110
Figure 6. 7 Measured photo response from PZT NPs devices (S2 and 3).....	112
Figure 6. 8 The dependence of the photo-current and photo-voltage on the light intensity.....	113
Figure 6. 9 Leakage current of bulk PZT film (S1), large size PZT NPs (S2) and small size PZT NPs (S3) MFM devices.....	114
Figure 6. 10 J-V characteristics of fabricated devices under light illumination.....	115
Figure. 7. 1 A cartoon that explain the brief process of colloidal synthesis for PbS QDs.....	122
Figure. 7. 2 Schematic of the standard layer-by-layer spin-coating process.....	124
Figure. 7. 3 Schematic of the Sawyer-Tower measurement system for P-E hysteresis...	125
Figure 7. 4 (a) XRD comparison between PZT crystalline powder and the thin film on ITO/glass substrate, (b) P-E Hysteresis form PZT thin film on ITO substrate.....	128
Figure 7. 5 (a) Absorption spectra of PbS QDs, where the QD absorption peak is located at 1023 nm. (b) TEM image of PbS QDs.....	128
Figure 7. 6 Device structure cartoons and Cross-sectional SEM images of (a) ITO/PZT/PbS/Al hybrid device, and (b) single layer PZT on ITO substrate, respectively	130
Figure 7. 7 J-V characterization of (a) PZT:PbS-QDs hybrid devices, and that of PZT, PbS for comparison. (b) J-V hysteresis of PZT:PbS-QDs devices, when the polarization is up and down.....	132
Figure 7. 8 External quantum efficiency (EQE) and absorption spectra for the (a) PZT:PbS-QDs hybrid and (b) single layer PZT devices respectively.....	134

LIST OF TABLES

Table 1 Device performance for single and hybrid solar cells and respective reference devices.....	133
--	-----

Chapter 1: Introduction

1.1 Background and Motivation

1.1.1 3rd Generation Photovoltaics

Since the silicon-based solar cell was demonstrated in 1839 by Edmond Becquerel, solar cells (also called a photovoltaic cell) have been developed a lot in efficiency and in understanding its mechanism. Today's commercial photovoltaic (PV) technology is categorized as crystalline silicon (1st generation) and thin film (2nd generation). The 1st generation cells, which are monocrystalline and multi-crystalline Si cells, are the most efficient of the mainstream PV technologies and accounted for about 86 % of PV produced in 2010. [1] The 2nd generation solar cells are structured using an extremely thin layer of semiconductor material made of amorphous silicon (a-Si), copper indium diselenide (CIS), copper indium gallium diselenide (CIGS), or cadmium telluride (CdTe). In the 2nd generation category, multi-junction PV cell is also included. These cells use multiple thin film layers of semiconductor material (usually group III and V elements) to expand their absorption spectrum. Combined with other techniques, these cells have demonstrated the highest power conversion efficiencies exceeding 40 %. Numerous structures and materials continue to be investigated using emerging technologies for the 3rd generation PV. The concept of the 3rd generation cells are either very high efficiency (exceed Shockley-Queisser 31% limit) or very low cost PV cells. In the low cost approach, there has been remarkable progress in polymer PV and dye sensitized solar cell (DSSC). [2] Those organic based PV devices utilize organic materials (dyes, conjugated

polymers, and molecular semiconductors) as light harvesters. These can be easily fabricated using an all solution process that lowers the production cost. The resulting cells are lightweight, low cost, and flexible. The highest reported power conversion efficiency (PCE) of polymer PV and DSSC are 12% (Heliatek GmbH, Germany) and 14.1% (EPFL, Switzerland), respectively. Unfortunately, given the current material limitations, organic solar cells suffer from short operation lifetimes due to vulnerability to oxygen, moisture, and UV irradiation. In addition, organic materials have limited spectral sensitivity and low carrier mobility.

In the inorganic material PV researched for the 3rd generation, several novel concepts have been developed to minimize losses and expand the absorption spectrum for highly efficient PV cells. For example, a hot carrier solar cell uses the selective contact to extract the hot (energetic) charge carriers before significant thermalization occurs. Multi-band (intermediate band) solar cells consist of an intermediate band or bands between the valence band and conduction band. This process enlarges the absorption to the long wavelength. Thus, it enables the formation of a highly efficient photovoltaic device. Multiple exciton generations (MEG) in nanocrystals quantum dots (QDs) has the potential to provide multiple carriers from a single absorbed photon (and to minimize losses due to thermalization), and Nozik's and Klimov's groups have proven the existence of the MEG phenomena using femto second laser spectroscopy. [3, 4] Also there are several demonstrations of carrier multiplications in electrical currents. [5, 6] However, because of the quantum confined structure of the nanocrystals, it is difficult to extract the charges created by multiple exciton generations. A recently proposed mechanism to

overcome this drawback is a 'strong internal electric field' in the device to extract the multiple excitons from the quantum dots, which is one of the main idea of this thesis.

1.1.2 Colloidal Quantum Dots

Over the past few decades, researchers have put in lots of efforts in colloidal quantum dot (or nanocrystal) research. Because of the small size of these nanocrystals, the wave function of an electron is confined in three dimensions and the electron in the nanocrystals exhibits quantum behavior governed by Schrödinger's equations. As should be expected, the confinement energy and resulting changes in the electrical and optical properties are also modified by changes in the shape of the nanocrystals. Semiconductor nanocrystals appear to be ideally suited as light absorbing materials due to their size-tunable band gap to cover the entire solar spectrum and the possibility of multiple exciton generations. Among QDs, Colloidal quantum dot (CQD) solar cells have advantages in low cost and scalable solution based fabrication processes, as well as the large variety of available materials too.

In spite of these great advantages from CQDs, there are still a few drawbacks to overcome. One obstacle is that CQDs can have surface defects which can affect the recombination of electrons and holes by acting as temporary "traps". [7] Because of these traps, mid-gap states can capture both electrons and holes, accelerating recombination. Other main obstacles that limit power conversion efficiency for the next

generation solar cells are the inefficient charge transfer and transport, and the low open circuit voltage (V_{oc}) level when CQD is fabricated as a PV device, regardless of the type of junctions used. [8] Generally, this is understood to be due to Fermi level pinning at the mid-gap states, which are formed by a large number of surface states associated with defects on the CQD surface. [9] QD is a semiconductor material which has the lower energy band gap, in the case of Si, 1.1 eV and PbS, 0.41 eV in the bulk state. A strategic approach to overcome trap effect, lossless charge transfer / transport or a large V_{oc} is the keys for the success of next generation solar cell.

1.1.3 Ferroelectric Photovoltaics

Ferroelectric materials are characterized by a spontaneous electric polarization that can be switched using an external electric field. Because of the sensitivity to external stimuli such as stress, strain, temperature or electric field, ferroelectrics have been used in sensors and actuators. Another interesting property of the ferroelectric material is the bulk photovoltaic effect (BPVE). Unlike in the p-n junction solar cell, steady state photocurrent can exist in a homogeneous medium under uniform illumination. BVPE has several unique features such as an extremely large photovoltage which is 'above the materials band gap' and also a photocurrent proportional to the polarization magnitude.

[10] Since the first observation of BVPE in the 1950s, it has not been extensively studied because of the poor photocurrent generation. But BPVE has seen a resurgent interest recently, especially in ferroelectric thin films, because of its possibility of a higher open

circuit voltage that exceeds above the band gap. Some of the well-known BPVE ferroelectric materials are lead lanthanum zirconate titanate (PLZT), lead zirconate titanate (PZT) and bismuth ferrite (BFO).

Ferroelectrics also have a few drawbacks to overcome. Ferroelectric PLZT, PZT or BFO are relatively high band gap (> 2.5 eV) materials. Thus, low absorption in the solar spectrum limits the efficiency of ferroelectric PV cells. Another shortcoming of ferroelectric materials are the very small short circuit currents due to the low photoconductivity. This is usually understood that the most of the ferroelectric materials are insulators.

Recently, ferroelectrics are attracted due to its above bandgap properties. The principles of above band gap open circuit voltage from ferroelectric PV is described in Figure 1.1.(b). This shows the ferroelectric materials can generate high open circuit voltage by ordering the domain structure as reported by Yang et al. [10]

The domain wall works similar to a classical p-n junction. (Figure 1.1.(a)) Owing to the abrupt change of polarization at the domain walls, the divergence of the polarization is non-zero ($\nabla \cdot \mathbf{P} \neq 0$), thus, an imbalance of charges develop at the domain walls. The charges induce an electrostatic potential drop across the domain wall, and this potential offset causes a band bending across the domain wall. Because of the few nm of domain wall thickness, it has a very strong local electric field and efficient charge separation. In contrast, photo generated charge carriers are localized and tightly bound in the bulk of ferroelectric domain. It causes recombination before electrons are transported to the other side of a domain wall. This process limits the photocurrent, but the open circuit voltage increases linearly with the number of domain walls. Another very interesting recent

report shows that a bulk hetero junction polymer solar cell incorporated with ferroelectric polymer exhibits enhanced performance due to the assisted electric field from nanostructured ferroelectric polymers. [11-13] Those recent demonstrations show that novel device structure using ferroelectric domains and proper light harvesting materials will enable multiple degrees of freedom for controlling the photovoltaic effect and enabling efficient next generation PV.

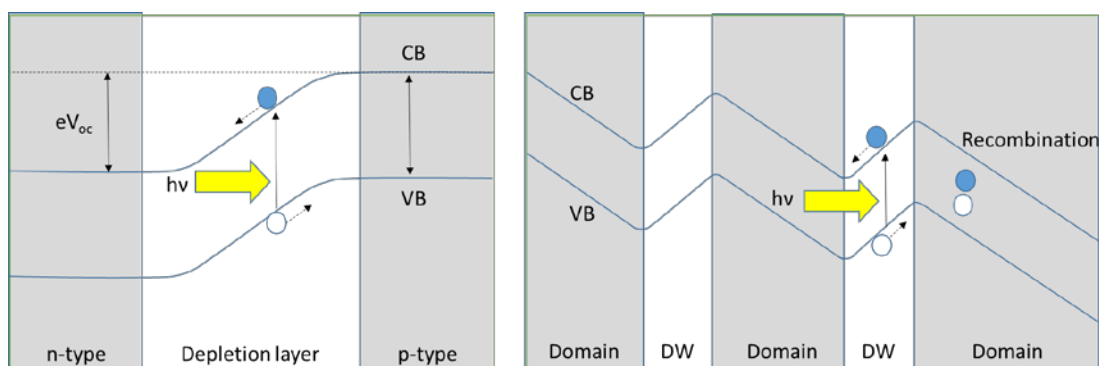


Figure 1.1 Principles of operation for a conventional solar cell and the ferroelectric alternative. (a), Band diagram of a conventional semiconductor p–n junction, showing the conduction band (CB), valence band (VB), band gap (E_g) and open-circuit voltage (V_{oc}). Here, $h\nu$ is the energy of the incident photon and e is the elementary electric charge. (b), In the ferroelectric domain, band bending occurs across the domain wall (DW). The directions of electric polarization (P) are shown by arrows. Reproduced with permission from ref [14]. Copyright © 2010 Nature Publishing Group

1.2 Research Overview

The goal of this thesis is to explore a novel mechanism for next generation solar cells based on hybrid devices using both semiconductor nanocrystals and ferroelectric materials by combining their strengths and minimizing their drawbacks. To accomplish this goal, material synthesis, measurement properties, novel device fabrication, and characterizations are required. We focus on following research tasks: 1) Novel synthesis approach using low cost solution process fabrication for nanocrystals and ferroelectric nanostructures, 2) All solution based nanofabrication for the proposed device to take advantages of quantum dots and ferroelectric materials and 3) Various optical and electrical test and analyses to understand the mechanism of novel hybrid photovoltaic devices. And we showed the successful outcomes which contributed to building a novel photovoltaic mechanism and providing the solutions to overcome the obstacles that cause losses in the energy conversion process.

There is a need for new solar energy paradigms that offer low cost and high conversion efficiency. Nanocrystals offer tailored optical and electrical properties. Ferroelectric materials can create a strong internal electric field resulting in high open circuit voltage. By combining the strengths of these approaches, one can achieve the goal of low cost and high conversion efficiency. Still there were several hurdles to outcomes when we started this research: 1) the fundamental understanding of novel photovoltaic devices such as ferroelectricity assisted charge transfer and transport mechanisms. 2) A device model for the new PV concept established using various electrical and optical

measurements, and material parameters. 3) Material synthesis and device fabrication was performed and studied for a low cost all solution process. However, we successfully overcame these hurdles and showed the insights of the novel mechanism of photovoltaics using colloidal quantum dots and ferroelectric nanoparticles hybrid device.

1.3 Research Impact and Summary

In this thesis, inorganic quantum dot (or nanocrystals) based solar cells demonstrate some of the desirable advantages of organic counterparts in terms of lower cost and scalability, combined with ferroelectric PV layers. Although ferroelectric photovoltaics has been known for 50 years, it was not investigated extensively due to the low power conversion efficiency. Thus, we have very limited knowledge of ferroelectric materials and the underlying PV mechanism. Remarkably, recent research on the ferroelectric PV cell shows that engineered domain walls can exhibit a photovoltaic effect with an impressively high voltage output. The internal electric field in the ferroelectric material is one order of magnitude larger than conventional p-n or hetero junction solar cells. We showed a hybrid device using solution based QDs and Ferroelectrics (FE-QDs) and showed the much higher PV efficiency compared to that of each single layered devices. As discussed above, there were critical challenges in both nanocrystals and ferroelectric materials to achieve an efficient PV performance. Therefore, our study dealt with the

major challenges such as 1) Efficient charge transfer and transport in nanocrystals and ferroelectric materials and 2) Expand absorption spectrum and current limitation of ferroelectric materials, resulting in novel hybrid PV devices that can combine the strengths of the two approaches, and minimize their drawbacks, leading to a new PV and solar energy paradigm.

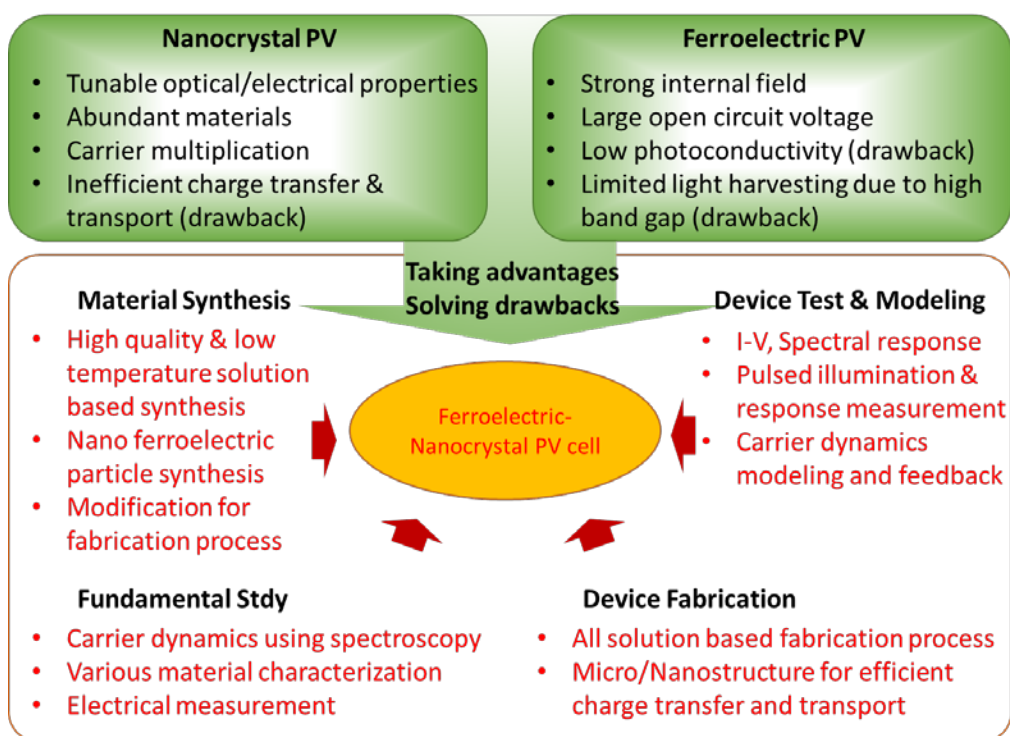


Figure 1.2 Overview of research

Figure 1.2 is the overview of our research motivation. To achieve the novel mechanism and device for the next generation photovoltaics, we used PbS as a QD material and synthesized / fabricated PZT NPs (PZT nanoparticles) as a ferroelectric material. With a successful result of material engineering, we analyzed and studied

physics inside the novel PZT thin film and PZT NP devices. Finally, we fabricated PZT/PbS-QDs thin film hybrid photovoltaic device and achieved high open circuit voltage and high short circuit current device, taking advantages from ferroelectric PZT and PbS QDs, respectively. This shows the great possibility of next generation high efficiency and low cost solar cell. We know of this is also the first demonstration of FE-QDs devices.

1.4 Organization of the Dissertation

In this study, photovoltaic devices made from PZT nanoparticles and thin films have been studied and discussed, which were deposited on TCO (ITO and FTO) substrates. The discussion of structural and electrical properties extends to their corresponding ferroelectric energy band and its future applications. The integration of ferroelectric and CQD materials will be exploited for the potential device applications. The coverage of the topics is interdisciplinary, and the main purpose is to present a sound experimental and theoretical basis for further advances in numerous emerging ferroelectric applications. The intention is that the description of experimental methods, results, and theoretical analysis are included as an integral part. Theoretical analysis and experimental results are presented and combined to build this integral basis.

Chapter 1 is about the motivation in which the idea of this research started, and discuss the state-of-art of ferroelectrics, nanotechnology, and photovoltaics.

Chapter 2 introduces the general ferroelectric properties as well as its history.

Furthermore, we discussed why the PZT material was chosen. We discussed ferroelectric properties, such as remnant polarization, P-E hysteresis, photo responses and bulk photovoltaic effect.

Chapter 3, Colloidal quantum dot also discussed in detail from its synthesis, performance, potential hurdles and future possibilities in details. We also included its history, and discussed QD size effect, quantum confinement, tunable bandgap, MEG and its photovoltaic effect.

Chapter 4 introduces the synthesis methods. The first part is a sol-gel technology with an emphasis on nanoparticle synthesis which is employed for all fabrication of ferroelectric nanoparticle thin films discussed in this thesis. Second is colloidal technology for the CQD synthesis. Aspects applicable to thin film fabrication of nanoparticles and QDs are described with the following of specific discussion of several growth parameters: temperature, chemical solution, Zr/Ti ratio, and thickness of ferroelectric PZT, and temperature and time reaction relations of PbS QD nucleation.

Chapter 5 describes PZT thin film devices fabricated by sol-gel solution on TCO substrates with Al electrode, in order to show that the PZT device is ready for the next step hybrid device. The structural and electrical properties are discussed with a focus on their ferroelectric properties. Also, the photovoltaic properties of PZT thin films of the

photocurrent and J-V curves are studied in this chapter, and the optical properties and energy bandgap are discussed.

Chapter 6 describes high-quality PZT nanoparticle films on ITO substrates with Al electrode. As we know, this structure photovoltaic device is the first trial. Ferroelectric and photovoltaic properties of the PZT nanoparticles were intensively studied. The structural and electrical properties are discussed with a focus on their ferroelectric properties and compared with PZT gel coated thin film device from Chapter 5.

Photovoltaic properties of PZT nanoparticle films of the photocurrent and J-V curves are studied in this chapter. Unique nanoscale properties are also shown in this chapter, and the measurement technique is also discussed in detail.

Chapter 7 describes a novel hybrid device made by ferroelectric PZT thin film and PbS quantum dots. Higher light energy harvesting was observed, and the device was compared with conventional ferroelectric photovoltaic devices. This work is the first trial to make a ferroelectric and quantum dots (FE-QDs) hybrid device and show the great possibility of the new concept of the hybrid device, while the ferroelectric-organic photovoltaic hybrid device is dominant in this research area.

Chapter 8 is for summary and future works. We intend to study the possibility of future photovoltaic or photo sensing applications using the novel material PZT NPs, and novel concept of the device make a fusion with quantum dots and organic materials.

Chapter 2. Ferroelectricity

Overview

In this chapter, we will review the fundamental characteristics and properties of ferroelectric materials, and its applications. We will present the origin of the ferroelectricity, and the details of ABO_3 structure, Curie temperature and its polarization-electric field hysteresis will also be discussed. Then, Ferroelectric material domain and the related photo-response properties will be discussed to explain the new concept of the photovoltaic theories. Finally, the reason why the PZT was chosen will be explained in this thesis, at the state of its morphotropic phase boundary.

Background of the Ferroelectricity

Since the first discovery of ferroelectricity from a Rochelle salt (which has given its name to an entire group of crystals) 1920 by Valasek, [15] various ferroelectrics were introduced. Barium titanate, Rochelle salt, triglycine sulfate, potassium dihydrogen phosphate, lead titanate (PT) and titanate zirconate of lead (PZT) are among the most widely used and thoroughly investigated ferroelectrics. [16] Among them, lead zirconate titanate ($Pb(Zr,Ti)O_3$), commonly called PZT, is considered to be the most potentially important in non-volatile memory and energy harvesting applications. Especially during the last two decades, ferroelectric PZT materials were used for non-volatile memory and random access memory (RAM) applications due to the demand of high dielectric constant and nonvolatile property from the semiconductor industry. After extensive research and development, Samsung developed a PZT based 4 Mbit 1T-1C ferroelectric memory for

commercial use. [17] Another interesting property of the ferroelectric material is the bulk photovoltaic effect (BPVE) [18]. Unlike in the p-n junction solar cell, steady-state photocurrent can exist in a homogeneous medium under uniform illumination. In the past decades, continuous progress has been made in integrating ferroelectric PZT photovoltaic technology to achieve high efficiency and low cost solar cells, because of their internal polarity and photo-sensitive properties. [19-24] PZT photovoltaic devices can be prepared by various growth and synthesis methods such as sol-gel solution process, Molecular Beam Epitaxy (MBE) growth and sputtering methods. BVPE has several unique features such as extremely large photovoltage which is 'above the materials bandgap'. [10] However, studies for a photovoltaic device with PZT showed low photocurrent and poor absorption range from the solar spectrum, which are the drawbacks for the solar cell applications using ferroelectric materials.

In this chapter, the definition and basic properties of ferroelectric materials are presented.

2.1 Ferroelectric Materials

Ferroelectric materials are a group of crystalline dielectrics having spontaneous polarization within a certain temperature range. The orientation of polarization can be reversed by an electric field, which varies significantly under the influence of external factors. In the viewpoint of hierarchy, ferroelectric materials are a subgroup of pyroelectric materials, which will generate electricity from thermal energy from the outside, or vice versa. And pyroelectric materials are a subgroup of piezoelectric materials, which will generate electricity from the mechanical movement outside of the

materials. Pyroelectric materials present piezoelectric properties while ferroelectric materials possess both pyroelectric and piezoelectric properties, in addition to their unique ferroelectric properties.

Decades of studies have been performed in the field of ferroelectricity since the discovery of ferroelectricity in Rochelle salt ($\text{KNaC}_4\text{H}_4\text{O}_6 \cdot 4\text{H}_2\text{O}$; means “rock” in French) in the 1920s. [25] However, early work did not attract longer attention because the composition of Rochelle salt has slightly changed by dehydration in either a vacuum or in dry air. The occurrence of ferroelectricity from potassium dihydrogen phosphate (KDP) and isostructural dihydrogen arsenate was reported by Bushc and Scherrer in 1935 and that was when ferroelectricity started to attract more attention. [16] Further studies were led to the discovery of ferroelectric perovskite oxide barium titanate (BaTiO_3) in 1945 by Ginsberg. Other lead based materials, like PZT (1949), PbTiO_3 (1950), PbZrO_3 (1951) with much simpler crystal structures and more stable ferroelectric properties, were also studied subsequently.

Ferroelectric ‘thin films’ has also been attractive for over decades with a wide range of application from non-volatile memories, piezoelectric devices and pyroelectric sensor to optical devices, according to the development of thin film technology. Some of the ferroelectric materials like PZT ($\text{PbZr}_{1-x}\text{Ti}_x\text{O}_3$), SBT ($\text{SrBi}_2\text{Ta}_2\text{O}_9$), BST (BaSrTiO_3) were popular materials for thin film ferroelectric research. And these materials have overcome many drawbacks, from moisture instability in the early stage of the ferroelectric history to fatigue phenomenon of nonvolatile memory within the past 20 years. Among the ferroelectric materials Pb-based perovskite ferroelectrics including $\text{Pb}(\text{Ti,Zr})\text{O}_3$ (PZT), $(\text{Pb,L a})(\text{Zr,Ti})\text{O}_3$ (PLZT), PbTiO_3 (PTO), have been attracted

researchers because of their high remnant polarizations and comparably low heat treatment temperatures. Pb-based thin film ferroelectrics are simple and stable compared to those earlier ferroelectric materials. [26-28] With these simple and stable characteristics, the Pb based perovskite oxides became more important. Pb based materials also opened the way to the industrial applications using ferroelectric materials.

With the presence of an external electric field, dielectric materials have the property to align internal dipoles, as shown in Figure 2.1. The total charge remains unchanged in the bulk of the material, but at the edges, the aligned dipoles effectively act as surface charges (P). While most dielectrics lose their polarization after the removal of the external field, ferroelectric, which also is one kind of dielectrics, remains its polarized condition.

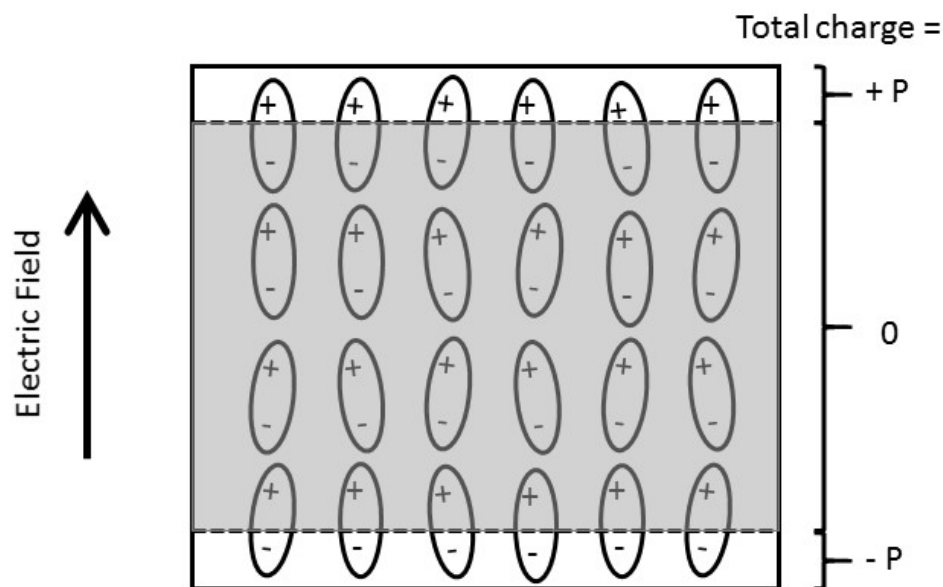


Figure 2.1 Representation of the dipoles in a dielectric material placed in an electric field. [29]

In analogy to magnetism, also referred to as ferromagnetism, the surface charge that remains after the removal of the external field is called remnant polarization (P_r). The direction of this polarization depends on the original external field (original polarization). If a ferroelectric material is polarized, small external electric fields cannot change the orientation of its dipoles. If there is external electric field larger than a certain level, dipoles can start to change their direction. Since 1976, thin film PZT have been studied and developed using both vacuum and chemical solution techniques. The thin films are similar to bulk ceramics, reproducing ferroelectric properties and high permittivity (ϵ_r). They are therefore suitable dielectrics for use in integrated circuits for non-volatile ferroelectric random access memory (FERAM) and dynamic random access memory (DRAM), where high capacity can be obtained using less area, and the high relative permittivity of the PZT allows the fabrication of capacitors up to 100 nF directly onto integrated circuits. Another important application to use PZT is photovoltaic and photo sensing devices because of its photo-response property. Light illumination can initiate electric dipoles and separation of electron hole pairs. The operating principle of the ferroelectric photovoltaic device is different from the p-n junction based PV cells. In the following sections, we will discuss more details to understand PZT based photovoltaic devices.

2.1.1 Perovskite ABO_3 Structure

Most of the ferroelectric materials have an ABO_3 perovskite structure as shown in Figure 2.2. As can be seen in Figure 2.2, the A element (which is Pb in the case of PZT) is a large cation situated at the corners of the unit cell, and the B element (which is Zr or

Ti in PZT) is a smaller cation located at the body center. The oxygen atoms are positioned at the face centers. These materials have a characteristic temperature, namely the Curie temperature (T_c), at which the material makes a structural phase change from a polar phase (ferroelectric phase) to a non-polar phase, typically called the paraelectric phase. Crystals can generate the local electric field by the displacements of cations and anions in the crystals. At high temperatures above the Curie point, the thermal energy of the crystal lattice becomes so high that the lattice vibrations are equally distributed in all directions, which is called cubic structure, so that no dipole moment exists on average and the crystal maintains the paraelectric cubic structure. [30] However, as the temperature cools down below the Curie point, the thermal energy is no longer high enough to vibrate the lattices in x-, y- and z-direction randomly and will not stay in its cubic structure. As shown in Figure 2.2, this deformation depends on the zirconium to titanium ratio in the case of PZT. [31] For lead titanate, the phase below Curie temperature is tetragonal ($a=b \neq c$, $r=90^\circ$). A larger zirconate content exhibits a rhombohedral (or trigonal, $a=b=c$, $r < 120^\circ \neq 90^\circ$) structure after phase transition. In tetragonal structure, the cations, Zr^{4+} or Ti^{4+} and Pb^{2+} ions, are displaced slightly, and this deformation develops a dipole moment, and the PZT remains in the ferroelectric state. Because the phase transition in PZT induces a dipole moment by displacing ions in the crystal, the lattice constant of ABO_3 is known about 4 Å including PZT. [32]

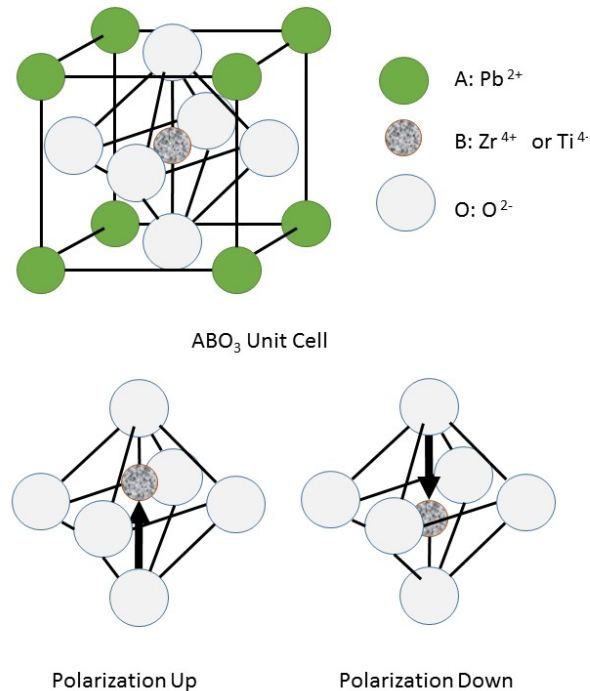


Figure 2.2 Perovskite ABO_3 unit cell for PZT, illustrating 180° polarization reversal for two of the six possible polarization states produced by displacement of the central cation in the tetragonal plane [25]

When we talk about piezoelectric materials including ferroelectrics, piezoelectric materials are “perovskite” crystalline structure. The name, perovskite, is come from the mineral name of calcium titanate ($CaTiO_3$) having a structure of the type ABO_3 . Many piezoelectric (including ferroelectric) ceramics such as $BaTiO_3$, $PbTiO_3$, PZT, PLZT, lead magnesium niobate (PMN), potassium niobate ($KNbO_3$), Potassium Sodium niobate ($K_xNa_{1-x}NbO_3$), and Potassium tantalate niobate ($K(Ta_xNb_{1-x})O_3$) have a perovskite type structure. That is why PZT is called perovskite ferroelectric material, and it has ABO_3 type structure.

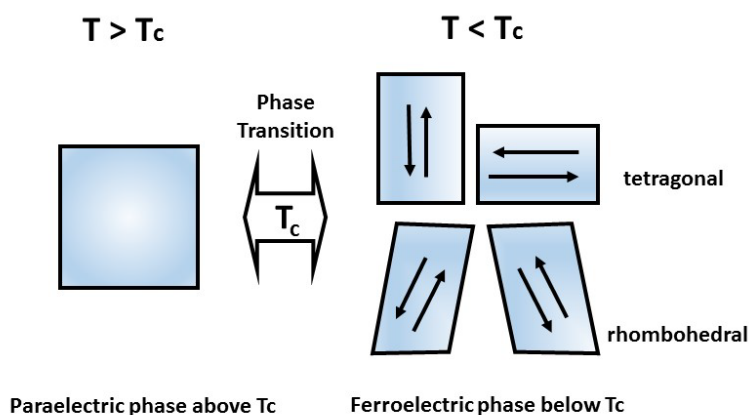


Figure 2.3 Schematic diagram of the phase transition in a ferroelectric material. T_c is the phase transition temperature. The arrow, indicates the direction of spontaneous polarization in the ferroelectric phases.

We have discussed; ferroelectricity is characteristic that will have a spontaneous polarization without any electric field from the outside. The spontaneous polarization can be switched by applying an external electric field which is above the certain range of voltage. All ferroelectric materials have a transition temperature called the Curie point (T_c), and at temperature $T > T_c$, the crystal does not exhibit ferroelectricity. Above T_c , the crystal has a centrosymmetric structure, normally called cubic structure, and has no spontaneous polarization. Meanwhile, for $T < T_c$, it is ferroelectric. Below T_c , the crystal exhibits ferroelectricity and has a structure resulting from a change in the symmetry of the unit cell, normally in the structure of tetragonal or rhombohedra structure. [33] As a perovskite materials are cooled down to below T_c , the central ion in the unit cell

displaces from its equilibrium position to create a spontaneous polarization.

Consequently, a perovskite ferroelectric material transforms from a paraelectric centrosymmetric structure into a ferroelectric noncentrosymmetric structure which is often tetragonal or rhombohedral.

Figure 2.3 depicts the phase transition in a ferroelectric material when the ferroelectric materials are under Curie temperature after phase transition, and a Cubic structure was shown on the left which is paraelectric phase above T_c . Below T_c , the structure was changed to tetragonal or rhombohedral structure, where the arrow indicates the direction of spontaneous polarization in the ferroelectric phases. Tetragonal phase has 6 directions of polarization directions while rhombohedral has 8 polarization directions. In this figure, only 2-dimensional directions are shown.

2.1.2 P-E Hysteresis

As we discussed above, the switching of polarization with an applied electric field is the essential property of ferroelectrics. Thus measuring the change of polarization has been studied and defined as the Polarization-Electric field (P-E) hysteresis loop measurement where the polarization is plotted against the electric field. As illustrated in Figure 2.4, the value of polarization remains nonzero even without the electric field, which is known as remnant polarization, P_r . The direction of polarization is changes when the electric field is applied in the opposite direction with its amount is higher than the coercive electric field E_c . This is analogous to ferromagnetic properties of magnetic

materials. The differences we should think are electric polarization instead of magnetic polarization and external electric field instead of the external magnetic field.

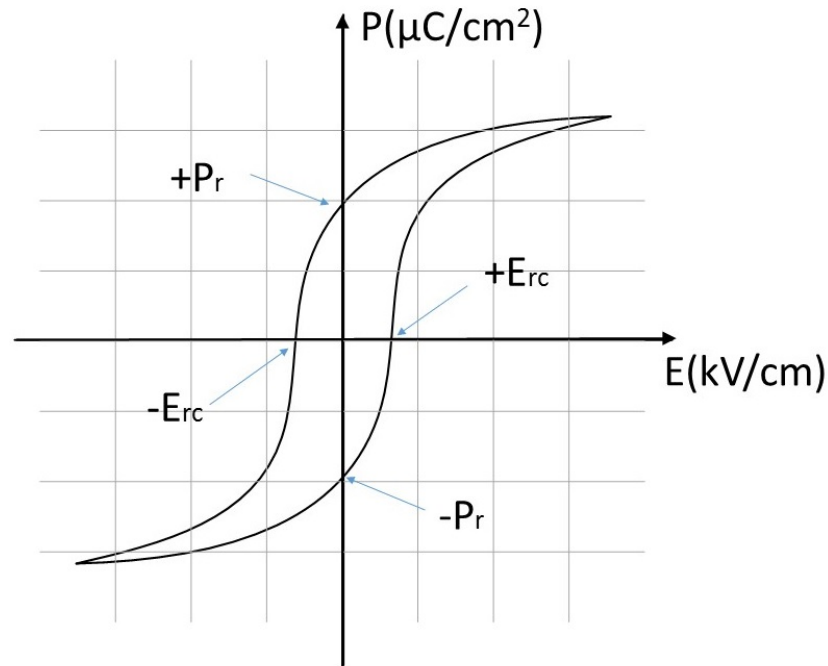


Figure 2.4 Typical hysteresis loop of a ferroelectric material. Remnant polarization is marked as P_r and coercive electric field is marked as E_{rc}

The P-E hysteresis loop (Figure 2.4) is a typical and unique characteristic of ferroelectricity where the materials illustrate this behavior below Curie temperature (T_c). Ferroelectric materials transit its state from ferroelectric to the paraelectric phase when the temperature decreases through the Curie point T_c . In the paraelectric phase under the T_c , there is no hysteresis behavior or remnant polarization in the materials, and the polarization exists only by an applied electric field. When the electric field is removed, the polarization returns to zero as shown in Figure 2. 5.

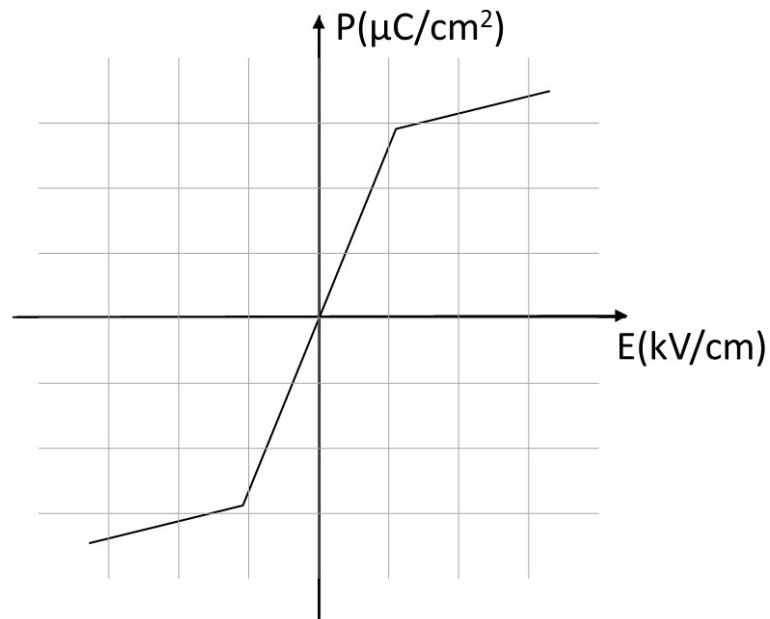


Figure 2. 5 Typical paraelectric polarization versus electric field.

2.1.3 Ferroelectric Domain and Domain Walls

A ferroelectric domain is a space where the spontaneous polarization is uniformly oriented. Figure 2.6 (a) shows the six possible spontaneous polarization direction in tetragonal ferroelectric materials including PZT. The six directions in the cubic cell are equivalent to the high temperature paraelectric phase, but can be distinguished in below T_c temperature ferroelectric phase. During the phase transition from the cubic to the tetragonal phase, the spontaneous polarization can arise along any of six directions.

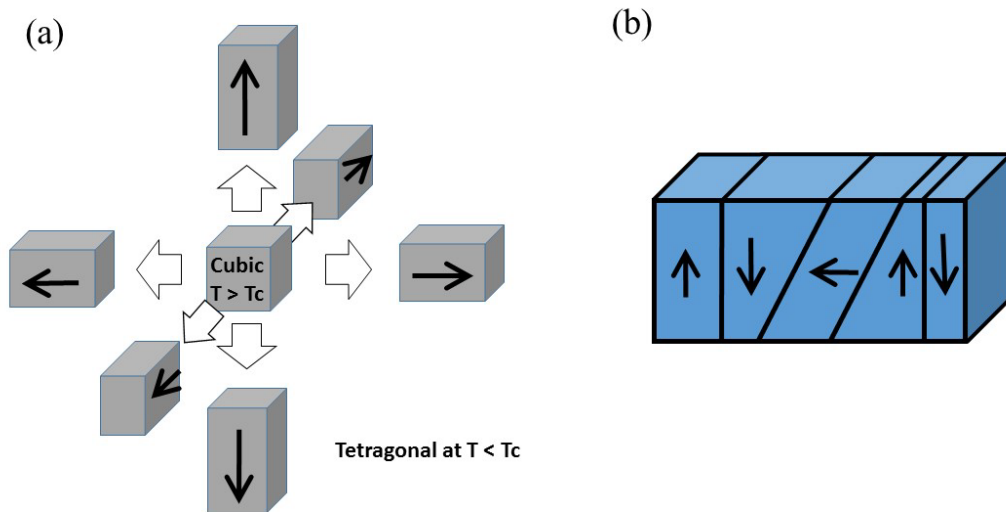


Figure 2. 6 (a) Six possible directions of tetragonal PZT ferroelectric polarization under Curie temperature. (b) Schematic diagram of 90 ° and 180 ° domain walls. The arrows indicate the polarization directions.

The interface between neighboring two domains is called a domain wall. In a ferroelectric material, the width of domain walls is very small around 1-2 nm. [10] In a tetragonal ferroelectric phase, the angles between two domains are either 90° or 180°, whereas they are 71°, 109°, or 180° in a rhombohedral phase. The walls separated by perpendicularly oriented polarization are called 90° domain walls while 180° domain walls are separated in the opposite direction. The 90° and 180° domain walls are schematically shown in Figure 2.6 (b). 180° domains can be reversed with minimal structural strains. However, switching of 71°, 90°, 109° domains require a significant structural deformation, due to the fixture of the lattice in x-, y- or z-direction while cooling down crystallization time under the temperature of T_c.

2.1.4 Polarization Switching and P-E Hysteresis Loops

The polarization can be reoriented in the opposite direction of the electric field when an external field is applied in a direction opposite to the polarization. This process is reversible and is called polarization switching. Using polarization switching, we can reorganize ferroelectric internal electric fields. When the polarization is parallel to an applied electric field, the switching is done. However, not all polarization is exactly reoriented along the electric field direction.

The polarization switching can be measured by the displacement current that flows while the applied electric field is sweeping from minus to plus and vice versa. The charge in the polarization of the ferroelectric measured by the applied electric field can be calculated by integrating the displacement current. This important characteristic of a ferroelectric is called a polarization and electric field hysteresis. A hysteresis loop shows the polarization switching behavior with the value of P_r and E_c , where P_r is remnant polarization and E_c is a coercive electric field. The net polarization of an initially not polarized ferroelectric material is small. When an electric field is applied below E_c , there is a linear relationship between switchable polarization and the applied electric field. In this case, there is no polarization switching. As the electric field increases higher than E_c , domains in which the direction of spontaneous polarization is opposite to electric field, and begins to switch to a more energetically favorable direction. The switching process continues until all of the domains are aligned in the electric field direction under the electric field above E_c . When the field returns to zero, the polarization still does not return to the initial value. The amount of switchable polarization after the removal of an electric field is the remnant polarization, P_r and the strength of the electric field to switch

the opposite polarization domain is a coercive electric field, E_c as we discussed above, and this process can be repeated multiple times because of its reciprocal property. One of the applications of this hysteresis phenomenon is the ferroelectric non-volatile memory. For example, when the polarization is up, it contains the data “1”, and when the polarization is down, the data means “0”. Because this process can be repeated, ferroelectrics can be used as a RAM, even non-volatile when there is no power from outside. However, typical ferroelectric materials show fatigue property, which means polarization will decrease while it reads and writes many times. Many efforts were exerted on improving fatigue of ferroelectrics though we will not discuss further this. [34]

Another aspect of important polarization switching is effect to the carrier transportation. By changing polarization direction, we can change carrier density. [35] This means that we can control current by changing polarization or with pre-poling of the device. This polarization and its carrier transportation have not been studied fully but has been gaining more interests recently.

2.2 Ferroelectric Photo Response

The Photodiode is well-understood device and used in many areas in modern times. Photodiode uses asymmetric interfaces such as p-n junctions or metal/semiconductor Schottky junction interfaces. However, photo-induced currents in ferroelectric materials were not summarized well. Also, the relationship between electronic transport characteristics and ferroelectric polarization had been studied only a little. This was

partially due to the complexity of ferroelectric domains. However, it is well known that bulk photocurrent can be induced by high-energy light illumination even in good insulators. And photocurrents without external bias has been studied in ferroelectrics by some research groups. [36-41]

When a ferroelectric thin film in an open circuit is illuminated by light, a higher photovoltage, than the energy bandgap, has been observed in the direction of the electric polarization. [36, 38] The magnitude of this photovoltage is directly proportional to the crystal length in the polarization direction. In addition, a steady-state photocurrent can be generated in the direction of the electric polarization when a ferroelectric thin film under continuous light illumination forms a closed circuit. [42] This photovoltaic effect in ferroelectrics is distinctly different from the typical photovoltaic effect in p-n junctions, and it was also observed in Pb-based ferroelectric oxides [40, 41, 43] and LiNbO_3 [36, 38]. However, the observed photocurrent density turns out to be very small, on the order of a few nA/cm^2 . This is mainly due to poor bulk dc conduction of the ferroelectrics and poor absorption of the solar spectrum. [38, 39]

Recently, T. Choi et al. discovered that unidirectional electric current flows from ferroelectric materials which are normally seen from p-n junction type diode. [42] They found bulk electric conduction in ferroelectric monodomain BiFeO_3 crystals and is highly nonlinear and unidirectional. This pseudo-diode current effect can be switched its direction when the electric polarization is flipped by an external voltage. This is a brilliant discovery that we can contribute to the carrier transportation by polarization, and by implicating this, we can change the current direction with the ferroelectric device while changing polarization direction under illumination conditions.

Few years ago, the research interest in ferroelectric devices was generated again by the discovery of above-bandgap photovoltaics caused by the ferroelectric domain wall effect. Photo-voltage has been known that it is related with many factors, such as the thickness of photo response material, conductivity and remnant polarization of the ferroelectric crystals, crystal orientation, domain size and domain wall, and the surface interface between ferroelectric and metals. A few models were suggested to explain the relationship of these factors. A popular model to explain the photovoltaic effect from the ferroelectric materials until now is bulk photovoltaic effect and Schottky junction effect. However, a sophisticated explanation was revealed recently, which is domain wall effect and depolarization effect. In this section, we will review the conventional bulk photovoltaic and Schottky effect models and new models of depolarization field and domain wall theory.

A. Bulk Photovoltaic and Schottky effect

Ferroelectric material has noncentrosymmetric as reviewed in the previous section. In the noncentrosymmetric material, the probability of the electron transition with a momentum k is different from the probability of the transition to opposite direction with a momentum k' . Therefore generated electrons under illumination condition make a steady current in one direction. This is a different model from the p-n junction photovoltaic shown in Figure 2.7.

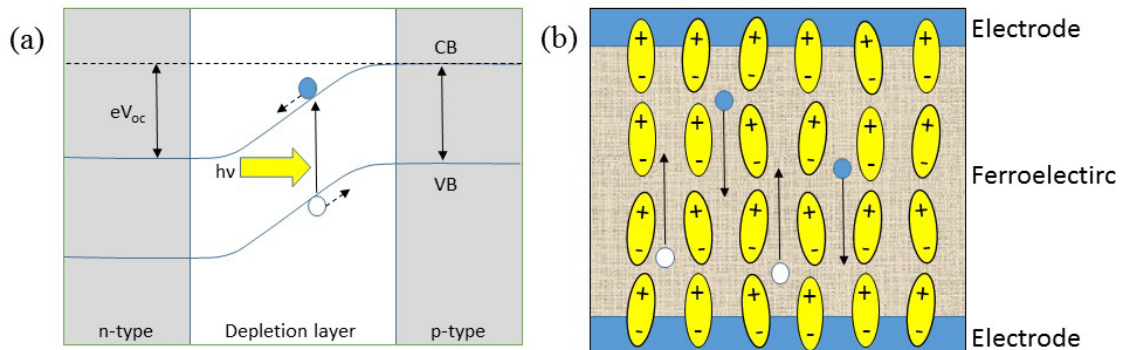


Figure 2.7 Schematic diagram of the working principle of (a) p-n junction photovoltaics, and (b) ferroelectric photovoltaics. Reproduced with permission from ref [10]. Copyright © 2010 Nature Publishing Group

Schottky junction has been observed and studied in many semiconductors to metal interfaces. When the ferroelectric materials contact with a metal interface, there is photocurrent under illumination, same as that of semiconductor and metal interface. Schottky effect is caused by the band bending, which is due to the energy bandgap mismatch between ferroelectric materials and metals. The value of photocurrent is determined by the Schottky barrier height and depth of the depletion layer. Photo-voltage is more related with ferroelectric crystallization rather than the Schottky bandgap differences since the Schottky derived photo-voltage is smaller than ferroelectric deduced photo-voltage. Noble metals were widely used, such as Pt or Au, to use its rectifying characteristics for photovoltaic applications.

B. Depolarization Effect

As shown in Figure 2.1., there are high densities of polarization charges on the surface of the ferroelectric bulk system. These surface polarization can make a huge electric field across the ferroelectric bulk or ferroelectric thickness. The surface charge due to the ferroelectric polarization is called depolarization field. Depolarization field effect is more obvious when a bulk or film thickness is small since the electric field is inversely proportional to the thickness. Or it is obvious when the contact material is a semiconductor rather than a metal, because metals tend to screen the depolarization effect with its free electrons. However, the relationship of the depolarization field and the photovoltage is still not clear, due to the presence of bulk photovoltaic or Schottky effect and its interference result from photovoltaic data.

C. Domain Wall Effect

Recently, domain wall effect was highly interested, which was evoked by S.Y. Yang et al., with their milestone report. [10] They reported that the photo-induced carrier can be separated more easily at the ferroelectric domain wall using the BiFeO_3 (BFO) film. They observed that the photo-voltage in the BFO film increased linearly with the total number of domain walls along the net polarization direction. The intrinsic potential drop at the domain walls is from the narrow domain wall. This steep energy bandgap induced dissociation of the photon-generated excitons. Dissociated carriers from the steep energy band gap are diffused in the bulk area as minority carriers. Electric field induced by the penetrated minority carriers in nanocrystals sum up and make a high voltage across the

electrode. This phenomenon was named “above bandgap photovoltage” and is schematically explained in Figure 2.8

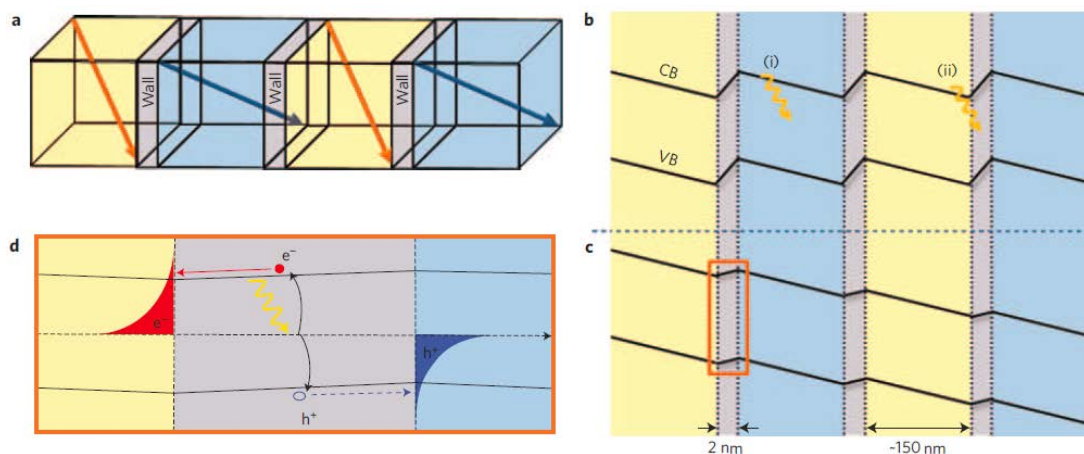


Figure 2. 8 Band structure in dark conditions and under illumination of BFO film. [10] (a), Schematic of four domains (three domain walls) in an ordered array of 71° domain walls. (b), Corresponding band diagram showing the valence band (VB) and conduction band (CB) across these domains and domain walls in the dark. Note that there is no net voltage across the sample in the dark. Section (i) illustrates a photon hitting in the bulk of a domain and section (ii) a photon hitting at a domain wall. (c), Evolution of band structure upon illumination of the domain wall array. (d) A detailed picture of the build-up of photo excited charges at a domain wall. Reproduced with permission from ref [10]. Copyright © 2010 Nature Publishing Group

2.3 Perovskite PZT

Triglycine sulphate (TGS) and KNO_3 are some of earlier ferroelectric materials studied, but they are very unstable in the presence of moisture. The perovskite titanate and niobate families have been studied since the 1950s. Among these ferroelectric materials, BaTiO_3 and PZT have been intensively investigated because of their excellent ferroelectric, piezoelectric properties and moisture stability.

Lead zirconate titanate (PZT) has long been the leading material considered for ferroelectric memories, optical sensors and other application like piezoelectric actuators, [44] though strontium bismuth tantalate (SBT) and BST, a layered perovskite, is also a popular choice due to its superior fatigue resistance for memory applications. These are also popular because it is lead-free, which is required specification from IT industry these days. However, it requires a higher processing temperature, which creates high cost and difficulties of fabrication, even though progress has been made in optimizing precursors recently with SBT and BST.

Generally, perovskite oxides have attractive light absorption and comparably easy to change A and B materials forms ABO_3 structure. Especially, perovskite PZT is one of the most popular materials due to its various fabrication method and low-temperature processing.

2.3.1 Morphotropic Phase Boundary of PZT

Perovskite structure lead zirconate titanate, $\text{Pb}(\text{Zr}_x\text{Ti}_{1-x})\text{O}_3$ ($0 < x < 1$) is a well-known ferroelectric material. PZT is a combination of two perovskite materials: lead zirconate

(PbZrO_3) and lead titanate (PbTiO_3). Both of these materials are also perovskite ferroelectric materials.

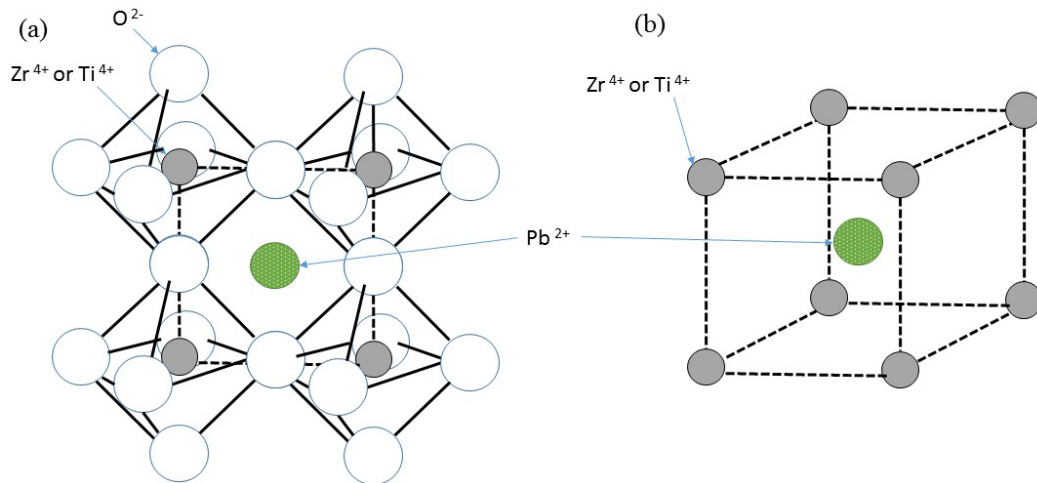


Figure 2.9 Perovskite structure from PZT atomic cells

Figure 2.9 shows unit cell structure of PZT's ABO-type structure. Eight divalent Pb^{2+} ions locate at the A sites and one tetravalent Zr^{+4} or Ti^{+4} ion does at the B site, and the oxygen ions sit at the face-center of the unit cell. In the unit cell structure shown in Figure 2.9, solid circle position can be filled with Ti or Zr. This Ti/Zr position is known as being able to move up or down, not in the center, and make ferroelectric polarization. [45]

PZT is a complicated material which has different characteristics by not only Ti/Zr ratio but also its annealing temperature. Figure 2.10 shows the phase diagram of PZT according to the temperature and the ratio of PbZrO_3 and PbTiO_3 .

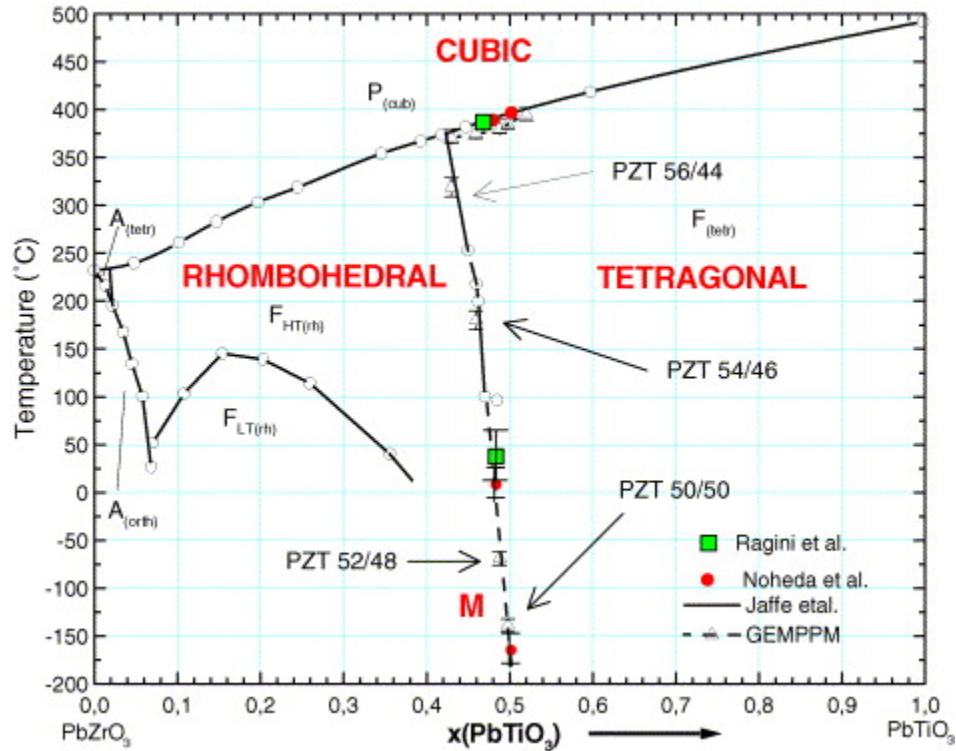


Figure 2. 10 PbZrO_3 - PbTiO_3 phase diagram. F, P, and A stand for ferroelectric, paraelectric and antiferroelectric phases respectively. The subscript T denotes a tetragonal phase; C a cubic phase; R a rhombohedral phase, of which there are high temperature (HT) and low-temperature (LT) forms. Reproduced with permission from ref [29]. Copyright © 2005 by Journal of European Ceramic Society.

PbTiO_3 is a ferroelectric material with a Curie temperature of 490 °C, whereas PbZrO_3 is antiferroelectric with a low Curie temperature of 230 °C. Above the Curie temperature, PZT has a paraelectric cubic perovskite phase over the whole range of composition. The phase diagram at the Zr rich region is considerably complex below the Curie temperature, where even small amounts of Ti can turn the antiferroelectric structure

of PbZrO_3 to a rhombohedral ferroelectric phase, but is also reversible to antiferroelectric orthorhombic phase at the low-temperature. With increasing the Ti concentration (7%), this transformation between antiferroelectric and ferroelectric can be significantly depressed and eventually disappears. The vertical phase boundary, well-known as morphotropic phase boundary (MPB) occurs at about $x = 0.53$, associated with favorable piezoelectric and ferroelectric properties due to the coexistence of tetragonal and rhombohedral phases. At the MPB, the dielectric constant also passes through a maximum, whereas the coercive field passes through a minimum. [46] The phase diagram is first reported by Jaffe et al. [47] and the best performance shown morphotropic phase boundary (MPB) is around $\text{Zr}:\text{Ti} = 53:47$. Later, Noheda et al. also confirmed that the MPB is around that point by XRD study. [32] Therefore, most experiments here focus on the characteristics of a PZT thin film and PZT NP with an MPB composition, which has the ratio of $\text{Zr}:\text{Ti} = 53:47$, $(\text{Pb}(\text{Zr}_{0.53}\text{Ti}_{0.47})\text{O}_3)$.

Chapter 3. Quantum Dots

Overview

In this chapter, we will discuss the details of colloidal quantum dots. One of the fascinating properties of quantum dots are its energy bandgap tunability by the quantum confinement effect. We will explain the related exotic properties such as tunable energy bandgap, narrow emission, multiple emission generations (MEG) and the QD photovoltaic effect. We will also discuss the synthesis method of the colloidal quantum dots. Finally, we will summarize the advantages and applications from PbS QDs, which is the material used in this thesis.

3. 1 Quantum Dot Size Effect

Materials show different physical, electronic and optical properties when its size is very small, where the size effect cannot be ignored. Quantum dots (QDs) are nanometer-sized semiconductor particles. When the QD size shrinks to the Bohr exciton radius of the corresponding bulk semiconductor, the exciton is confined by its finite-size. The electron-hole pair can no longer exist as the same in the bulk semiconductor materials, which will be discussed later in this section. The energy state, the exciton can exist in bulk, will be changed by the limitation of the nanoscale semiconductor size. From the quantum mechanics and the Schrödinger equation, we see that exciton energy state will

be higher when the particle size is reduced. According to this, the optical and electrical properties of the QDs can be tuned through a particle size. From the size effect, many unique optical and electrical phenomenon were discovered up to today, including photovoltaic effect, photoluminescence, multiple exciton generation (MEG), blinking and more phenomenon which cannot be seen from the bulk semiconductor materials. [48-50]

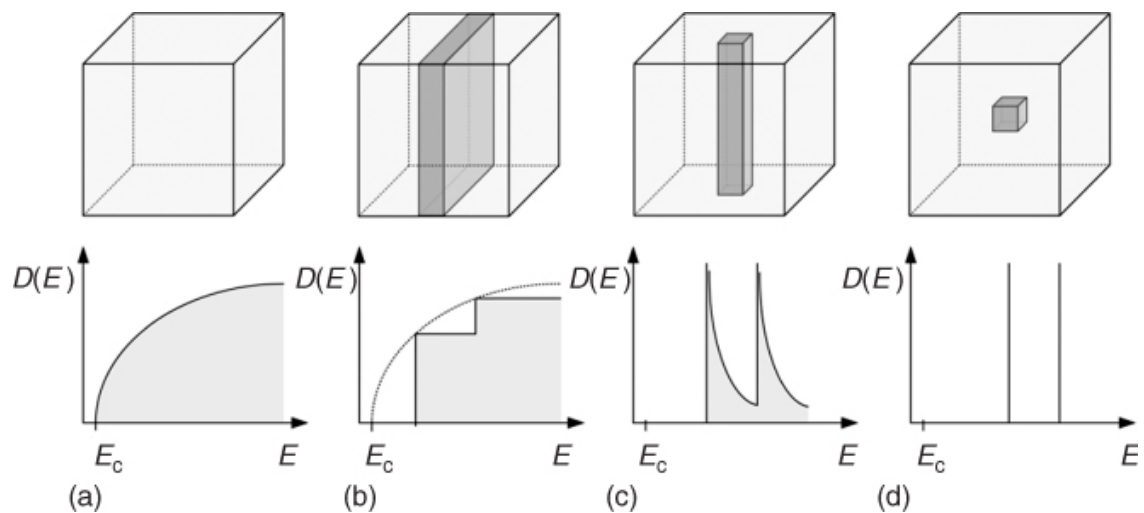


Figure 3.1 Density of states for electrons in bulk conduction band together with those in various confined geometries. (a) bulk, (b) quantum well, (c) quantum wire, (d) quantum dots. Reproduced with permission from ref [51] Copyright © 2014 John Wiley and Sons.

Spatial confinement in semiconductor materials is known as quantum confinement. Quantum confined materials are more attracted, due to the advanced material engineering. When the material is confined in the 3-dimensional (3-D) space, a lot of material properties are changed, such as the optical, electrical, physical and even

chemical ones. This property change is related to the shape, structure and the size of the materials. The quantum confined semiconductor materials are classified as being a quantum well (2-D), quantum wire (1-D) or quantum dots (0-D), where all of them have a structure and/or a space dimensional change from the bulk material. Among them, quantum dots are very interesting due to its free motion, zero-dimensional, maximum surface to volume aspects, which will reveal a variety of unique properties as explained later.

Zero-dimensional QDs consist of tens to hundreds of semiconductor atoms in the shape of dot crystal. There are a few shapes of QDs, such as a cubic or hexagonal in an atomic scale, but in many cases QD is considered as a sphere or a dot.

Energy bandgap in zero-dimensional QD has two unique properties-discrete (quantized) and a higher value of energy bandgap. In a bulk semiconductor, the exciton Bohr radius gives an estimation of the spatial dimension of the exciton. If the semiconductor size is smaller than the Bohr radius, due to the small size of nanocrystals, the strong quantum confinement should be considered as being in discrete energy levels and bigger energy bandgap comparing with the bulk semiconductor. The reason for the discrete energy bandgap can be explained with the density of states and quantum mechanics as explained in the next section. Since the density of states is discrete in QDs, the energy bandgap will be discrete as well (Figure.3.1 (d)). The higher energy bandgap of quantum dots is derived from the one-dimensional box theory from quantum mechanics. [52] The small size of quantum dots provide small semiconductor crystal space, which is the width at the quantum box theory, and the only energy states that can exist in the higher level compare to that of bulk semiconductor crystals. Such bandgap is extremely sensitive to the volume

change of the QDs and can be tuned over a large energy range simply by the size control over the QD. [51]

3.1.1 QD Confinement

Electrons in quantum dots confined in a 3-dimensional quantum box, of which the size ranges from a few nanometers to tens of nanometers. In this scale, thermal electron de Broglie wavelength ($\lambda_{DB} = h / (2m^*k_B T)^{1/2}$, where h and k_B are from the Planck's and Boltzmann's constant, T is temperature) is longer than the QD box size. According to the quantum mechanics, only the standing wave of the electron wave function can exist in the quantum box. Therefore, the energy state should be enlarged.

Free electrons in a quantum dots is a box dimension of k_x , k_y , and k_z given by

$$E = \frac{h^2}{2m_2} (k_x^2 + k_y^2 + k_z^2) \quad (2.1)$$

Where, k_x is n/L_x , where n is the quantum number and L is the width of the quantum well model.

Instead of considering λ_{DB} for electrons and holes separately, it is usually more convenient to describe a QD as a region of space using a concept of the exciton Bohr radius A , where $A = (4\pi\epsilon_0\epsilon_r\hbar^2) / (\mu^*e^2)$. While the exciton can exist using full space of the Bohr radius in the bulk materials, there is a limitation of the Bohr radius in the QDs because of the limited nanocrystal size. It is called quantum confinement. When we select an actual material for the semiconductor quantum dots, we should consider the three confinement regimes. First, in a weak confinement regime, the size of the quantum dot is

larger than both the Bohr radius of the electron and the hole. The created exciton acts much like an exciton in the bulk and follows the rules of a bulk energy bandgap. Second, in the intermediate confinement regime, only the electron is confined (consider the general effective mass of an electron is lighter). Third, in strong confinement regime, both the electron and hole have their energy levels increased and quantized because both the electron and hole are confined. Semiconductor quantum dots with strong confinement exhibit the greatest enhancement in optical properties (consider the optical properties as mainly being related to the photonic generation of a pair of the electron and hole, or related with the recombination of a pair of them).

In some semiconductors, the Bohr radius for the electron or hole is too small to be confined in a quantum dot so that they cannot have the quantum confinement property. So, we should select the right molecular structure for the quantum dots. Many of the quantum dots developed today are strong confinement semiconductor materials.

3.1.2. E_g Tunability of QD

We discussed that the energy bandgap of the quantum dots can be tuned by its size. The physical size of the QD is from the semiconductor's exciton Bohr radius, which is the average distance separating the electron and hole as they are bound in orbit with one another via the Coulomb interaction. Exciton Bohr radii range widely, from 1 to 50 nm, depending on the dielectric constant of the semiconductor material and the charge carriers' effective masses, as shown above. As the QD sizes become smaller, a bandgap between conduction and valence band will become wider. This means that the band edges will be shifted, which can be reached several hundreds of meV and tuned QD's bandgap

over a wide spectral range. The popularity of cadmium chalcogenides (CdS, CdSe) is partially due to its ability to cover the visible spectral range, using this property. The reputation of InAs and lead chalcogenides (PbS, PbSe and PbTe) QDs also are from the ability to cover from the infrared spectrum, due to QD bandgap tunability from its smaller initial bulk bandgap.

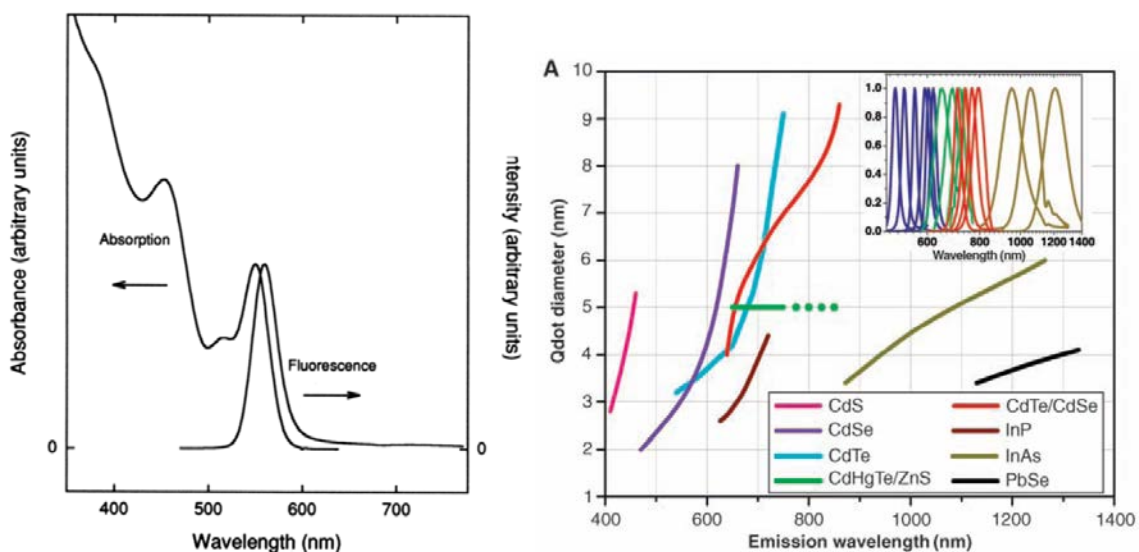


Figure 3. 2 (a) Typical room temperature band edge luminescence and absorption spectra for 3.5 nm CdSe crystallites. Reproduced with permission from ref [53]. Copyright © 1993 American Chemical Society. (b) Emission maxima and sizes of quantum dots of different composition. Quantum dots can be synthesized from various types of semiconductor materials (II-VI: CdS, CdSe, CdTe; III-V: InP, InAs; IV-VI: PbSe) characterized by different bulk band gap energies. Copyrights © 2015 American Association for the Advancement of Science [7]

QDs bandgap tunability has attracted mainly due to its tunable photoemission properties in its early stages of the application. In many cases, QD is considered as a single semiconductor for bandgap engineering. Some of the application examples are as follows. It is referred as a single molecule for biomedical applications, a single spin source like an atom or a single photon source for the lightning applications. [51] Single QDs were viewed as a convenient alternative to organic dyes as markers in biological imaging [54] since they offered a variety of colors by its sizes. Other envisioned applications based on QDs included solution processed light-emitting thin films [55] and optical gain media for lasing applications. [56]

3.1.3 Narrow Emission of QD

Another benefit from the QD bandgap is its quantization. We explained above that QD shows the quantized energy bandgap due to its density of states. Using quantized energy state, it is possible to make a narrow emission linewidth, which is a great benefit for lasers application. [56] It also can be applied to various color-engineering including displays and lighting. [55] In lighting applications, narrow spatial accumulation of holes and electrons within the same semiconductor volume has a great benefit. Examples are QD diodes, radiative recombination of carriers for LEDs, QD films resulting in bright and narrow photon emission which is required from display industry for a high color gamut products. Similarly, laser application using QDs is possible but requires optical gain through stimulated emission. [57]

3.1.4 Photovoltaic Effect

Among QDs' many useful optical qualities, one of the most favorite characteristic is its photovoltaic (PV) effect. PV mechanism can be divided into a few steps. QDs absorb the light above the bandgap and generate free charge carriers, which are electron and hole pairs, with excess energy above the lowest exciton energy; these energetic electron-hole pairs are termed hot carriers. Then the carriers transport to the electrode and contribute to the photovoltaic energy harvesting, and the rest will be recombined, with a phonon or a thermal dissipation, in the semiconductor QDs.

PV effect of QD can be improved by the exciton mechanism, device structure engineering and surface treatment for reducing trap status from QD surface. There is one thing we should point out before discussing the three factors above, which is the Auger recombination. Except radiative recombination, which emits the photon when electron and hole recombine across the energy band gap, there is an Auger recombination. In the Auger effect, one electron gives up its extra energy to a second electron in the conduction or valence band during recombination. In other words, this excited electron then gives up this additional energy in a series of collision with the lattice and eventually returns to its original energy edge state. It is known that the Auger recombination dominates at very high doping level. [58]

Exciton mechanism in the QD is very interesting. In the generation of excitons with excess energy can follow several paths: (1) it can be dissipated as a heat or Auger processes when the carriers relax to their edge-energy state, (2) electron-hole pair can be created if the excess energy is, at least, equivalent to or higher than the QD bandgap, and (3) the electrons and holes can separate and the excess energy can be contributed to

increased electrical free energy. [59] Case (2) is an exotic phenomenon from QDs, and called multiple exciton generations (MEG), which will be discussed in the next section.

In addition to the exciton mechanism, device engineering also contributed to PV development. QD shows the marvelous progress recently as a photovoltaic device with various techniques, such as wide bandgap bulk heterojunction (BHJ), quantum dot sensitized solar cells (QDSSC), and organic-inorganic hybrid structures. [11] One of the main target of the photovoltaic application is to improve the power conversion efficiency. The power conversion efficiency, η , is consist of three multiplicative components: short-circuit current density (J_{sc}), open-circuit voltage (V_{oc}) and fill factor (FF) as shown in equation (3. 2), where P_T is the incident optical power.

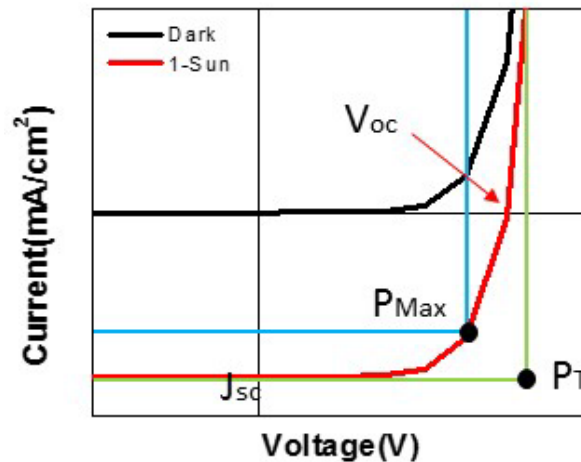


Figure 3. 3 Typical measurements open-circuit voltage (V_{oc}), short-circuit current (J_{sc}), fill factor (FF), maximum power output of the device (P_{max}). The graph is measured by Si photodetector.

$$\eta = \frac{J_{sc} \times V_{oc} \times FF}{P_{in}} \quad (3.2)$$

(where, $FF = P_{Max}/P_T$)

Normally, the progress in QD PV device performance has been achieved through a Schottky QD solar cell. [60] A QD thin film with a transparent conductive oxide (TCO) creates a Ohmic junction. On the other side, a shallow work function metal creates a Schottky junction and a significant built-in potential is established relative to the (natively p-type) QD film. Indium tin oxide (ITO) is typically used as the Ohmic TCO while aluminum and magnesium have been widely used as the shallow work function metal.

3.1.5 Multiple Electron Generations (MEG)

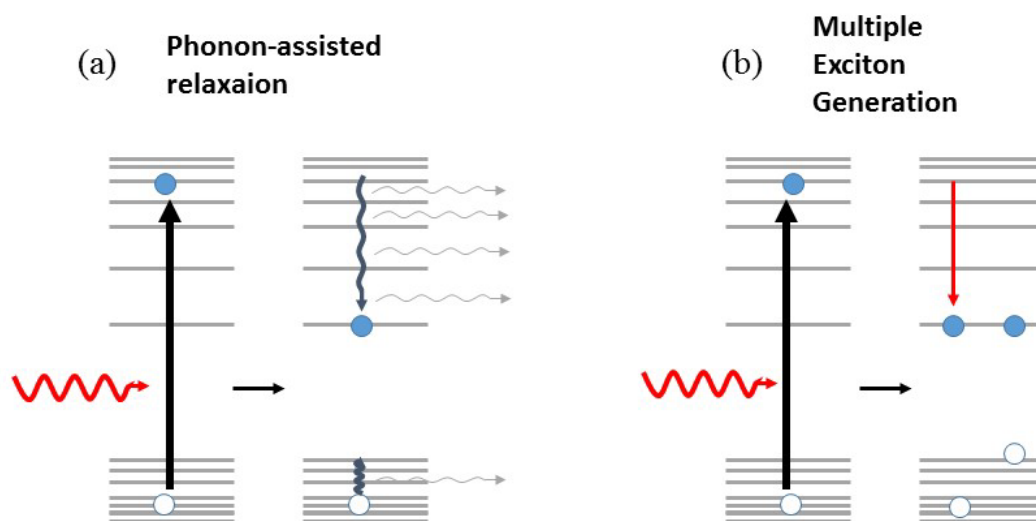


Figure 3. 4 Multiple exciton generation in CQDs. (a) Conventional relaxation of an excited carrier to the band-edge through release of phonons (Auger recombination). (b) Alternatively, the excess carrier energy can be transferred to another exciton. Reproduced with permission from ref [61]. Copyright © 2013 WILEY-VCH Verlag GmbH & Co. KGaA, Weinheim.

There had also been breakthroughs with the surface treatment of the QDs. [62] Also, as long as the surface of the quantum dot is well passivated such that there are no traps for either electrons or holes, the efficiency should be higher than in the bulk because the energy bandgap is higher than that in bulk. However, due to the tiny size to volume ratio of the QDs, it is extremely sensitive to oxidation when exposed to the air. Therefore, the surface treatment of the QDs has been intensely studied and improved recently.

There are two major ways to improve the photovoltaic effect. One is to produce an enhanced photovoltage, and the other is to produce an enhanced photocurrent. For the higher photocurrent, multiple exciton generation (MEG), has attracted much attention in QDs. MEG is the process that the energetic hot carriers produce a second electron-hole pair through impact ionization. [59] MEG, known as a process inverse to Auger recombination, is the process that two electron-hole pairs recombine to produce a single highly-energetic electron-hole pair, instead of a conventional energy dissipation in the form of heat (Figure 3. 4 a). With a sophisticated approach to the bandgap engineering, the process can achieve external quantum efficiency (EQE) of solar cells built from CQD films by 55 - 65% by generating more than one charge carrier for each high energy photon that is absorbed, thus increasing its contribution to the photocurrent. [59]

Nozik reported that MEG is favored in quantum confined systems due to the nanoscale QD is expected to produce slower phonon-mediated relaxation, compared to a bulk semiconductor. [3] Since slowing in the relaxation from the high-level electron in the conduction band down to the band edge was expected to favor high MEG yields. This can be achieved by removing the holes from the QD core by a fast hole trap at the surface. This is because the hole effective mass is much heavier than the electron, hole exciton

will cool down much faster. Therefore hot exciton can contribute to the photocurrent. This process is called a phonon bottleneck in QDs and has been investigated extensively. In contrast to what was predicted, smaller QDs with larger intra-band energy level spacing were in fact found to exhibit faster relaxation to the ground state than what was observed in larger dots, [63] suggesting that surface states and ligand vibrations were dominating the intra-band relaxation. [64]

In order to improve QD device performance, extra charge carriers should be not only created by MEG but be separated and collected at the electrodes. The first example of successful MEG phenomenon in an optoelectronic device was shown in 2009 through the demonstration of MEG-enhanced photoconductive gain in CQD photodetectors. [65] In 2011 MEG was shown to improve the photovoltaic response of CQD solar cells. [66] Device modelling and comparison to experimental data suggested that more than one carrier per photon was generated for photon energies beyond $3E_g$, but to confirm the MEG effect, smaller-bandgap CQD films were used to shift the $3E_g$ value closer to the energies of the solar radiation spectrum and achieve quantum efficiency above 100% for high-energy photons. Lead chalcogenide nanorods were shown to exhibit lower MEG threshold and higher efficiency [67] due to reduced dielectric screening and thus increased Coulomb coupling. [68] Still, extensive experimental and theoretical efforts exerted for understanding the processes, reducing Auger recombination, [69] and enhancing multiexciton generation. [67]

However, QDs have comparably lower photovoltage. Lower photovoltage is a disadvantage, so we need other engineering approach to improve this hurdle. We will

show how we overcome this low photovoltage, using a hybrid structure with ferroelectric thin films.

In summary, we have reviewed the quantum confinement, tunable E_g and MEG in the viewpoint of photovoltaic and optical performance of QDs.

3.2 Colloidal Quantum Dots

3.2.1 Advantages of CQD

There are numerous approaches in fabricating QDs and chemical synthesis is one of popular methods due to its easiness and cost effectiveness [70, 71]. From the point of view of nano manufacturing, this colloidal approach has been studied in order to achieve the scalability, low-cost, and fabrication reliability. In the following sections, we will discuss chemically synthesized nanocrystal QDs that are known as colloidal quantum dots (CQDs).

3.2.2 PbS CQD

Colloidal QDs are usually synthesized according to the procedure initially reported by Murray et al. [72], of which the apparatus shown in Figure 3. 5. This procedure involves heating a coordinating solvent and organic ligands to a temperature of 300 °C.

Organometallic precursors for the desired semiconductor (such as dimethyl cadmium and

trioctylphosphine selenium for CdSe) are then rapidly injected into the reaction vessel, initiating the homogenous nucleation of nanocrystals.



Figure 3. 5 QD synthetic apparatus employed in the preparation of CQDs by the hot-injection method.

Colloidal quantum dots (CQD) are grown in two steps, which is nucleation and epitaxial quantum dot growing on a QD surface. With an organometallic and hot injection method, immediate nucleation can be made. The quantum dots continue to increase in size under the reaction temperature. The size is determined by when the growth is stopped. In this process, quantum dots produce size distribution.

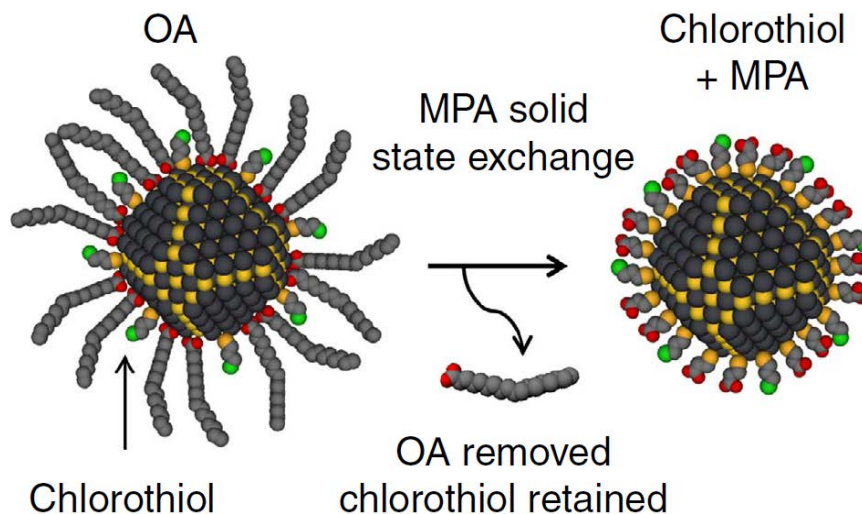


Figure 3. 6 Schematics of the diagram of a general colloidal semiconductor quantum dot. Schematics show the oleic acid (OA) based ligand exchange by 3-Mercaptopropionic acid (MPA). Reproduced with permission from ref [73]. Copyright © 2014 Nature Publishing Group

Figure 3. 6 is a diagram of a general colloidal semiconductor quantum dots. The nanocrystal has a crystal lattice and is often surrounded by organic ligands, which is formed when it is synthesized by a solution method. These ligands surround the dots and make it soluble. The ligands are also involved in the growth process, but after the growth they can be exchanged. The usual ligand for the dots in this thesis is oleic acid (OA), which is highly soluble in nonpolar organic solvents. There are many different semiconductors which can be made by the colloidal method. Typical QDs are made of binary alloys such as cadmium selenide (CdSe), cadmium sulfide (CdS), indium arsenide (InAs), lead sulfide (PbS) and lead selenide (PbSe). QDs may also be made from ternary alloys such as cadmium selenide sulfide ($\text{CdSe}_x\text{S}_{1-x}$). These quantum dots can contain as

few as 100 to 100,000 atoms within the quantum dot volume, with a diameter of 10 to 50 nm.

3.2.3 CQD Synthesis

A. Organometallic Method

After the organometallic synthesis method was introduced by Murray in 1993, with II-VI semiconductor cadmium chalcogenide materials, [53] lots of chemical synthesis methods have developed and been reported. Organometallic synthesis showed first success based on the organic ligand surrounded quantum dots. Cadmium Chalcogenide CQDs (CdE; E = S, Se, Te) were prepared in the inert gas environment using a high-temperature process. An advantage of this method is that the crystalline, monodisperse, and highly luminescent CQDs can be prepared with well-controlled and narrowly-distributed sizes. High reaction temperatures (200 °C - 300 °C) annealed out defects and improved crystallinity. Particle size was controlled mainly by the reaction temperature, with larger particles being obtained at higher temperatures. The average CQD diameter varied from 12 to 115 Å. This method is an innovation in the synthesis of high-quality, controllable CQDs, and activated further marvelous researches after.

B. High Injection Method

The method of rapid injection of organometallic precursors into another organometallic solvent at a high temperature is called the hot-injection method. This is another innovation to the synthesis of monodisperse CQDs. Through this hot-injection method, CQD particle sizes can be controlled in a very easy way. The hot-injection method

separates the synthesis process into two processes, which include synthesizing each organometallic precursor and rapid mixing two precursors with rapid injection in the hot reaction temperature. Nucleation and subsequent growth in time were achieved by reaction time and quenching of the reaction mixture. Quenching (or rapid cooling) of the mixed solution is known to prevent Ostwald ripening during growth, which is a critical factor in achieving a narrow size distribution. Following synthesis, QDs are precipitated from the growth solution and recast into a suitable solvent. Prior to their use in devices, they are usually precipitated and re-dissolved several times in order to eliminate excess ligands from the solution. Using hot-injection synthesis methods, it was possible to obtain monodisperse CQDs of a variety of materials with 5–10% standard deviation without post-preparative size fractionation.[74]

The high-temperature organometallic method and high-injection method has led to a dramatic increase in the number of groups to synthesize and investigate many II–VI semiconductor CQD systems. Following advances have been made in chemically synthesized CQDs with IV–VI, and III–V semiconductors. Each of these classes of materials has now been synthesized with narrow size distributions. Synthesis of IV–VI CQDs was realized by Murray and coworkers with the preparation of nanocrystalline PbSe in size from 3 to 15 nm. [75] Further approaches were explored by chemical modifications, where various Pb precursors, including PbO and PbCl₂, or Se precursors such as Se powder and trioctylphosphine selenide, as well as an array of solvent systems, including the non-coordinating octadecene, were employed. [76] Additionally, in 2003, the synthesis of PbS CQDs by the hot-injection method was first reported by Hines and

Scholes using the reaction of lead oleate and bistrimethylsilyl sulfide in octadecene. [77] Subsequent studies have also used PbO as the Pb source, and bistrimethylsilyl sulfide in trioctylphosphine, S in octadecene, or S in oleylamine as the S source. [78] After Hines made high luminescent CQDs. A major step toward the preparation of stable and highly luminescent CQDs was taken by Hines and Guyot-Sionnest, who passivated the surface using an inorganic wider-bandgap semiconductor capping shell. [79] In this thesis, we followed the last method which Hines introduced, which is using PbO and bistrimethylsilyl sulfide in octadecene solutions.

Uniform and less dispersed sizes of CQD is essential to produce a closely-packed, high quality CQD device. Chemically derived CQD with a uniform solution is crucial for systematic characterization of the structural, electronic, and optical properties of materials when it is fabricated as a thin film or self-patterned structure. The high temperature organometallic method with rapid injection opens a great pathway to the uniform, inexpensive and less dispersed CQD synthesis. Using colloidal method as explained, CQD has shown many interesting characteristics when it was made as a conventional condensed matter device, without losing its nano-size and nanophotonic properties.

3.3 Properties of PbS CQD

Lead chalcogenide QDs is promising to expand the current absorption spectrum to near infrared region of the solar spectrum, due to its considerably lower bulk band gap. PbSe

QDs have bandgap tunable from 1.1 eV (QD diameter ~ 4 nm) to 0.4 eV (QD diameter 16nm), [77] and PbS also can be tuned similarly (bulk PbS bandgap is 0.37 – 0.41 eV). In addition, this infrared QDs also strongly absorbs solar photons of higher energy (larger absorption coefficient at higher photon energy).

Solar cells based on a Schottky barrier formed at the interface of the PbS or PbSe QD films and a metal cathode have been reported, [9, 80-82] with PCEs of up to 2.1% under 1 sun AM1.5G test conditions. In these devices, it is suggested that photocurrent is generated by field-assisted charge separation in the depletion region. PbS has shown great performance with Schottky barrier photonic barrier. In addition, PbS QDs have generated strong research interest due to the discovery of multiple exciton generations (MEG) that possibly could boost quantum dots solar cell efficiency. [83]

Of particular interest to this work is the prospect of tunable absorption across near and shortwave infrared wavelengths. In this section, the synthesis and basic optical characteristics of nanocrystal QDs are reviewed.

3.3.1 Material Properties of PbS CQD

Size affects to various properties of QDs. QDs size can be controlled using reaction temperature and reaction time by quenching the reactive solution to the room temperature when the desired QD size is reached. QD size can be monitored by measuring the absorption spectra of an aqueous solution taken from the synthesized colloid. TEM images are also normally used for the successful size and crystallization control. For the crystallization of the QDs, XRD is usually used. According to the high-resolution TEM,

we can also observe the atomic structure and the distance between the atom layers to confirm the crystallization of the QDs. Fourier transform infrared spectroscopy (FTIR) spectra, Energy-dispersive X-ray spectroscopy (EDX) and X-ray photo-electron spectroscopy (XPS) analysis can be used for ligand analysis.

3.3.2 Optical Properties of PbS CQD

The quantum confinement effect increases the optical transition energy over that of the bulk material. This, in turn, enables the absorption band-edge to be precisely tuned to shorter wavelengths by reducing QD size. In the case of PbS ($E_g \sim 0.4$ eV) and PbSe QDs ($E_g \sim 0.3$ eV), spectral absorption can be tuned to shortwave infrared wavelengths. The absorption spectra for PbSe QDs is a range of core diameters as shown in Figure 3.7. The ease of spectral tunability combined with access to near-infrared and shortwave-infrared wavelengths make PbS and PbSe CQDs an attractive material for optoelectronic device applications. In particular, QDs make an excellent matching with various materials, such as semiconductor, oxide, and organic materials.

One can see discrete states in the absorbance though they are clearly inhomogeneously broadened. The lowest energy level is clearly seen and it is labeled as the first exciton peak. The first exciton peak is the transition from the unexcited state of the semiconductor to having one exciton in the lowest electron state. In this thesis, the plots in later chapters denote PbS quantum dots with 950 nm absorbance, which implies that the quantum dots have its first exciton peak at 950 nm.

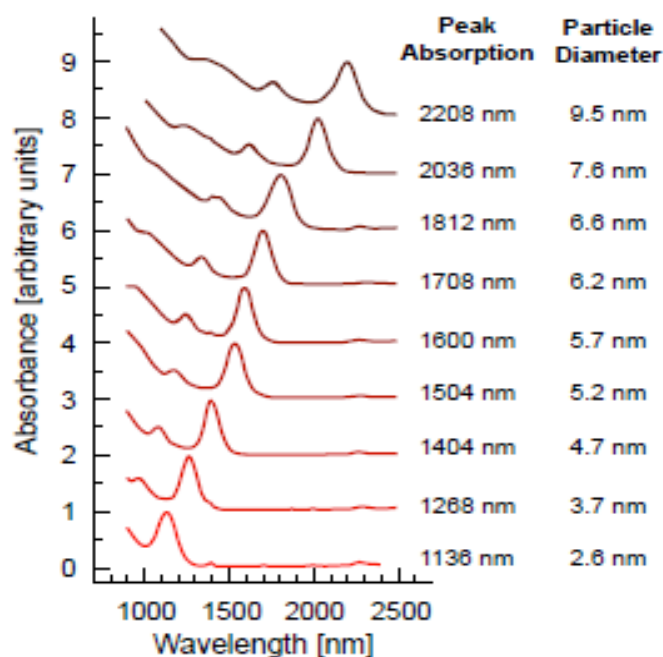


Figure 3. 7 Absorption spectra of PbSe QDs as a function of nanocrystal diameter.

Reproduced with permission from ref [84]. Copyright © 2003 WILEY-VCH Verlag GmbH & Co. KGaA, Weinheim.

3.3.3 Pb-Chalcogenide QDs for Photovoltaics

Bandgap tunability and favorable electronic properties make PbS QDs attractive for a diverse range of optoelectronic device applications. [81, 85, 86] In this thesis, we focused on the development of PbS CQD photovoltaic devices, which have seen particularly rapid progress as a potential material to surpass the Shockley-Queisser single-junction limits.

PV efficiency from QDs can be maximized considering a few factors, including Schottky junction, bandgap engineering and surface treatment.

A. Schottky Junction

Contacting PbS CQD films with metal electrodes, whether resulting in ohmic or Schottky character, plays a crucial role in the operation of electronic and optoelectronic devices. Charge transfer depends on the relationship between the alignments of the work function of the metal electrode with the energy levels in the PbS film. Forming a well-controlled Schottky contact to CQD films produces rectifying characteristics, rendering the system suitable for using as a photodiode and for photovoltaic energy conversion applications. [87] The extraction efficiency of photogenerated non-equilibrium carriers from the PbS CQD solid plays a key role in determining the performance of a solar cell.

The discrete nature of the electronic levels in PbS CQDs, which vary with size and surface chemistry, results in a size- and material- dependent optical characteristics. Au contacts can readily inject or extract holes into/from PbS CQDs larger than ~ 6 nm in diameter, whereas a potential barrier forms at the interface with smaller PbS CQDs. [88]

B. Bandgap Engineering

In order to increase the energy harvested from the broad sun spectrum, QD size tuning (funneling) and heterojunction solar cells are tried from a combination of CQDs of differing sizes and thus bandgaps. [89] PbS shows a great tenability in its absorption in near IR spectrum due to its low energy bandgap. However, the low energy bandgap causes the small open circuit voltage problem and resulting in low power conversion efficiency.

C. Surface Treatment

Colloidal synthesized QDs are generally capped by organic ligands that employ long chains (Oleic Acid in this thesis) to ensure their solubility. These insulating organic barriers between CQDs prevent efficient carrier transport from QD to the electrode when it is fabricated as a device. Therefore, much attention has been devoted to the development of new ligand strategies that minimize the insulating effect from organic chains. One of the brilliant research was performed by Tang et al., and they showed the 1,2-ethanedithiol (ETD) as a great passivating material as a post treatment. They report the first inorganic ligand-passivated CQD photovoltaics, achieving 6% solar power-conversion efficiency. [90] We also used the EDT as a post passivation material in this thesis.

Sargent group at University of Toronto studied the nature of long-living traps in PbS QDs and the effect of surface sites on the response time of PbS detectors. [80, 91] The treatment of QD films with different molecules can control the surface states and consequently response time. They fabricated a device with efficiency around 1.8%.

There has been much progress in improving the power conversion efficiency (PCE) of nanostructured solar cells in the visible light region with reported efficiencies reaching 6 %, [90] 7.0% with in-organic ligand exchange, [92] and even 8.85 % with band alignment with a semiconductor layer and ligand exchanging. [60] Among the QD materials, PbS and PbSe QDs possess excellent photosensitivity in the near-infrared spectrum. Semiconductor PbS with a bulk bandgap of 0.41 eV offer excellent size tunability across the near IR region and can be synthesized with an inexpensive and soluble process. We report here the synthesis of size-tunable PbS colloidal QDs. PbS

offer strong optical absorption due to the direct band gap. PbS also offers a great potential possibility to high efficiency via optimal utilization of the sun's broad spectrum and capacity to be band-gap-tuned to spectral positions optimal for efficient visible and infrared harvesting ensures that there exist no fundamental obstacles to achieving compelling high solar power conversion efficiencies.

The dots used in this thesis are grown by the injection of organometallic reagents into a hot coordinating solvent. The PbS QDs span their spectrum to the near-infrared which is very useful for photovoltaic and photosensitive devices. In this work the PbS QDs without a cap are used, which is strongly confined.

Solar cells based on a Schottky barrier formed at the interface of the PbS or PbSe QD films and a metal cathode have been reported by Luther et al., with PCEs of up to 2.1% under 1 sun AM1.5 test conditions. [9] In these devices, it is suggested that photocurrent is generated by field-assisted charge separation in the depletion region. One limitation of Schottky-based solar cells is the open-circuit voltage (V_{oc}) which is an important factor that directly affects the PCE. A heterojunction solar cell incorporating an electron-transporting/hole-blocking layer between the QDs and the metal cathode could potentially allow for a higher V_{oc} . Still there is a challenge in realizing such a device with the current mechanism of the device. So we proposed a novel mechanism of a ferroelectric domain wall effect and implemented to the PbS-PZT photovoltaic device and showed higher V_{oc} .

To overcome the efficiency limitation of QD device, we proposed a novel mechanism for next generation solar cells. CQD uses Schottky or ohmic junction structure for PV

devices. If we can use bulk area carrier transportation mechanism which is observed at ferroelectric materials, new mechanism can be proposed with hybrid structure. Furthermore, we suggested that spontaneous polarization can improve the carrier transportation or hinder the transportation according to the polarization directions. CQD also can improve poor ferroelectric bulk DC conduction. Ferroelectrics are basically insulators as it has poor bulk carrier transportation and poor solar spectrum absorption by wider energy band gap. If CQD and nano-sized ferroelectric particle are mixed with device architecture engineering, there is a great possibility of improving solar efficiency.

Chapter 4. Synthesis and Fabrication of PZT NPs and PbS QDs

Overview

Great efforts have been exerted on the synthesis and fabrication of ferroelectric perovskite oxides with the development of thin film deposition techniques. Ferroelectric materials can be prepared by various methods. [22, 31, 34, 39, 93-97] There are chemical methods, such as hydrothermal methods, chemical solution deposition, sol-gel process, and physical methods such as the vacuum deposition method, pulsed laser deposition, sputtering. [16, 98] In a big group, it is normally categorized into a physical and chemical method.

A. Physical Method:

There are several vacuum deposition techniques, which have been proved that this technique can obtain precise composition control and also been widely utilized for the deposition of high quality ferroelectric thin films, such as molecular beam epitaxy (MBE), pulsed laser deposition (PLD), metal-organic chemical vapor deposition (MOCVD) and sputtering. [31, 44, 94, 99, 100]

Those physical deposition technologies have advantages in their relatively simple operation, good composition control and capable epitaxial growth of ferroelectric materials. However, it requires bulky and expensive machines, and it is not so compatible with suspension nanoparticles.

B. Chemical Method:

However, the chemical processing method such as hydrothermal or sol-gel methods provides suitable properties such as solubility or volatility, control of stoichiometry for multi-metallic arrays with inexpensive fabrication costs. Among those, the sol-gel method is known to produce materials from solutions either in bulk, coating films, fibers or powders, porous materials, ceramics, organic-inorganic hybrids and nanocomposites. The sol-gel method also can achieve the good quality with low-temperature processing. The significance of the sol-gel method consists in easy-to-modify of processing and creation of novel materials. [16, 101]

This chapter presents a brief overview of the general chemistry of the QDs and sol-gel method as well as its use in the fabrication of thin films. Improvements in the properties of 2-methoxyethanol based sol-gel films and its application of nanoparticles through modification of the precursor chemistry are described as well. Their use in the fabrication of thin films will be explained in the following sections.

4.1 Fabrication Techniques

In early studies of PZT thin films, physical vapor deposition (PVD) techniques were used to prepare the films. These included RF magnetron sputtering using a bulk PZT target, and reactive RF sputtering of a metal target [34]. Laser ablation [99] and chemical vapor deposition (CVD) also have been utilized to prepare these films. [14]

RF magnetron sputtering is the deposition technique which uses the plasma energy to deposit a thin film on the substrate from the stoichiometric ceramic target. For example, PZT thin films on various substrates are deposited from a PZT ceramic target giving 4W power at 20 - 250 °C substrate temperature, at Zhenxing Bi et al.'s study. [102]

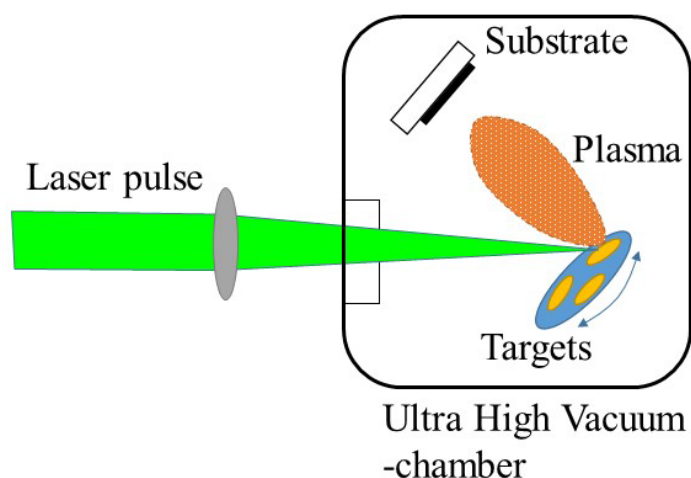


Figure 4.1 Schematic diagram of a typical laser deposition set-up.

Pulsed laser deposition (PLD) is the method that thin films are prepared by the ablation of one or more targets illuminated by a focused pulsed-laser beam. Smith and Turner were the first people to use this technique in 1965 for the preparation of semiconductors and dielectric thin films using a ruby laser. [103] PLD was established due to the work of Dijkkamp et al. [104] on high-temperature superconductors in 1987. Their work showed the principle of PLD, which is the stoichiometry transfer between the target and deposited film and high deposition rates of about 0.1 nm per pulse. Since the work of Dijkkamp et al., this deposition technique has been intensively attracted for all kinds of oxides, nitrides, or carbides, and also for preparing metallic systems and even

polymers or fullerenes. A typical set-up for PLD is schematically shown in Figure 4. 1. In an ultrahigh vacuum (UHV), chamber, elementary or alloy targets are struck at an angle of 45° by a pulsed and focused laser beam. The atoms and ions ablated from the targets are deposited on substrates during the operation. Mostly, the substrates are attached on the surface parallel to the target surface at a target-to-substrate distance of typically 2 -10 cm. [99]

PLD has advantages in the viewpoint that there is little difference in the composition between the target material and the deposited film, and that it is possible to crystallize the films at relatively low substrate temperatures. This is because atoms ejected from the target has a relatively high energy compared with that of thermal evaporation. And even materials with a high melting point can be easily deposited if the materials strongly absorb the laser light. This is both versatile and expensive technology, resulting it being used mainly for research, not on an industrial level.

Metal-organic chemical vapor deposition (MOCVD) is a popular thermodynamic technology used in a semiconductor process. MOCVD uses ultra-pure gasses injected into a reactor and finely deposits a very thin layer of atoms onto substrates with a high temperature. It has an advantage of high flexibility for deposition from semiconductors, metals to dielectrics. [105] However it is highly toxic, a source material is very expensive, and environmental disposal costs are high. Normally in a semiconductor factory where MOCVD equipped, it needs huge facilities of scrubber and disposal lines, which adds to the increasing cost. Figure 4.2 shows the principle of an MOCVD process.

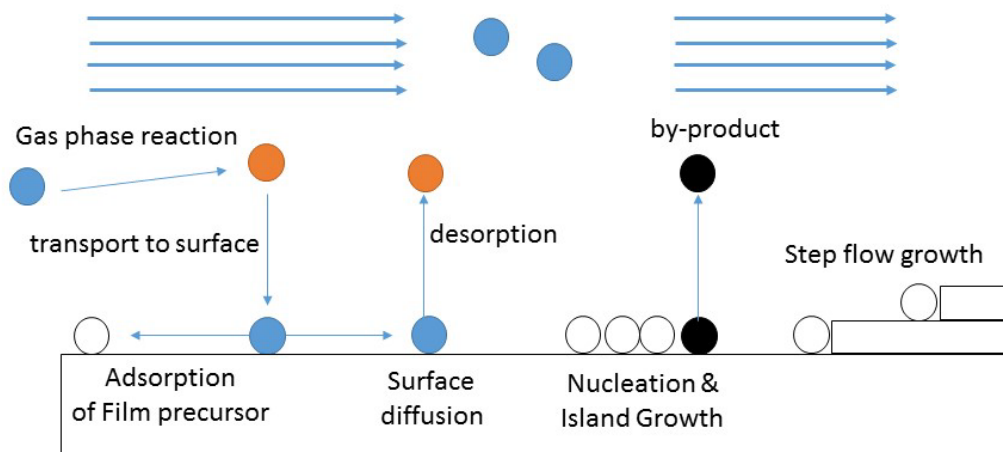


Figure 4. 2 Schematic diagram of MOCVD principle for PZT thin films.

MOCVD process has a few steps. First, the chemicals are vaporized and transported into the reactor with other gasses. Then, the critical chemical gas-phase-reaction takes place. And it turns the chemicals into the desired crystal on the substrate. Second, on the attached molecule crystal, the same structure of the molecules stack up and this is called epitaxy, of which the name comes from the Greek meaning “arrangement” or “order”. This accumulated layer will form thin films. During the process, desorption will also occur, but if the absorption rate is higher than desorption, the thin film will grow.

Physical techniques such as sputtering, MOCVD and PLD was used for PZT thin film fabrications. [31, 34, 41, 100, 106] These techniques formed high-quality PZT thin films, such as epitaxial growth, layer by layer stacks on the substrates. However this is expensive and does not have much room to change the method, so it is less interesting for soluble nanocomposites fabrications.

4.2 Sol-gel Method

Among the chemical method, the sol-gel method has been widely studied [16]. The sol-gel technology has specially developed within the last two decades. Considering the micro- or nano- structures, the sol-gel method can be applied from porous materials, dense materials such as glasses and ceramics to nano-composites. It is also known that this method enables solution based and low-temperature processing, which has advantages of low prices, less substrate damage and the fact that it is easy-to-handle. The sol-gel method is good candidate solution process which can be applied for bulk heterojunction (BHJ) devices using colloidal based material or organic based material. [16] We consider sol-gel is the most applicable to nano-composite with a feasible process. So, this section will explain a brief overview of the general chemistry of sol-gels, the types of PZT sol-gels, and their synthesizing processes.

Metal Alkoxide is one of the popular methods to make sol-gel precursors because it can be transferred easily to non-organic materials, and it is easy to fabricate. Furthermore, it has less toxicity and easily melts in the solution with alcohol ligands. An alkoxide consists of an organic group bonded to a negatively charged oxygen atom. They can be written as RO⁻, where R denotes an organic substance or alkyl radical (such as methyl (CH₃), ethyl (CH₂CH₃) or others). Likewise, metal alkoxide can be written as M(OR)_n where M (Metal) is combining with one or more of R (alkyl group) with the help of oxygen. The formula is as below for sol-gel process. Here ‘n’ denotes valence number.



The first step is to make alkoxide. When the covalent halogen compound which is MX_n reacts with alcohol, alkoxide with a stronger covalent force will be made. This process normally occurs when metal or non-organic material is mixed in the organic solution with a certain reaction temperature. Normally a few different metals attend the process of alkoxide to make a complex compound material. This alkoxide state is also called 'sol' which is a uniform mixture of solution.

The next step is hydrolysis. Hydrolysis mechanism will make alkoxide to gel and the formula is as below. The gel is the state of being linked together to make a wide connection between alkoxides. Metal alkoxide hydrolysis makes one or more alkoxy group to a hydroxyl group. At this time, alcohol will be generated as a reaction product. The hydrolysis consists of replacing one OR group on the alkoxide with a hydroxyl ion (OH), releasing an alcohol molecule in the process.



Most of the alkoxy will form hydroxide or hydrated oxide easily when it gets in contact with water. Oxide materials will, therefore, be condensed to hydroxyl group as shown below.



Throughout the process (4.1), (4.2) and (4.3), $2M(OH)_n$ will be formed as a final product with $2MO_{n/2}$ and nH_2O being produced last. $2M(OH)_n$ also written as M-O-M denotation.

By definition, condensation releases either alcohol or water, depending on the initial compounds. We can say that condensation is the reverse reaction of hydrolysis. If hydrolysis and condensation reactions of the metal alkoxide exceed the level, macro-molecules containing many M-O-M segments will form and depending on the reaction speed (normally by reaction temperature), form precipitates or extend throughout the solution which will eventually become a highly viscous or solid gel. These reactions can take anywhere from the duration of < 1 second to weeks.

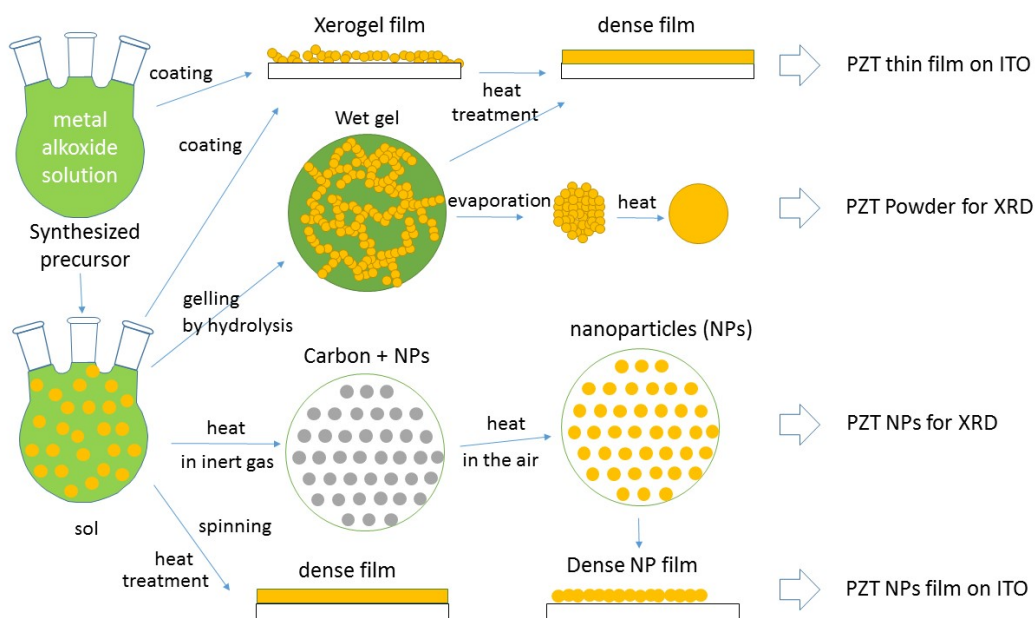


Figure 4. 3 General schematic diagram of sol-gel formation and the resulting material and the devices in this thesis.

The hydrolysis and condensation reactions are a reversible process. The speed of the reaction depends on the concentration of the initial compounds as well as the reaction

temperature. If the hydrolysis and condensation reaction reaches equilibrium with its reverse reaction, the solution will never be the gel in a sealed container. We call it as a stable sol solution in this paper. By varying the amount of water or alcohol, it is possible to control the speed of each reaction and shift the equilibrium in either direction. More importantly, it is possible to ‘stop’ the hydrolysis/condensation reaction in the solution and make a stable sol solution in the sealed container. ‘Stop’ in the sentence above means to inhibit the reaction because the solution is easily changed to gel by the humidity from the outside of the containers or in a room environment. If one were to add water to a stable sol, this would increase the speed of the forward reactions, and would shift the equilibrium toward hydrolysis. If enough water is added to the solution, the sol-gel solution will become a gel. This gelation is actually desirable for the fabrication of thin film spin coating, but we think that gelation is not good for nanoparticle synthesis. Because theoretically gelation will make a big chunk of the link between metal alkoxide as shown in Figure 4.3.

There are various processes and chemicals for sol-gel methods. In this research, we tried two major sol-gel methods which are acetic acid based sol-gel and 2-methoxyethanol based sol-gel.

A. Acetic Acid Based Sol-Gel:

The first approach was an acetic acid based system of which we referred the synthesis method from Chao Liu et al. [107] In this method ferroelectric PZT precursor liquid was prepared. The basis of the acetic acid sol-gel rests with the property of an acetic acid to slow the hydrolysis and condensation reactions of transition metal alkoxides by forming more stable metal alkoxo-acetylates [101]. The original solution is prepared by dissolving lead acetate trihydrate $[\text{Pb}(\text{C}_2\text{H}_3\text{O}_2)_2 \cdot 3\text{H}_2\text{O}]$ in acetic acid $[\text{CH}_3\text{COOH}]$. And the solution usually refluxed overnight. Then 50% - 90% of the acetic acid was distilled to minimize the amount

of water in this Pb starting reagent. The zirconium propoxide [$\text{Zr}(\text{O}(\text{CH})\text{CH})$] (70 wt% in propanol) and the titanium isopropoxide [$\text{Ti}((\text{CH})\text{CHO})_4$] were then added to the acetic acid and lead acetate. To prevent the humidity from outside, all the process was proceeded in the inert flask with Ar gas. Slightly higher lead concentration (normally 10% higher) was intended to compensate the loss of Pb in the subsequent thermal treatment. The solution was stirred at 50 °C overnight to reach a transparent form. For a trial of the nanoparticle, ammonia was slowly added with Ar gas to bubble through this mixture solution, pH of this solution was increased to allow the nanoparticulate precursor to grow slowly. While this acetic acid method was believed to be a comparably stable and well controlled reaction, still there are the difficulties of PH, humidity control and a drawback in its long reaction time.

B. 2-methoxyethanol Based Sol-Gel:

A second sol-gel process is based on the solvent 2-methoxyethanol. In this method, a ferroelectric PZT precursor liquid was prepared and consecutive PZT nanoparticles were fabricated by inert gas annealing and ultra-sonication processes. The ratio of Zr : Ti = 53% : 47% was chosen from the ratio which would show the best ferroelectric properties. [25, 32] The precursor materials were lead acetate trihydrate, zirconium propoxide and titanium isopropoxide. These precursors were dissolved into 2-methoxyethanol. A typical synthesis was started with dissolving 0.4M of lead acetate trihydrate ($\text{Pb}(\text{CH}_3\text{COO})_2 \cdot 3\text{H}_2\text{O}$; 99.5%, SigmaAldrich, USA) in 2-methoxyethanol at 80 °C for 2 hours. We weighed 0.4M of lead acetate and added 10% more to recover the evaporation loss. [108] Before dissolving in the 2-methoxyethanol solution, lead acetate powder was weighed and dried at 125 °C for 1 hour to remove the water from the acetate. 2-methoxyethanol was injected with a syringe into a vacuumed flask. Magnetic stirring was used for 30 min to get a uniform solution.

After lead acetate was dissolved into the solution, 0.4 M titanium isopropoxide ($\text{Ti}[\text{OCH}(\text{CH}_3)_2]_4$; Aldrich, USA) was added to the lead-dissolved solution. In order to make sure that all titanium and the lead solution was well mixed, the mixture was stirred vigorously. When all the lead and titanium were dissolved in the 2-methoxy ethanol, then only a transparent solution remained. This transparent liquid was the lead titanate precursor solution. Using the same method, 0.4 M of zirconium propoxide ($\text{Zr}(\text{OCH}_2\text{CH}_2\text{CH}_3)_4$, 70 wt. % ;Aldrich, USA) was mixed into the lead titanate precursor solution. The solution was stirred at 80 °C until it turned into a transparent and uniform solution. This PZT precursor solution was a morphological mixture of each Pb, Zr and Ti material.

As for the hydrolysis and catalyst, deionized (DI) water and nitric acid (HNO_3) was added to the PZT solution in the following manner. After preparing 1:1.5 of the molar ratio for PZT and DI water for hydrolysis, nitric acid was added into this PZT solution. The solution was prepared by adding ethylene glycol to produce PZT thin film devices with higher viscosity. Any additives such as DI water, nitric acid or ethylene glycol was not added to the main colloidal solution when we make PZT nanoparticles, because it was considered not helpful to the formation of nano-sized particles with the complex linked gel solution.

The 2-methoxyethanol reacts with the metal alkoxides to act effectively as a multi-ligand agent which prevents the complete hydrolysis of the metal alkoxides with the addition of water. For this method, it is comparably easy to control the hydrolysis and condensation reactions. So we put in more focus on the 2-methoxyethanol based sol-gel method. In this thesis, all the PZT thin film made from a sol-gel spin coating or PZT nanoparticle devices was made by 2-methoxyethanol based sol-gel method.

4.3 Fabrication of PZT Sol-Gel Thin Film Devices

4.3.1 Deposition

For the thin film fabrication, dip coating, and spin coating methods are typically used to create a thin sol-gel layer onto the substrates. However, Spin coating has been used extensively in the modern semiconductor industry than dip coating. Liquid sol-gel is deposited on a substrate with a spin speed of 2000-4000 rpm. This causes the liquid to be flat on the substrate uniformly by high rpm (revolutions per minute) and will not be too thin by the viscosity of the solution. If the rpm speed is faster, the uniformity of the film will improve but the thickness will become thinner. If the spin speed is slower, we can get thicker film but the uniformity will not be as good as that of higher speed coating. A diagram of the spinning process is illustrated in Figure 4.4.

First, the solution is dropped onto the substrate. The spin coater is then activated and centrifugal forces expel most of the liquid. The increasing viscosity of the liquid due to the evaporation of the solvent resists the flow caused by the centrifugal force causing the film to get dense. When coating a film using a sol-gel, after drying, the as-deposited film is an amorphous gel of metal-organic compounds. In order to eliminate the organic components and make a crystalized PZT, the film needs pyrolysis, which involves heating to approximately 120-300 °C between each time of spin coating. Finally, the film is annealed at the target temperature for crystallization, of which the temperature is normally over 500 °C for PZT thin films.

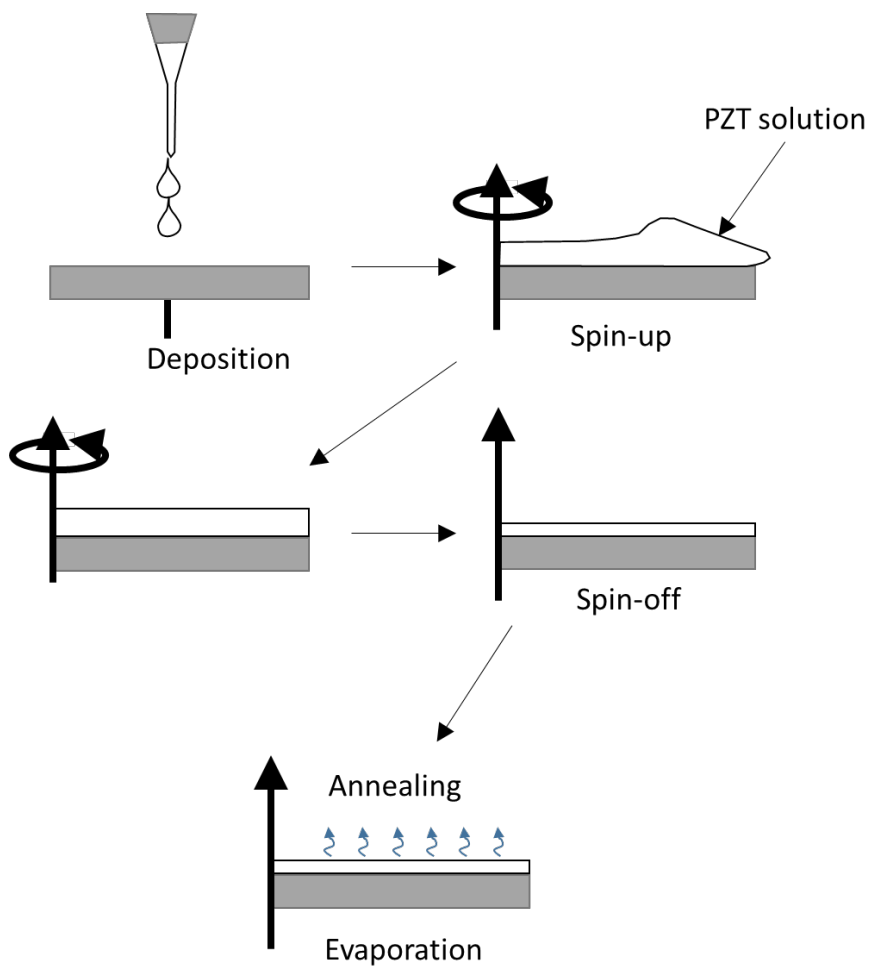


Figure 4. 4 Spin coating method.

The advantage of spin coating is the level of control it provides since the thickness of the layers can be controlled by adjusting the spinning speed and duration, without having to change the solution. In this research, synthesized PZT sol-gel solution was spin coated on CTO such as ITO and FTO substrates. Spin coating speed for PZT sol-gel was 3500 rpm for 30sec at one-time coating. The coated device was annealed at 600 °C and spin coated again to increase sufficient thickness of the film.

4.3.2 Thermal Processing

After spin coating and drying the PZT sol on the substrate, a high-temperature thermal treatment is required for crystallization. After drying the film, the amorphous metal-organic gel should convert to an amorphous layer of inorganic metal oxide compounds. In this stage, still amounts of organic carbon might be left in the film which will inhibit the proper crystallization of the film during the annealing.

The method of thermal processing is important. The film need to be annealed at 500 °C–700 °C for crystallization for PZT. While the film is cooling down back to room temperature, perovskite PZT structure is formed. So, several times spin coating the PZT thin film device was annealed at air atmosphere at 580 °C or 600 °C for 30 min. And the film devices were cooling down naturally down to room temperature in the furnace. When PZT film is baked at the high temperatures, normally 580 °C or 600 °C, the PZT layer will melt down and will become crystallized when the temperature is going down. When we quench the PZT thin film at a temperature of 400 °C or above, the film was not crystallized well.

One more important factor in this thermal process is the substrate. ITO knew that endures up to 300 °C, below glass up to 400 °C while PZT needs over 500 °C for crystallization. However, we successfully fabricate PZT thin film device with ITO and FTO (F:SnO₂). FTO is generally known that it is more stable and will not degrade when it is annealed at high temperature compared to ITO or ZnO substrates and showed high crystallization. [109]

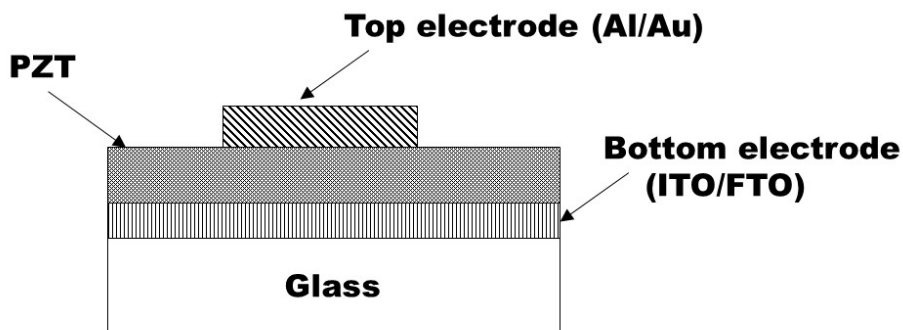


Figure 4. 5 Cross section of the ferroelectric PZT capacitor

Figure 4.5 depicts the structure of a PZT thin film capacitor. The bottom electrode is ITO or FTO on the glass, and on top of that, the PZT thin film was spin-coated. Like other metal depositions, thermal evaporation was used for Al (or Au) deposition on PZT capacitive device. Al electrode was thermally evaporated on the device at the pressure level of 6×10^{-6} Torr with $0.3 - 0.8 \text{ \AA/s}$ deposition rate, using 0.06 cm^2 dumbbell shape shadow mask. The details and results are discussed in Chapter 4.

4.4 Fabrication of PZT Nanoparticle Film Devices

There was a story about a ceramist who could make very light but thermally enduring china with lots of tiny air bubbles inside the pottery in ancient Korea and Japan. They made a multi-pore china and annealed it with straws in a sealed kiln. Burning straws would consume all the oxygen inside a kiln, and china would be fired with burning charcoal. In this rare oxygen environment, the carbon element in china cannot be changed to carbon dioxide (CO_2) and left a residue inside. Following that, oxygen annealing in an unsealed kiln would make

the carbon residues out as a form of carbon dioxide to make the micro-pores of the china. The HRSI(High-temperature reusable surface insulation) tile which used on the bottom of the space shuttle also made by similar ways. HRSI was composed of high purity silica fibers. Ninety percent of the volume of the tile was empty, giving it a very low density (9 lb/cu ft or 140 kg/m³) making it light enough for spaceflight. We could not confirm more detail facts and couldn't confirm the real process of ceramics from other document references or another source of materials, but this is the starting idea of making PZT nanoparticles.

We followed conventional PZT sol-gel method to make the PZT sol. Before adding DI (Deionized) water for the hydrolysis, the precursor solution was heat-treated in an inert gas atmosphere and the temperature was around 380 °C – 500 °C. Without any oxygen, an organic material composed of carbon compounds cannot be removed even by high heat treatment, because at high temperatures, oxygen is needed to combine with carbon and be removed from the solution as a form of carbon dioxide (CO₂). So only black carbon ash residue will be left between PZT inorganic compounds and occupy space between metals which were originally was metal alkoxides. After this process, black PZT ash was annealed at 580 °C or 600 °C. In this stage, residual black carbons will be removed as a form of CO₂ and make a blank space between PZT nano-crystals.

Though the particles are small, it is quite easy to agglomerate at high temperatures. So, ultrasonication was used for separating each nano-sized particles. Figure 4.6 shows the mechanism of PZT nanoparticle formations.

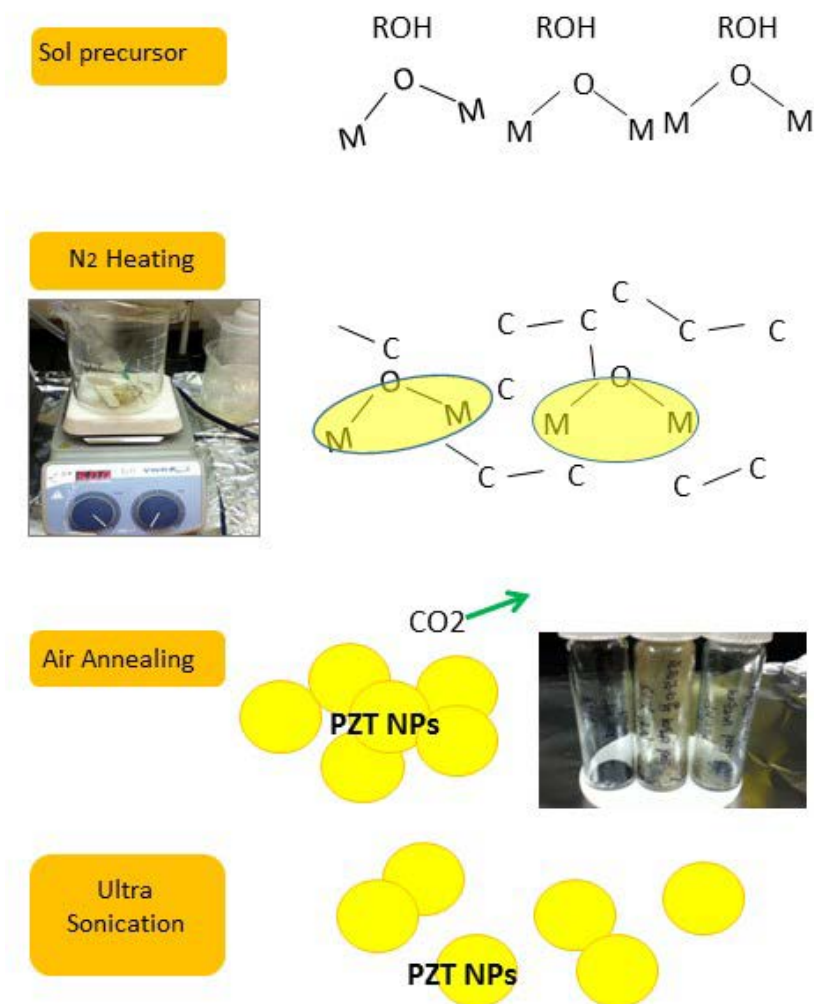


Figure 4. 6 Schematic diagram of the mechanism of PZT nanoparticle formation and inert gas contributions

Sol precursor consists of a metal alkoxide, M-O-M structure. This is surrounded by organic materials with ROH in the schematic above. These sol precursors were heat treated in the nitrogen filled glove box, then organic materials changed to black carbon powder.

Following oxygen annealing will remove residual black carbon as a form of CO_2 . The final material will be nano-sized PZT powders.

If we kept the hydrolysis and condensation process in PZT precursor solution, a white precipitated gel was formed. This white precipitated gel was centrifuged at 4500 rpm for 45min to extract PZT nano-composites. Then the PZT nano-composites were treated under an Ar or N_2 gas flow furnace at 500 – 700 °C for 1 hour and turned into black colored powder. It is the same procedure in Figure 4.6 and it is assumed that the black color is from the carbons converted from organic compounds surrounding the PZT nanostructures. The only difference is the PZT material which is ‘gel’ this time. After the secondary annealing process at 600 °C under oxygen rich ambient for 30 min, the carbons surrounded PZT nanostructure was disappeared and the same light yellow color powder was the final products. Finally, in order to separate the PZT crystalline nanoparticles, ultra-sonication was followed.

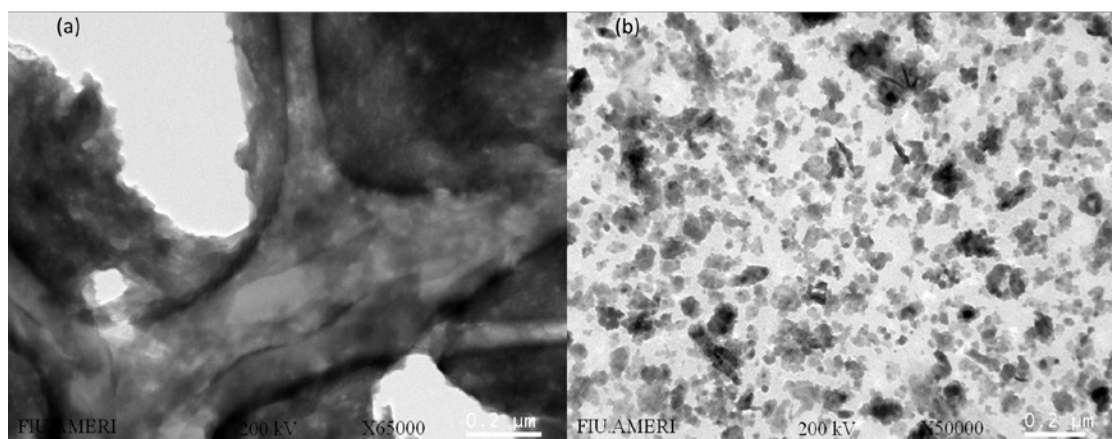


Figure 4. 7 TEM image of the final product from (a) PZT gel and (b) PZT sol, after the nanoparticle synthesis process explained in Figure 4.6.

Figure 4.7 (a) is the TEM image of the light yellow powder made from PZT gel after hydrolysis and centrifuge it for separating from sol solution. Because this is made from a gel compound, the powder is big in size in TEM image. Figure 4.7 (b) is the TEM image of the light yellow PZT nanoparticles made from PZT sol based solution which made without hydrolysis process. The size of the particle was nano-sized and had a uniform distribution. So we can confirm that a PZT nano-sized particle can be produced without hydrolysis more effectively. And following ultrasonication separates particles much more effectively.

With the successfully synthesized PZT NPs, we drop cast water-based PZT NP solution on the ITO substrate. Since PZT NPs is already cooled down to the room temperature when it is formed as a nano-size particle, any temperature-sensitive substrate can be used such as a flexible or ITO coated glass substrate. 40mg/mL concentration of PZT NP and DI water solution is used for drop cast. 0.1 mL solution is dropped on the ITO substrates using a syringe each time. After dropping the PZT NP solution, the device is dried on 80 °C hot plate for 5 min. It is repeated until the 2 mL of PZT NP solution is deposited on the substrate. The final device is the ITO/PZT-NP/Al capacitive structure device. In this case, the thickness of the PZT NP film is 10 μm on the ITO substrate. We will discuss the details and results in Chapter 5.

4.5 Synthesis of PbS Quantum Dots

PbS nanocrystals were synthesized by a method derived from other research group and confirmed its quality by checking the optical properties later. [77] The synthesis of PbS nanocrystals was performed in two flasks, one for lead (Pb) solution and the other for sulfide

(S) solution. The lead oleate precursor was prepared in situ by heating PbO in oleic acid (OA) at concentrations 0.2M under Ar at 160 °C for 1 hr. A solution of bis(trimethylsilyl)sulfide (TMS) in octadecene (ODE), a non-coordinating solvent, corresponding to a molar ratio of 2:1 Pb/S was prepared in another flask and injected into the vigorously stirring lead oleate solution at 160 °C. Trioctylphosphine (TOP) has also been used as the dilution solvent for the TMS without any perceivable effect on the resulting nanocrystals. Given that TOP is basic in chemical nature and much more reactive than ODE, it could play a greater role in the nanocrystals growth than has been observed. A typical synthesis involved 0.09g PbO dissolved in 4 mL OA, into which 42 μ L TMS in 2 mL ODE was injected. The heating mantle was lowered away from direct contact to the reaction flask immediately after the target reaction time and target temperature for nanocrystals growth, for example at 120 °C / 5 sec. The solution in the flask was quenched with acetone cooled in the refrigerator. In addition, the whole flask was emerged in the iced water for about 10 min, in order to stop the reaction rapidly and reduce the PbS size distribution.

Chapter 5. Photovoltaic and Ferroelectric Properties of $\text{Pb}(\text{Zr}_{0.53}\text{Ti}_{0.47})\text{O}_3$ Thin Films under Dark and Illuminated Conditions

5.1 Overview

Thin films of $\text{Pb}(\text{Zr}_{0.53}\text{Ti}_{0.47})\text{O}_3$ (PZT) were prepared by the sol-gel method. The photovoltaic response of the film under dark and illuminated conditions was investigated using capacitor type devices with Aluminum (Al) as top and FTO bottom electrodes. A metal/ferroelectric/metal (MFM) structure was used for electrical property measurements and the film was characterized by I-V, photocurrent, P-E hysteresis and optical transmission and absorption. V_{oc} and I_{sc} are 0.15 V and $0.18 \mu\text{A}/\text{cm}^2$ respectively. Remnant polarization ($P_r = 0.5 \mu\text{C}/\text{cm}^2$, $E_c = 125\text{kV}/\text{cm}$) was also observed for the PZT thin films. The value of the optical band gap was found to be 3.0 eV. The results are discussed with the energy band gap model.

5.2 Background

PZT is not only a ferroelectric material but also optically transparent in visible range, therefore using PZT makes a device for optical applications such as optical MEMs, a photo sensor or photovoltaic device are a smart choice. [20-22, 44, 96, 110] Recently, PZT thin films on ITO substrates has been studied for its use in photovoltaic (PV) applications, hybrid with organic materials. [111] Nevertheless, not so many studies

were performed, because of the difficulty to coat PZT sol-gel solution on ITO substrate, (mostly the degradation of ITO while heat treatment). One successful device fabrication was done by Cao, et al. [19] They demonstrated that the insertion of an n-type cuprous oxide (Cu_2O) layer between the PZT film and the cathode Pt contact in an ITO/PZT/ Cu_2O /Pt cell leads to the short-circuit photocurrent increasing 4.80 mA/cm^2 and 0.42 V for V_{oc} . while ITO/PZT/Pt layer showed $40 \text{ }\mu\text{A/cm}^2$ range, 0.56 V for V_{oc} . This was one of the successful achievements from PZT on transparent conductive oxide (TCO) substrate. However, they used copper oxide layer on the PZT thin film, and pure TCO/PZT/Al structure was not reported yet, as we know of. Nevertheless, TCO has its difficulties in high-temperature heat treatment. We also fabricated the photovoltaic capacitor device through high-temperature treatment and checked the basic electrical and optical properties for the further progress of PZT NPs and PZT thin film hybrid devices which will be discussed in the next two chapters. In this research, we made FTO/PZT/Al structure device and measured the I-V, photocurrent and leakage current as electrical properties. Also, we measured transmittance, absorption to check the optical properties of the device. As we know of, FTO/PZT/Al structure is not much studied and we report this structure for the first time.

As we discussed in Chapter 2, ferroelectric materials have spontaneous polarization inside the material. We also discussed that this built-in polarized field is responsible for the PV effect in ferroelectrics. [23] Furthermore, we discussed that the control of this field can be used to tune their photovoltaic properties in the previous chapter. So, we checked the ferroelectricity first through P-E hysteresis loop, to see if there was a ferroelectric spontaneous polarization in the PZT thin film on FTO substrate.

Molecular structure and electrical properties of PZT are sensitive to the Zr : Ti ratio [31, 41]. Thus, the choice of composition is crucial by the particular application. So, we used the ratio of Zr and Ti as 53 : 47, which is well known for the best ferroelectric morphology for the PZT. [25]

The effect of annealing, morphology and its relation to molecular structures and ferroelectric properties, was reported earlier in Chapter 3. We chose transparent electrode with ITO and FTO, and the substrate was better for PZT thin film device. Finally, the purpose of this work was to study the photovoltaic and ferroelectric properties of these films under dark and illuminated conditions, and future application for the advanced PV devices using ferroelectric PZT layers.

5.3 Experiment

To prepare the PZT (Zr : Ti = 53 : 47) films, the sol-gel solution was prepared in a fume hood using 2-methoxyethanol sol-gel method. Zr-propoxide and Ti-isopropoxide were added to the solution to intermediate heating and cooling. The final concentration of the solution was prepared in 0.4 M (molar). The detailed synthesizing method is the same as in Chapter 3. Figure 5. 1. (a) shows the summary flow chart for the PZT sol-gel synthesis.

For J-V and photo-current measurement, 600 nm thick PZT films were prepared by spin coating on commercially available FTO/glass substrates. As-grown films were post annealed in a furnace at the temperatures of 580 °C for 30 min. 100nm of Al was

thermally evaporated at a vacuum level of 6×10^{-6} Torr, with a deposition rate of 0.3 – 0.8 Å/s, and the deposited Al electrode has a 0.06 cm² size with a dumbbell like shape.

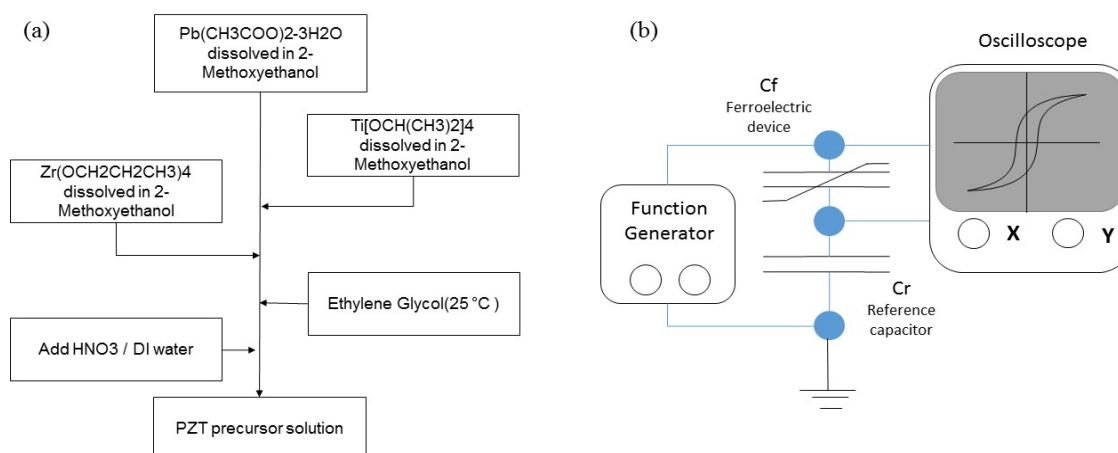


Figure 5. 1 (a) PZT sol-gel synthesizing method for PZT thin film device. (b) Sawyer-Tower circuit and peripheral equipment setup

Siemens 500D X-ray Diffractometer was used for XRD analysis. The measured X-ray peak was compared to JCPDS card and confirmed the material structure. A source meter and a computer were used to measure the photocurrent and I-V characteristics and acquisition of data under dark and illuminated conditions. The sample was illuminated from the top using a Xe light source with an air mass filter. The intensity of illumination was calibrated as AM 1.5 (100mW/cm²). All the measurements were carried out using a top-bottom capacitor configuration and the light source was illuminated from the bottom of the FTO substrate. The voltage bias was applied to the bottom electrode and the

current was measured using a source meter (Keithley 2400), which was interfaced to a computer for data acquisition.

Hysteresis characteristic was measured by the home made Sawyer-Tower circuit and the data was acquired by an oscilloscope which was connected to the computer. The Sawyer-Tower circuit setup was shown in Figure 5.1 (b). This method was introduced in 1930 for the first time, but it is still very practical for the characterization of ferroelectrics and study of fundamental phenomena such as spontaneous polarization, remnant polarization, coercive-field and polarization reversal mechanisms. The circuit consists of two capacitors, one is the ferroelectric sample (C_f) and another is a reference-capacitor (C_r). They are in a series, where C_r is chosen much greater than C_f so that the voltage drop across C_r is much less than the voltage drop across C_f (sample). So the drive voltage V_d is almost equal to the voltage across C_f . The voltage across the C_r , which gives polarization of the sample, is applied to vertical plates of the oscilloscope and the drive voltage after safe attenuation is applied to horizontal plates of the oscilloscope to measure the electric field across the sample. [17] For the optical properties, Spectrometer (Stellarnet) was used for measuring optical properties such as absorption and transmittance.

5.4 Results and Discussion

As we discussed in Chapter 2, PZT has different phases according to the ratio of Zr/Ti. When Zr is less than 50 %, the phase is in tetragonal phase. If Zr ratio is at around 53 %

tetragonal and rhombohedra will be mixed and if a higher ratio of Zr is in rhombohedra phase (Figure 2. 10 in Chapter 2).

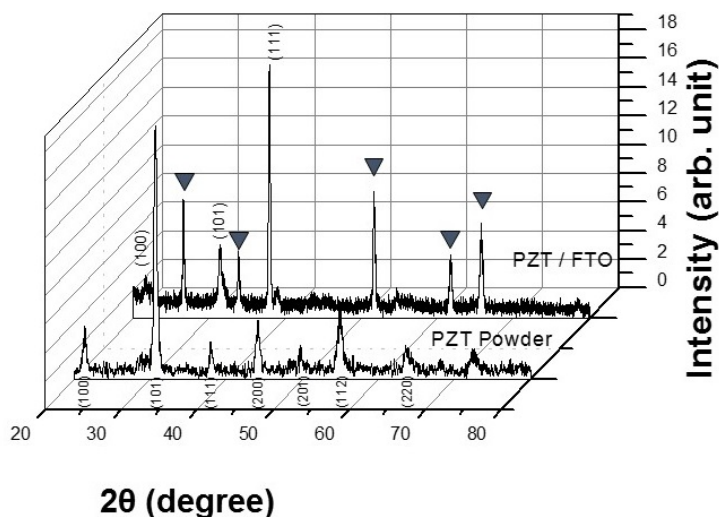


Figure 5. 2 XRD pattern of sol-gel synthesized PZT(53:47) powder and PZT/FTO. And “▼” represent the FTO peaks.

Figure 5.2 displays an XRD pattern in the pure PZT film on FTO-coated glass, showing that the PZT film has a polycrystalline perovskite structure. [112] Peaks from the PZT powder show that the sol-gel derived PZT was made as a perovskite structure. The triangular mark, ▼, is FTO peaks in the figure. The powder was annealed at 580 °C for 30 min. Figure 5.2 shows the phase was transitioned to the rhombohedra phase. We observed (101) as the main peak from the PZT powder, which represents the crystal is mainly rhombohedra structure. [113] Still we observed small peak height of (100), which is a tetragonal phase.

Figure 5. 3. (a) displays the representative current density–voltage (J–V) characteristic of the ferroelectric photovoltaic (FE-PV) devices, recorded under 1-sun which is AM1.5G (100 mW/cm²) illumination where Al electrode size was 0.06 cm². The dark current passes through origin when applied voltage is zero, and there is a generated current under illuminated condition.

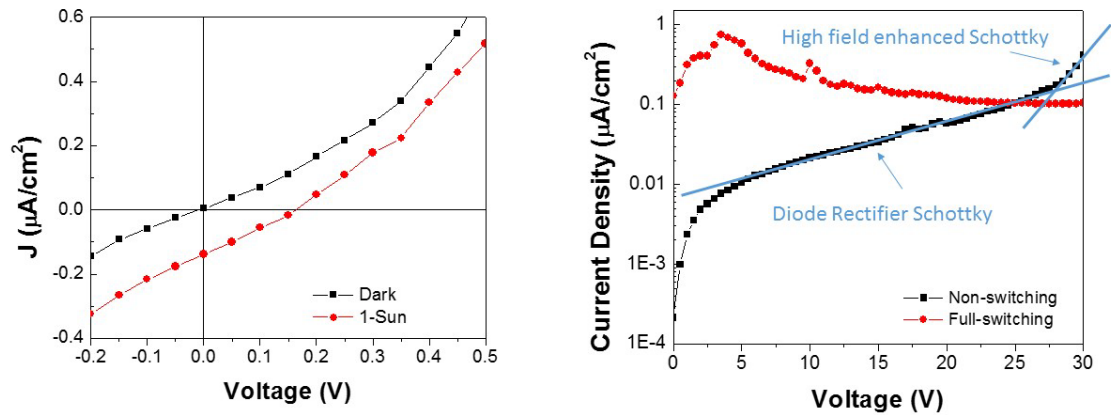


Figure 5. 3 (a) J–V characteristic of the ferroelectric FTO/PZT/Al photovoltaic devices. (b) Comparison of full-switching and non-switching currents, and Diode rectifier type Schottky line and high filed enhanced Schottky line was displayed respectively.

The device processing the structure FTO/PZT/Al exhibited characteristics with a short-circuit current (J_{sc}) of 0.18 $\mu\text{A}/\text{cm}^2$ and an open-circuit voltage (V_{oc}) of 0.16 V. This has a fill factor of 0.25, resulting in power conversion efficiency (PCE) of 0.000007%. The value of generating power is quite small as we could see with other ferroelectric PV

devices. [23, 114] We think this is from the lattice mismatch between FTO and PZT which will be discussed in Chapter 6.

Figure 5. 3. (b) shows the leakage current density versus voltage for a PZT thin film, with initial polarizations by changing the polarity of the applied voltage . The curves of the full-switching current and the non-switching current is very different. We put FTO as an anode, Al as a cathode. Current was measured after applying +1 V (Full-switching) or -1 V (non-switching) to the FTO electrode, by step of 0.02 V increment and 0.1 sec waiting time. When the electric field is applied as a minus to the FTO (Polarization up), then the remnant polarization is not zero and shows high current hump at about 4V, while sweeping up the voltage, and it is marked as “Full-switching”. When the initial electric field plus (polarization down), then the current showed normal I-V curve and marked as “Non-switching”. In the non-switching current in Figure 5. 3. (b) shows not ohmic but a Schottky type current. [43] The leakage current density with Schottky characteristics at low electric field can be explained by;

$$J = J_r \left[1 - \exp\left(-\frac{qV}{mk_B T}\right) \right] \quad (5.1)$$

where J_r is the reverse leakage current, V is the applied bias voltage, q is the electronic charge, K_B is the Boltzmann’s constant, T is the absolute temperature, and m is an ideality factor equal to unity for a perfect diode. [115] In high electric field region above 25 V in this experiment, the formula cannot explain, and the curve diverges. It is similar to the leakage current at high electric field area and called high-field enhanced Schottky.

In FTO/PZT/Al device, low field Schottky behavior was seen under 25 V. Above the 25 V, it showed high field enhanced Schottky curve.

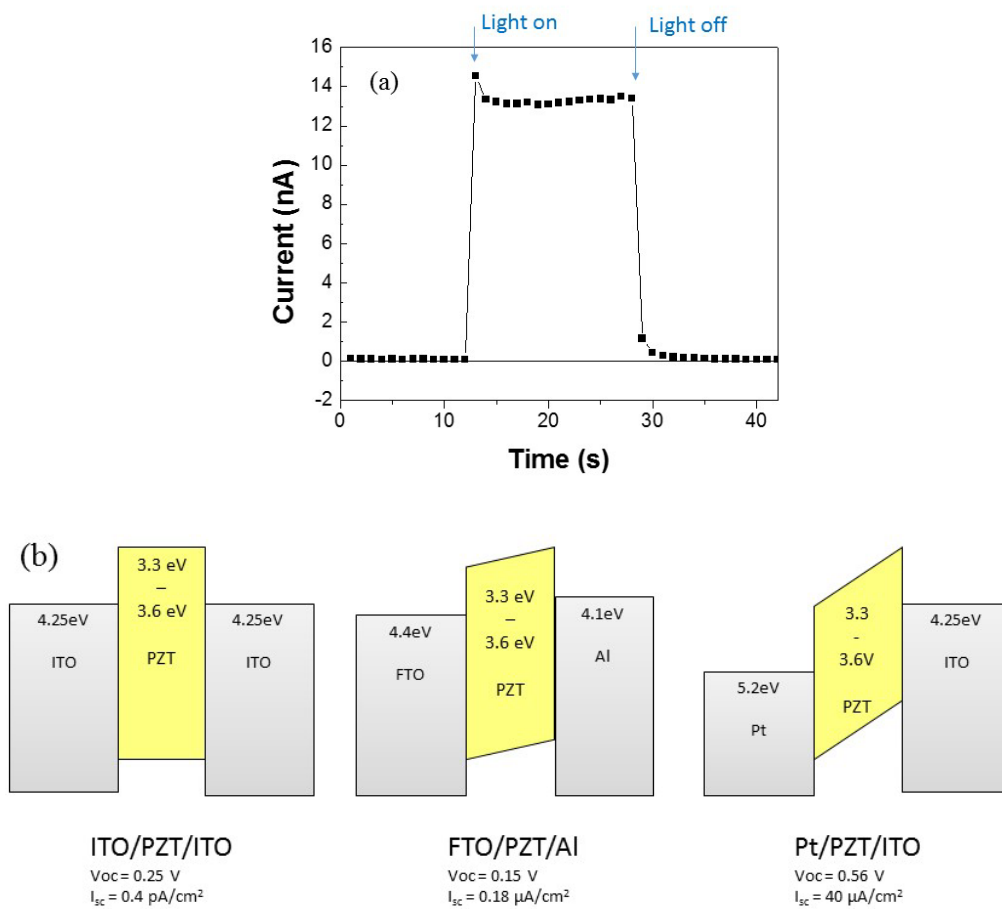


Figure 5. 4 (a) Photocurrent of PZT(53 : 47) thin film deposited on FTO substrate. (b) Schematics of energy band gap comparison among ITO/PZT/ITO, FTO/PZT/Al and Pt/PZT/ITO.

This means that Schottky emission model applies in a temperature domain around 300 K. [43] The existence of the Schottky barrier is important that it can contribute to the

photovoltaic effects, in addition to the bulk photovoltaic effect in ferroelectric PZT thin films. [43, 116]

Figure 5. 4 (a) shows the photoresponse of FTO/PZT/Al structure capacitor device. When the device was exposed to Xe lamp with an AM1.5G (100 mW/cm^2 ; 1-sun) condition, there was a photocurrent flow through the PZT thin film. Current was observed when the light was illuminated PZT device, and the no current was seen when the light is off.

Figure 5. 4 (b) shows the energy band diagram for ITO/PZT/ITO, FTO/PZT/Al and ITO/PZT/Pt structure. As displayed in Figure 5. 4 (b), energy bandgap difference between the two electrodes is the highest at ITO/PZT/Pt, and lowest at ITO/PZT/ITO structure. We can compare the current level of three devices and match with energy band diagram. From the Figure 5. 3. (a), I_{sc} was measured $0.18 \mu\text{A/cm}^2$ where V_{oc} was 0.15V, for FTO/PZT/Al device. For the reference, we compared with ITO/PZT/ITO device. Bin Chen, et al. fabricated ITO/PZT/ITO structure device using the same Zr and Ti morphology ratio, which was $\text{Pb}(\text{Zr}_{0.53},\text{Ti}_{0.47})\text{O}_3$, and the ITO/PZT/ITO structure photocurrent is a pA range, which is very small. The I_{sc} measured 0.4 pA/cm^2 where V_{oc} was 0.25 V. So, FTO/PZT/Al shows the more than 400 times higher photocurrents than ITO/PZT/ITO structure. [20] Cao made ITO/PZT/Pt structure and showed $40 \mu\text{A/cm}^2$ for I_{sc} and 0.56 V for V_{oc} . [19] Considering the Al work function is around 4.1 eV, that of sputtered ITO is 4.25 eV and the FTO work function is 4.4 eV, ITO/PZT/Pt structure shows more than 200 times photocurrent compared with ITO/PZT/Al device.

Schematic energy band gap is shown in Figure 5. 4 (b). Compared to ITO/PZT/ITO, FTO/PZT/Al structure has a slope of a PZT energy band gap because of the FTO and Al

work function difference. Likewise, ITO/PZT/Pt structure has a steeper slope because of the wide difference of energy band gap between Pt and ITO. This schematic can explain why we think that these electrode band gap differences make the photocurrent differences. From this comparison, we could presume that the photocurrent is more related to the ferroelectric metal Schottky junction, rather than PZT bulk photovoltaic effect.

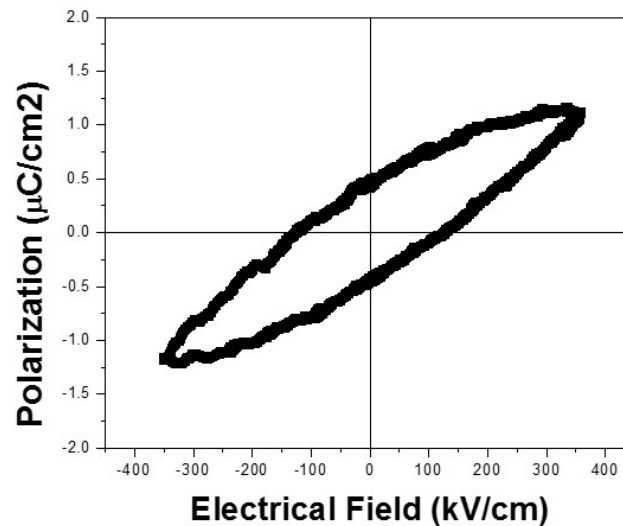


Figure 5. 5 P-E hysteresis loop of FTO/PZT/Al capacitor. . Remnant polarization P_r is $0.5 \mu\text{C}/\text{cm}^2$, when coercive electric field E_c is $125 \text{ kV}/\text{cm}$.

We measured the J-V and photocurrent to observe that ferroelectric FTO/PZT/Al capacitor has good photoresponse and power generation properties. Furthermore, the leakage current shape indicates that the device has a Schottky junction inside. [43] Ferroelectric device normally has low photocurrent and low photo harvesting efficiency. However, if we confirm that PZT, on the TCO substrate, has both photovoltaic(PV) and

ferroelectric properties, then it can be easily used to the next step of PV devices, which is ferroelectric-quantum dots hybrid devices.

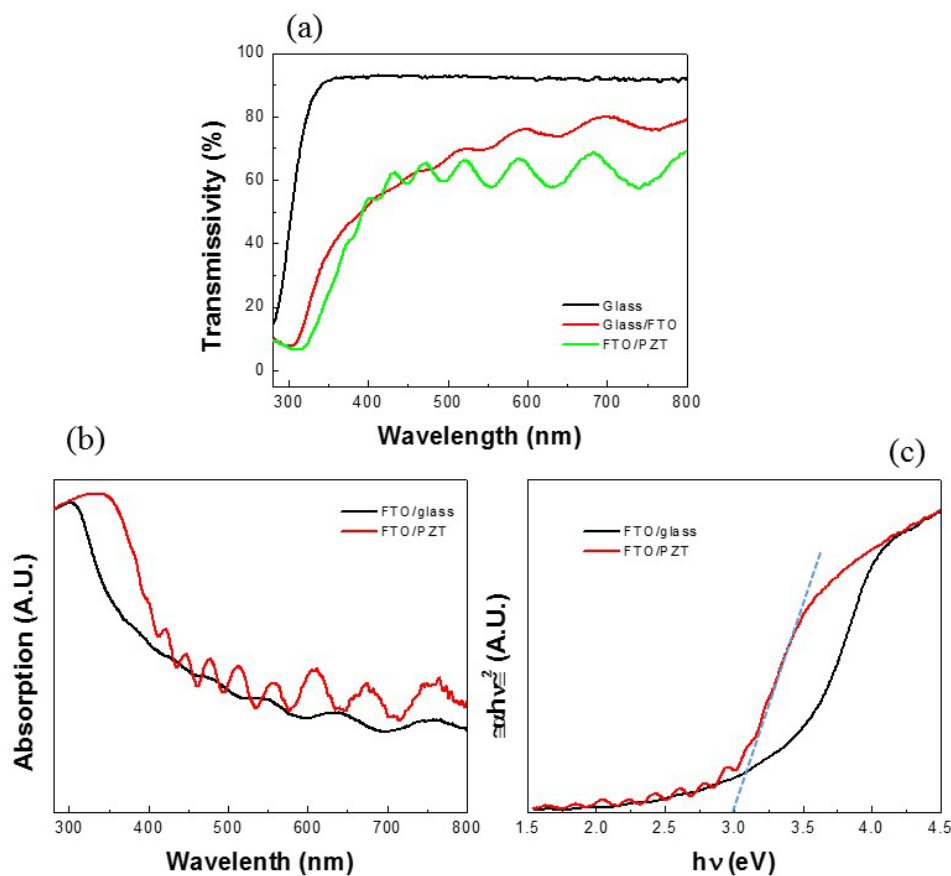


Figure 5. 6 Optical spectra of FTO/glass and FTO/PZT. (a) transmission, (b) absorption, (c) plot of $[\alpha hv]^2$ vs. $h\nu$ in order to find energy bandgap of PZT, which is 3.0 eV.

Figure 5. 5 is the P-E hysteresis of the PZT thin film to FTO substrate and Al electrode at room temperature. The hysteresis shape is not as sharp as PZT thin film coated on the PZT/Pt/Si structure. [117] Still, this device shows coercive electric field (E_c) of 125 kV/cm and remnant polarization (P_r) of $0.5 \mu\text{C}/\text{cm}^2$. This means that the PZT thin film

still has an internal polarization and form a strong internal field inside the film. We think the small polarization effect is from the lattice mismatch between FTO and PZT crystal, compared to that of SiO₂/Pt or SRO substrate. [118, 119]

Next, we studied the optical properties of the PZT thin film. Figure 5. 6 shows the UV–VIS light transmission graph for glass, FTO/glass substrate and PZT films deposited on the FTO-coated glass, respectively. The optical band gap is calculated to be 3.0 eV for the PZT/FTO/glass chip, which is the compatible with the value we suggested above. For a direct band gap semiconductor, the optical energy band gap E_g can be estimated from absorption $\alpha(h\nu)$ using the following relation; [120]

$$\alpha h\nu = A (h\nu - E_g)^2 \quad (5.2)$$

Where A is proportionality constant and $h\nu$ is the photon energy. The absorption coefficient $\alpha(h\nu)$ can be calculated by the relation $\ln(1/T)/d$, where T is the transmittance and d is the thickness of the film. The optical band gap of the deposited films can be estimated by plotting $(\alpha h\nu)^2$ as a function of $h\nu$, and extrapolating the linear region of $(\alpha h\nu)^2$ to the energy $h\nu$, where $(\alpha h\nu)^2$ corresponds to zero (David and Mott 1970, Tauc 1974, Tan et al 2005). Measuring the absorption and transmission gave us the proper energy band gap of the PZT thin film, which means that the UV light will be observed in this device and excite the carriers.

5.5 Conclusion

PZT synthesized successfully by a sol-gel method, and the resulting PZT thin film shows crystalized perovskite structures. ITO/PZT/Al MFM device was fabricated and ferroelectric internal field and photosensitive properties were observed. We also confirm Schottky barrier in the device and energy band diagram was explained comparing with other research group results. Optical Transmission and Absorption was measured and the energy bandgap was calculated. We tried to fabricate well crystallized PZT thin film for the next step, which is synthesizing the PZT nanoparticles, and novel concept of the device using PZT materials. We will discuss the PZT nanoparticle device in Chapter 5 and a new concept of the photosensitive device in Chapter 6, based on the successful fabrication of Al/PZT/FTO in this chapter.

Chapter 6. Ferroelectric Devices using Lead Zirconate Titanate (PZT) Nanoparticles

6.1 Overview

We successfully demonstrated the synthesis of lead zirconate titanate nanoparticles (PZT NPs) and the ferroelectric device using synthesized PZT NPs. The crystalline structure and the size of the nanocrystals were studied using X-ray diffraction and transmission electron microscopy (TEM), respectively. We observed < 100 nm of PZT nanoparticles and this result matched dynamic light scattering measurement (DLS). The solution based low-temperature process was used to fabricate PZT NP based devices on ITO substrate. The fabricated ferroelectric devices were characterized by using various optical and electrical measurements and we verified ferroelectric properties including ferroelectric hysteresis and ferroelectric photovoltaic effect. Our approach enables low-temperature solution-based processes that could be used for various applications. To the best of our knowledge, this low-temperature solution processed ferroelectric device using PZT NPs is the first successful demonstration.

6.2 Background

Ferroelectric thin films and nanometer scale materials show extreme promise for numerous applications including nonvolatile memories, [121, 122] energy harvesters, [123, 124] field emission transistors (FET), [125] sensors and actuators. [44] For

decades, ferroelectric thin films on various substrates were researched extensively. Recently, the bulk photovoltaic effect (BPVE) of the ferroelectric materials also has attracted a lot of interest, [18, 118] because it enables a solar cell with an extremely large photovoltage, which is ‘above the materials bandgap’. [111, 126, 127]

Among ferroelectric materials, lead zirconate titanate ($\text{PbZr}_x\text{Ti}_{1-x}\text{O}_3$, PZT) thin film and NPs are a well-known ferroelectric material that has attracted a wide interest due to its excellent ferroelectric, piezoelectric and photovoltaic properties. [17, 128] PZT thin film and nanostructures can be fabricated using various methods such as MOCVD, sputtering, hydrothermal process and the sol-gel method. [94, 129, 130] Among those, the sol-gel reaction method has been widely used in preparing ferroelectric PZT materials because of its easy and inexpensive synthesizing process. [101, 131] However, PZT synthesized by sol-gel method need high crystallization temperatures. Usually, the thin film is treated above 600 °C for better ferroelectric properties. [132] This high temperature hinders the hybrid structure with other material which has cracks or inter-diffusion problems. [133, 134] This high-temperature process also prevents the use of an indium tin oxide (ITO) substrate or flexible polymeric substrates. To obtain a high quality ferroelectric properties, a good lattice match with the substrate is important. Therefore, expensive substrates, including SrRuO_3 , MgO or SrTiO_3 are widely used. [135] One of the possible solutions to address this issue could be nanostructured PZT materials. Due to its small dimension, the PZT nanostructures can be prepared as a colloidal solution while it keeps a good crystallinity and ferroelectric properties.

Recently, the discovery of perovskite ferroelectric nanomaterials opened up a great possibility of application for ferroelectric devices. There have been various nanostructures such as nanoparticles, nanorods, and nano-patterned structures using PZT, BaTiO₃, and SrTiO₃. [136-138] Those ferroelectric nanomaterials exhibit very different characteristics in its domain dynamics, coercive field and spontaneous polarization response. [30, 139-141] Since PZT ferroelectric materials require quite a high temperature in the sol-gel synthesis process, colloidal PZT NPs enable a low temperature solution based device fabrication. There have been several reports regarding PZT nanoparticle synthesis and sub 10 nm size of synthesized free-standing PZT particles are reported. [142] Recently, PZT NP was studied for its size, structure and domains, using XRD, FTIR, TEM and PFM. [107, 131, 143] However, there are more needs to understand properties of PZT NPs for various applications. In addition, if we synthesize the nanoparticles without losing ferroelectricity or photovoltaic properties, we can expand the ferroelectric device to various substrates, structures, and nano-scale applications.

In this study, we synthesized nearly free-standing nanocrystalline PZT particles in the size regime of about 30 nm – 100 nm. We introduced a modified sol-gel approach removing a gelation process and introducing an inert gas treatment in order to synthesize nanoscale PZT material. We have investigated the underlying chemistry in the hydrolysis-condensation of conventional PZT sol-gel method and characterized the synthesized PZT nanoparticles (PZT NPs) in order to have a further understanding on the structural evolution from sol to gel to crystalline nanoparticles. Synthesized PZT nanoparticles were fabricated as a photo sensing device with ITO substrates and Al

electrode. The fabricated devices show a clear difference in the electrical properties between PZT thin film and PZT nanoparticles. We also fabricated photo sensing devices by PZT NP sizes. The devices closely packed by smaller NPs shows well crystallized photo generating properties independent of the substrate structure. We discussed that size-dependent-ferroelectric-properties were originated from the nanoparticle surface effect.

6.3 Experiment

6.3.1 PZT Bulk and Nanoparticle Synthesis

In our synthesis process, we start with the synthesis of PZT sol-solution by a sol-gel method in order to fabricate a bulk PZT thin film and PZT NPs. The precursor materials were lead acetate trihydrate, zirconium propoxide, and titanium isopropoxide. And the solution of these precursors is 2-methoxyethanol. The synthesis starts with dissolving 0.4 M of lead acetate trihydrate ($\text{Pb}(\text{CH}_3\text{COO})_2 \cdot 3\text{H}_2\text{O}$; 99.5%, SigmaAldrich, USA) in 2-methoxyethanol at 80 °C for 2 hours. When we weighed 0.4 M of lead acetate, an extra 10% was added to recover the evaporation loss. [97, 108] In order to dissolve the lead acetate trihydrate, 2-methoxyethanol was injected by a syringe into the vacuumed flask while the magnetic stirring was used for 30 min to get a uniform solution. [144] After dissolving lead acetate in the solution, 0.4 M titanium isopropoxide ($\text{Ti}[\text{OCH}(\text{CH}_3)_2]_4$; Aldrich, USA) was added to the lead-dissolved solution. After a vigorous stirring process, the mixed precursor solution became clear and transparent. Using the same method, 0.4 M of zirconium propoxide ($\text{Zr}(\text{OCH}_2\text{CH}_2\text{CH}_3)_4$, 70 wt. %; Aldrich, USA) were mixed into

the lead titanate precursor solution. The solution was stirred at 80 °C until it turned into a clear and transparent solution again. We choose the ratio of Zr : Ti = 53 : 47, which is near the morphotropic phase boundary (MPB), for the best ferroelectric properties in this work. [37-39]

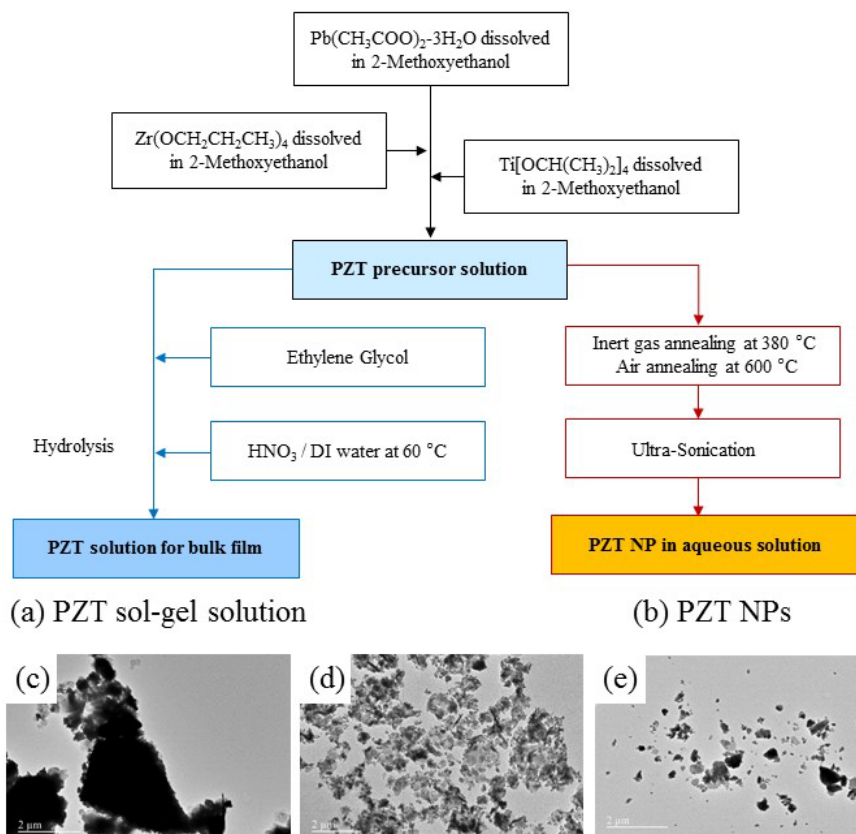


Figure 6. 1 Flow chart of sol-gel methods for bulk and nanoparticle PZT synthesis, and resulting Transmission Electron Microscopy (TEM) images. (a) A Method for PZT sol-gel solution for bulk material-Sample 1, (b) new synthesis approach for PZT NPs- Sample 2 and 3 (c) TEM images of PZT particles (Sample 1) synthesized by sol-gel and followed by the grinding method. (d) TEM picture of large size PZT NPs (Sample 2), and (e) small size PZT NPs (Sample 3).

After the preparation of the PZT precursor solution, three different synthesis methods were developed to prepare different PZT materials. One of those is the PZT sol-gel solution for the bulk PZT film (S1), and the others are the PZT NPs with different sizes (S2 for large PZT NPs, S3 for small PZT NPs). Synthesis of all three samples starts with the same precursor materials, but the processes are different as shown in Figure 6. 1 (a) and (b). A 2-methoxyethanol based sol-gel solution was spin cast after hydrolysis in order to form a bulk PZT films (S1), as described in the literature. [108] And a new sol based approach was used to create the large and small size of PZT NPs (S2 and 3).

Figure 6. 1 (a) shows the process of the sol-gel method for PZT bulk material (S1). In order to synthesize PZT NPs (S2 and S3), we adopted a new approach to the PZT precursor solution. As shown in Figure 6. 1 (b), we skipped the hydrolysis process that requires deionized (DI) water and nitric acid (HNO_3). Hydrolysis process benefits the spin casting process to create a thin film PZT, because the higher viscosity of the hydrolyzed solution enables better control of the film thickness. However, hydrolysis also accelerates the gelation in the solution, resulting in the micron size agglomeration of metal-organic compounds in the solution. [16, 101] Therefore, we skipped hydrolysis to maintain smaller PZT particle sizes. Instead of the gelation process, the prepared PZT precursor solution was transferred into inert condition, and heat treated. The PZT sol precursor was treated at 380 °C in the nitrogen-filled glove box for 30 min. This process changed the liquid precursor to black colored powder. It is assumed that this black color of the resulting PZT material is originated from the carbon molecules that was converted from the organic compounds. Therefore, the black colored powder consists of carbon and PZT compounds in nano-scale. Then we carried out the secondary annealing process at 600 °C under

oxygen-rich ambient for 30 min. After this annealing process, the resulting PZT material becomes a bright yellow colored powder. We assume that the carbons surrounding PZT nanostructure disappeared, and the PZT nanostructure became a perovskite structure because of the high annealing temperature [131]. Finally, an ultrasonication process was used after the PZT powder was dissolved in DI water. The ultrasonic energy can break the weak-bonding of the PZT nanostructures and effectively separate the nanoparticles from the agglomerated PZT nano powders. We also observed the sonication time is related to the nanoparticle size. In this work, we used the 2-hour sonication time to produce the large size PZT NPs (S2), and 48-hour sonication time for small size PZT NPs (S3).

Figure 6. 1 (c) shows that the particles become the size of a micrometer scale after oxygen-rich annealing, without the inert gas heat treatment. After the sintering process, we used mechanical grinding with a molar and a pestle to make PZT powders and the resulting powders are micrometer scale. However, we successfully synthesized PZT nanoparticles (under 100 nm) using our new approach as shown in Figure 6. 1 (d) and (e). Larger sizes of PZT NPs in Figure 6. 1 (d) are from the two hour ultra sonicated sample, and smaller size of PZT NPs in Figure 6. 1 (e) are produced by 48 hour ultrasonication process.

6.3.2 Device Fabrication and Measurement

As discussed earlier, we fabricated devices using a PZT sol-gel based bulk film (S1) and the two different types of colloidal PZT NPs, which are large size PZT NPs (S2) and small size PZT NPs (S3), in this study. In order to measure the properties of ferroelectrics and photoelectric, we fabricated Metal-Ferroelectrics-Metal (MFM) structure capacitive

devices on an ITO substrate. For the bulk PZT films (S1), the sol-gel solution was spin-casted onto a patterned ITO glass with a sheet resistance of 15 ohms-cm², (Thin film devices Inc.) and annealed at 600 °C for 30 min for the crystallization. The aluminum electrode (100nm thick) was thermally evaporated, resulting in ITO/bulk-PZT-film/Al device structure. For the PZT NPs (S2 and S3) thick film, PZT NPs in an aqueous solution was drop-casted on the patterned ITO glass while the glass substrate was heated at 80 °C. We used 1.5 ml of PZT NP solutions (40 mg/ml in DI water) to cover the 1.6 cm² size substrate for one time drop casting. Multiple drops used to ensure well-packed thin film deposition. Then, the same thermal evaporation process with a shadow mask created aluminum electrodes as shown in Figure 6. 2 (a). And the active area of this fabricated MFM device was 0.06 cm².

Figure 6. 2. (b) and (c) shows the cross-sectional scanning electron microscope (SEM) images of a large size PZT NPs (S2) and a small size PZT NPs (S3) MFM device, respectively. The thickness of both PZT NPs is both around 10 μm. As seen in the SEM images, we observed smoother surface profile. It is hard to tell the size of the nanopzrticles for S2 and S3 samples, since they are all aggregated during the fabrication process. However, the rough texture and uneven surface profile of the device using S2 indicates more porous film structure due to the wide size variation of PTZ particles.

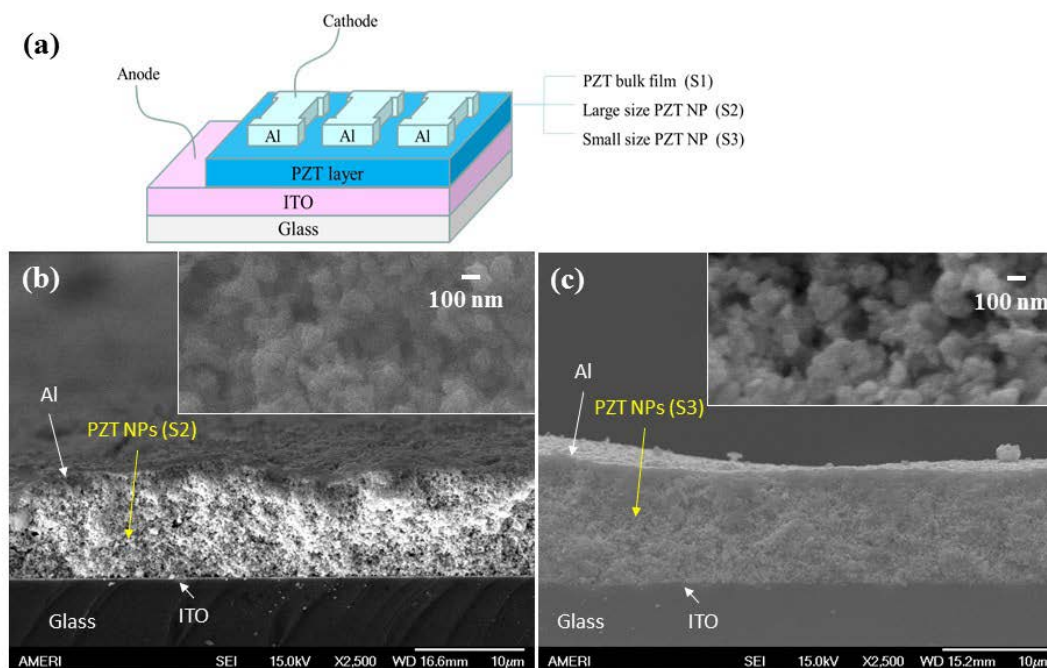


Figure 6. 2 (a) Schematic diagram of the fabricated PZT device, with the active device area of 0.06 cm^2 . Scanning Electron Microscope pictures of the cross section of ITO/PZT-NPs/Al structure devices with (b) large size PZT NPs (S2) and (c) small size PZT NPs (S3). The insets show the magnified cross section morphology of the fabricated PZT NP based devices.

To investigate the crystalline structures of the synthesized samples, an X-ray diffraction (XRD) study was carried out using a Siemens 500D X-ray Diffractometer with high-intensity CuK α radiation and 2θ step interval of 0.02. The measured X-ray peak was compared to JCPDS card and confirm the material structure. Transmission electron microscopy (TEM) images were taken with a Phillips CM-200 using an acceleration voltage of 200KV. Field emission scanning electron microscopy (FESEM) images were taken with a JEOL 6330F scanning electron microscope. Ferroelectric hysteresis was measured using Sawyer-Tower circuit, an oscilloscope (Tektronix TDS3014B) and a

function generator (Tektronix CFG253) that supplies a 130 Hz 20 V_{p-p} voltage signal. Reference capacitor was 10 μF, and a 130 Hz triangular waveform was used for the P-E hysteresis measurement. The I-V and photocurrent measurement was carried out using a source meter (Keithley 2400) and a LabView based custom data acquisition program. The photoresponse was measured under a one sun power (100mW/cm²) illumination using a 150W Xe lamp (Oriel) with AM1.5G filter.

6.4 Results and Discussion

6.4.1 Material Properties

Ferroelectric PZT materials can have two phases of the perovskite structure, which are a tetragonal and rhombohedral unit cell structures near the MPB. [35] Figure 6. 3 (a) shows the comparison between X-ray diffraction peaks of all the synthesized PZT samples. The two XRD patterns in Figure 6. 3 (a) are taken from PZT NPs and a bulk PZT film coated on ITO substrate. After the annealing process, peaks from both of PZT NPs S2 and S3 shows (101) and (201) peaks (JCPDS card No. 70-4260). [36] These XRD results confirm that the synthesized PZT NPs have the same rhombohedral crystallization as the PZT powder with micron scale, even though the diameter of particle sizes are below 100 nm. However, bulk PZT thin film (140nm thick) on the ITO substrates shows the main peak of (100) and (110) which can be interpreted that the perovskite on the bulk film is the mixture of tetragonal and rhombohedral.

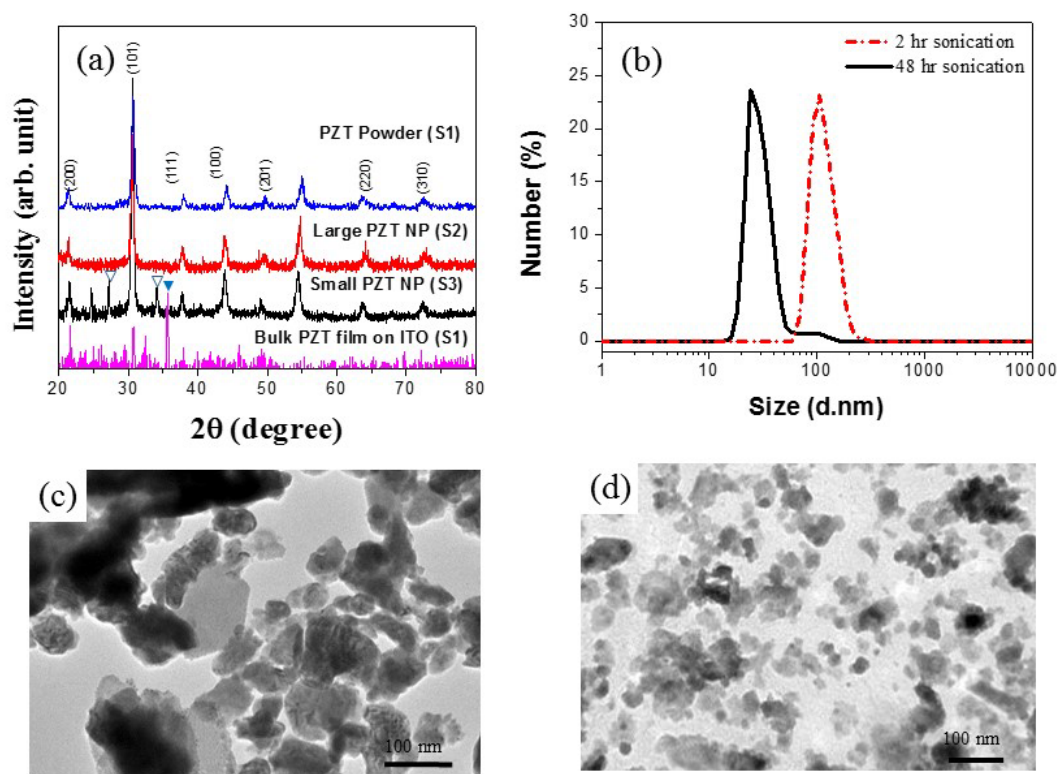


Figure 6. 3 (a) XRD diffraction pattern of bulk PZT powder synthesized by sol-gel method and PZT NPs synthesized by our new approach. “▽” and “▼” marks represent FTO and ITO peaks respectively. bulk PZT on ITO sample was only 140nm thick. (b) Measured DLS data shows the size distributions of two different samples (S2 and S3) and the peak values are 105 nm and 24 nm for S2 and S3, respectively. TEM images of PZT NPs are from (c) S2 with short ultrasonication time (2 hours), and (d) S3 with long ultrasonication time (48 hours).

TEM images of the PZT NPs under different synthesis conditions (S2 and S3) are shown in Figure 6. 3 (c) and (d). Figure 6. 3 (c) shows the PZT NPs after the sonication time duration of 2 hours. We observed 100 nm or larger nanoparticles with this 2 hour ultra-sonication treatment. As shown in Figure 6. 3 (d), longer ultra-sonication treatment

time enabled much smaller nanoparticle sizes (near 30nm). We assume that the vibrational energy provided by ultra-sonication can separate the agglomerated nanoparticles. In addition, we carried out Dynamic Light Scattering (DLS) measurement to confirm the distribution of the nanoparticle sizes. As shown in Figure 6. 3 (b), the measured data are well matched with the TEM images for both S2 and S3 samples. Peak values from the DLS data are 105 nm for S2 and 24 nm for S3. All these characterization results confirm that we have successfully synthesized PZT materials in a form of bulk or nanoparticles. Moreover, the simple ultra-sonication treatment enables PZT nanoparticles' size control depending on its treatment time.

We tried various PZT nanoparticles by Zr and Ti ratios. Figure 6. 4 shows TEM images and selected area electron diffraction (SAED) patterns of synthesized PZT NPs from different Zr and Ti ratio conditions. We confirmed that the synthesized PZT NPs with the ratio of Zr : Ti = 20 : 80, 35 : 64, 53 : 47, 65 : 35 and 80 : 20 show good crystal structures by SAED pattern. However, in Figure 6. 4 (d) and (e), 65 : 35 and 80 : 20 ratio of the PZT NPs shows the less crystallized nanoparticles and shows less crystallized SAED pattern compared to the others. SAED patterns for that two ratios is polycrystalline proved by the circular pattern from SAED, rather than the point pattern from the well crystalized SAED. This shows that the higher ratio of the Ti (less ratio of Zr) tend to well crystalized, when we synthesize PZT NPs. We chose the ratio of Zr : Ti = 53 : 47, which is near the morphotropic phase boundary (MPB), for the best ferroelectric properties for all devices in this paper. Figure S 1 (b) shows the TEM image from PZT NPs (S2, 53 : 47). The image also shows the aligned domain structure from the PZT NPs.

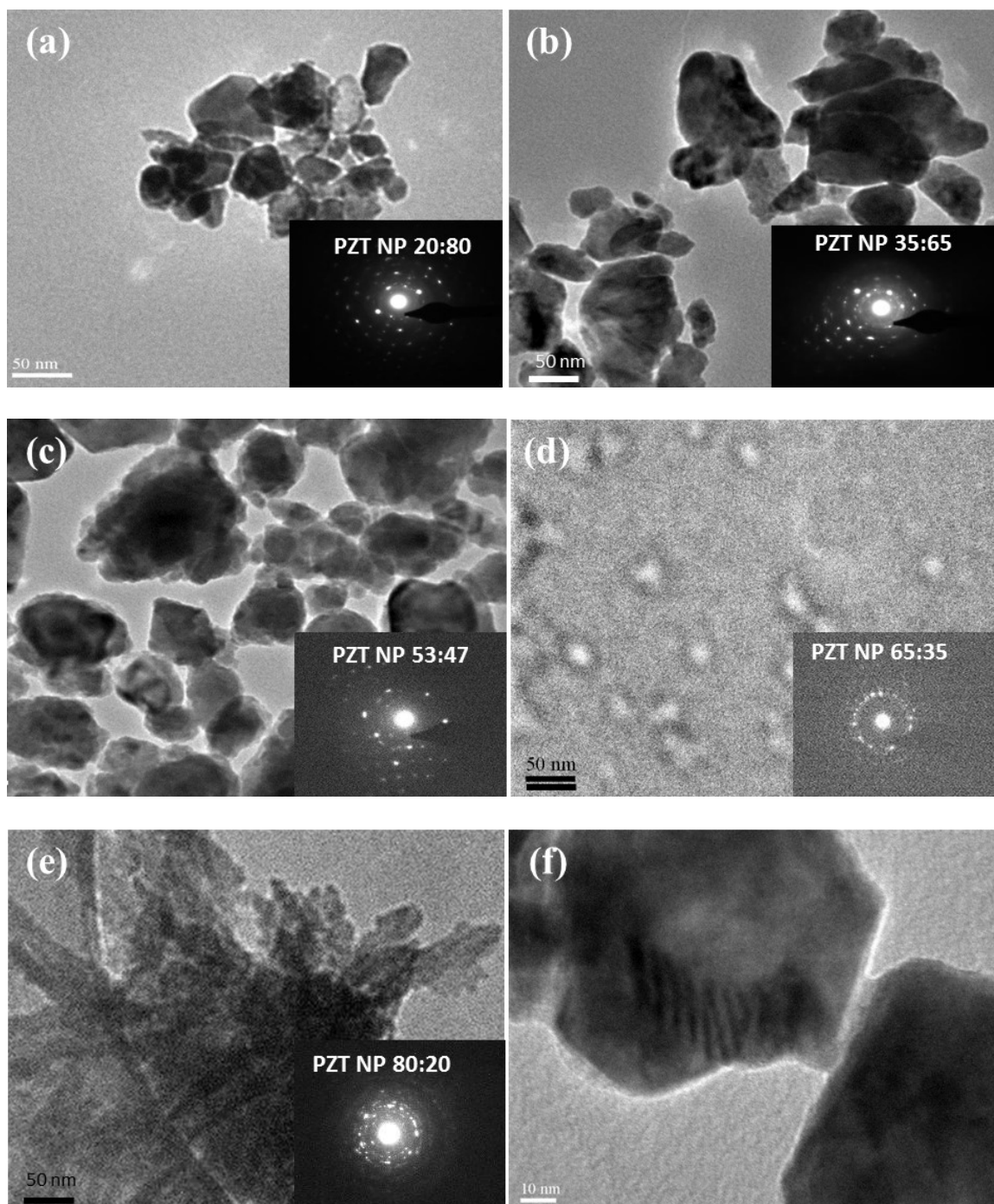


Figure 6. 4 TEM images and SAED patterns of PZT NPs by different Zr and Ti ratio. (a) Zr : Ti = 20 : 80, (b) Zr : Ti = 35 : 65 (c) Zr : Ti = 53 : 47, (d) Zr : Ti = 65 : 35, and (e) Zr : Ti = 80 : 20. All samples are after the 2 hour sonication. (f) Domain walls structure in PZT NPs (53 : 47) with the high resolution TEM images.

In Figure 6. 4. (f), domain structure was observed from the PZT NPs (53 : 47) after 2 hours of sonication. Through this TEM image, we can confirm that the PZT NPs are consist of domains which is the size smaller than the PZT NPs. This means that the domain size is also confined by the nanoparticle size. Bulk domain area will be separated and form a smaller domain size and the domain size is less than the PZT NPs size which is less than 100 nm in this thesis. When we make a PZT thin film device on the substrates, the domain and grain size is from 1 – 10 μm . [145] With PZT NPs, we can expect much less size (less than 100 nm in this thesis) of the domains and photo induced could face more frequent domain walls, then conventional PZT thin films.

6.4.2 Ferroelectric Properties of PZT Thin Film and PZT NPs

Ferroelectric materials have spontaneous polarization when there is no external electric field. This polarization direction changes when the external electric field is higher than a coercive field (E_c). Electric fields higher than E_c will align the domains in one direction. In this case, the aligned domain will remain even after the external electric field is removed. If we apply the external field in the opposite direction again, the alignment of the domain will flip over and align with the opposite direction. This is called the domain inversion process. [146]

We used the same PZT based MFM devices to confirm ferroelectricity as described in Figure 6. 2 (a). We studied ferroelectric P-E hysteresis by bulk PZT film and PZT NPs (S2 and S3). We observed the small size PZT NPs showed a saturated hysteresis. A bulk PZT film device fabricated on the ITO shows $0.6 \mu\text{C}/\text{cm}^2$, where coercive field, E_c is 134 kV/cm as shown in Figure 6. 5 (a).

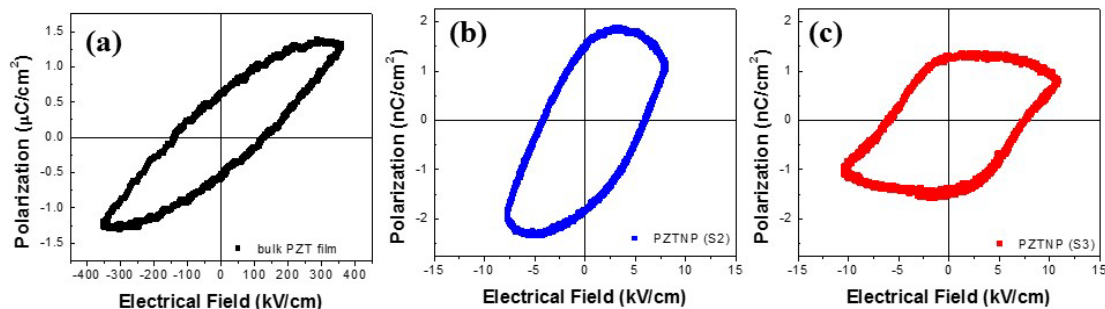


Figure 6. 5 Hysteresis of (a) ITO/bulk-PZT-film/Al, (b) ITO/PZT-NPs(S2)/Al and (b) ITO/PZT-NPs(S3)/Al structure.

The overall shape of ferroelectric hysteresis from the bulk PZT film (S1) device shows weak saturation in its hysteresis response. We assume that it is due to a very thin film thickness (~ 140 nm) and poor crystallization of PZT thin film due to the lattice mismatch between PZT ($a = 0.404$ nm) and ITO film ($a = 1.022$ nm). [147] Therefore, a PZT thin film on an amorphous ITO/Glass substrate is difficult to show the saturated hysteresis. [117] Figure 6. 5 (c) shows the hysteresis of ITO/PZT-NPs(S3)/Al device. The PZT NP device shows a saturated ferroelectric hysteresis compared to a bulk PZT film on ITO, because the PZT NPs are crystallized during the synthesis process. However, we observed relatively small polarization value (~ 1.5 nC/cm²) and coercive field value ($E_c \sim 5.5$ kV/cm). In Figure 6. 5. (b) similar polarization and E_c values are shown with a large size PZT NPs (S2), which is ~ 1.5 nC/cm² and coercive field of $E_c \sim 5.5$ kV/cm. However, the shape shows less saturated and distorted. We cautiously explain this distorted data is less compact PZT NPs film device from S2 samples, and comparably porous structure makes electrically imperfect.

Both of the PZT NPs shows small values of polarization. We assume that this small polarization comes from the aqua-solution based fabrication process, which is difficult to control the direction of ferroelectric domain and polarization. The domain orientation, such as c-domain or a-domain, can be affected mainly by lattice constants, and thermal expansion rate between PZT and substrates.

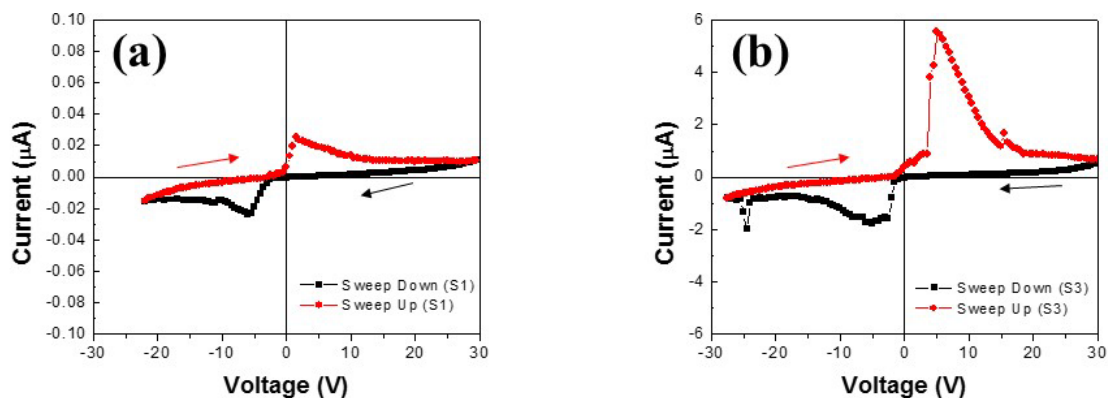


Figure 6. 6 Displacement current of (a) bulk PZT film on ITO substrate, and (b) PZT NPs on ITO substrate. Displacement current was measured using 5 kHz triangular waveform and sweeping up and down from -30 V to +30 V.

However, the synthesized PZT NPs is a free standing form and they cannot be grown on the substrate, but randomly deposited on an ITO substrate. [145, 148] Even though the individual nanoparticles are well crystallized, the PZT film using very small and random domain structures exhibits relatively small hysteresis response. To confirm this assumption, we need further investigation with PFM study to observe domains structures in the PZT NP film. In addition, we did not observe the better hysteresis from large PZT NPs (S2) and

more details including displacement current measurement are discussed in Figure 6. 6. However, those results show that the synthesized PZT NPs has the ferroelectric properties. And this opens a potential to use PZT NPs for nanoscale ferroelectric switching applications.

Figure 6. 6 shows displacement currents of bulk PZT and PZT NP devices, using 5 kHz triangular waveform (amplitude 5 V) and sweeping up and down from -30 V to +30 V. in Figure 5 we discussed the hysteresis for bulk PZT film on ITO and PZT NPs sample using S3. Figure 6. 6 (a) and (b) show the corresponding displacement currents of bulk PZT film and PZT NPs (S3), respectively. Both of the structure shows there is a dipole reversal process at the peak voltages. It should be noted that the crystal texture of the PZT films grown on ITO layers is relatively poor, resulting in relatively not saturated hysteresis shape, and differences in peak position and heights from the displacement current measurement. However, PZT NPs are already well crystallized before fabricating a device, and shows saturated hysteresis (Figure 5 (c)). The displacement current of PZT NPs is also shown higher dipole reversal process. (Figure 6. 6. (b))

6.4.3 Optoelectronic Properties of the Devices

One of the fascinating properties of the ferroelectric PZT material is its bulk photovoltaic effect. The absorbed photons create electric dipoles in the ferroelectric domains, and it produces an internal electric field across the device, resulting in open circuit voltage. We measured the photo response current under a dark and 1 sun (AM1.5G spectrum) power illumination. As shown in Figure 6. 7, PZT NP based devices by NP sizes show photo response, but the generated current levels were different. The measured

photocurrent was around 2 nA and 20 nA for the S2 device and S3 device, respectively.

(Figure 6. 7)

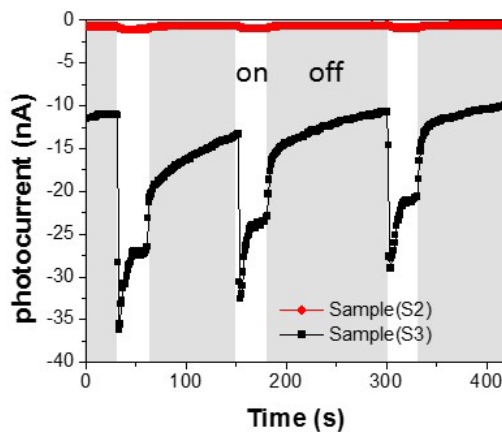


Figure 6. 7 Measured photoresponse from PZT NPs devices (S2 and 3) under gated light illumination using a solar simulator (1 sun power, AM 1.5G). The gray and white zones represent dark (off) and 1 sun illuminated (on) conditions, respectively.

In a ferroelectric polar system such as the PZT, the photon induced exciton is expected to be localized and tightly bound. [10, 14] Therefore, such an exciton in the bulk of the PZT is expected to recombine quickly, resulting in a small net photo effect. So a larger photocurrent could be originated from the particles with high surface to volume ratio. However, as we observed in the SEM image shown in Figure 6. 2, the PZT film quality between S2 and S3 samples are very different. S2 sample has larger size variation and more irregular particle shapes, it causes not a dense PZT film structure and shows poor photoelectric properties.

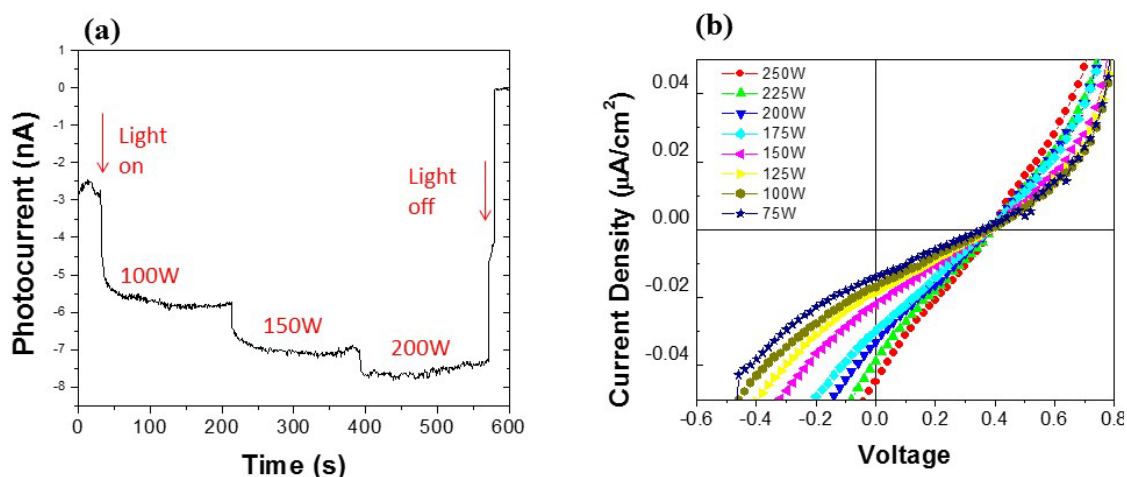


Figure 6. 8 The dependence of the photo-current and photo-voltage on the light intensity.

(a) Time based photocurrent while the light intensity increased from 100 W to 150 W to 200 W. (b) Photovoltage dependence by light intensity from 250 W to 75 W with a step of -25 W.

Photocurrent and photovoltage is known from the polarization-induced internal electric field instead of a p-n or Schottky junctions, [149] and the internal field enhanced the carrier separation, which is generated while the light is emitted in the ferroelectric material. We think the high intensity of the light can generate more carrier in the ferroelectric material and will show the higher value of the photo-current.

We further studied the photocurrent of PZT NPs by light intensity. Figure 6. 8 shows the time based photocurrent change when the light intensity is increased. The photocurrent shows higher values when the light intensity is increased. It is reported that the V_{oc} is proportional to the light intensity in a ferroelectric bulk material by Koch et al. [150] Figure 6. 8 (b) shows the V_{oc} under the different light source intensity. In contrast to the bulk ferroelectric ceramics, we observed that the V_{oc} level is not significantly changing while

we increase the light intensity. It should be noted that, the ferroelectric structure in our PZT thin film is not exactly same as the single crystalline ferroelectric materials that were studied earlier. In this study, we used a $\sim 10 \mu\text{m}$ thick PZT NP layer between two electrodes. We presume that the a single crystalline ferroelectric materials with bigger domain size show the V_{oc} change as a bulk photovoltaic effect. However our system (30 nm- 100 nm NPs) didn't show the same result. We cautiously assume this is from the reason that randomly aligned domains (dipoles) make a small internal field in macro scale device and the dipole strength in the small PZT NPs could be saturated under lower power illumination.

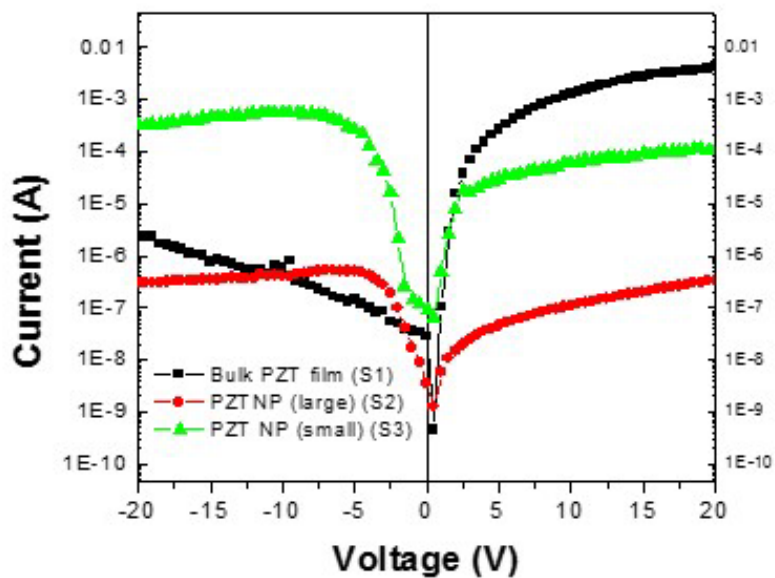


Figure 6. 9 Leakage current of bulk PZT film (S1), large size PZT NPs (S2) and small size PZT NPs (S3) MFM devices respectively.

One more interesting study from PZT NP is leakage current. Figure 6. 9 shows the leakage current of the bulk PZT film (S1), the large size PZT NPs (S2) and small size PZT NPs (S3). Compared to the S2 which is larger PZT NPs, S3 shows higher leakage level.

We presume that higher leakage current of S3 is from less porous and closely packed structure of the nanoparticle film. The leakage current is not symmetry for all devices and this can be explained by Schottky emission or Fowler-Nordheim tunneling (FN). [151]

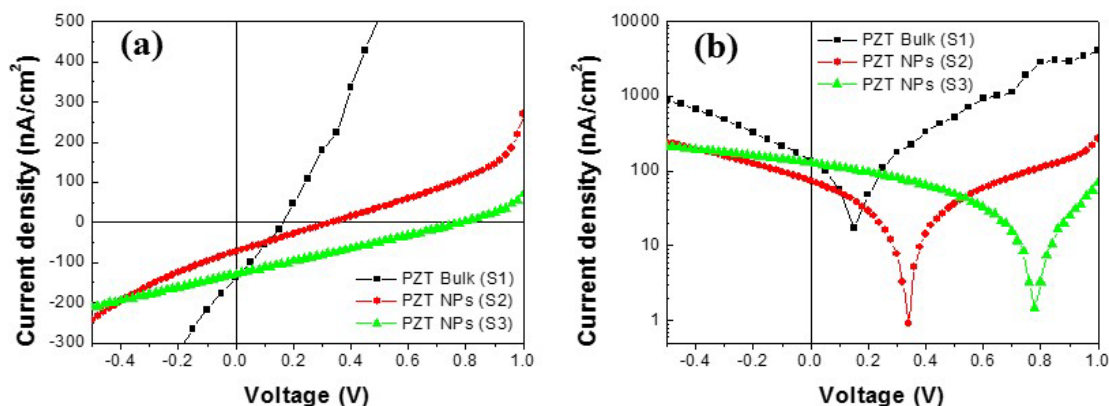


Figure 6. 10 J-V characteristics of fabricated devices under light illumination (1 sun power AM1.5G solar spectrum). (a) J-V plots of the devices using sol-gel derived PZT bulk film (S1), larger size PZT NP (S2) and smaller size PZT NP (S3). (b) log-scale plots of J-V measurements to compare the open circuit voltages from the devices using PZT bulk (S1), larger size PZT NPs (S2) and smaller size PZT NP device (S3).

From both PZT NP based devices, we observed decreased current while increasing the bias voltage on the negative side of Figure 6. 9. We need further investigation for better understanding of this unusual results. However, we observed that the ferroelectric

nanoparticle should explain with subtle care, because it will not follow Schottky or Fowler-Nordheim graph curvature.

We further investigated the ferroelectric photovoltaic effect of synthesized PZT materials using J-V measurement under 1 sun illumination (100 mW/cm^2). Figure 6. 10. (a) and (b) shows the current density–voltage (J–V) characteristics of the ferroelectric bulk film (S1) and PZT NP (S2, 3) devices. The measured short circuit current and open circuit voltage of bulk PZT film on ITO substrate (a J_{sc} of 138 nA/cm^2 and a V_{oc} of 0.15 V) are comparable to the reported properties by other research groups. [117] The photovoltaic device using sample 2 (S2) shows 74 nA/cm^2 of short circuit current and 0.34 V of open circuit voltage. The short circuit current density of the device using sample 3 (S3) was 129 nA/cm^2 and it is comparable to the device using PZT bulk material (S1). However, we observed 5 times larger open circuit voltage (0.78 V) than the device using bulk PZT film (S1) on the ITO substrates. We explain that the higher V_{oc} effect is from the lattice-free crystallization effect from the PZT NPs in the film. As we observed in Figure 5, The PZT NP shows a better saturated hysteresis characteristics due to the pre-crystallized nanostructures before the device fabrication process. This is one of the reasons that we could achieve better photovoltaic properties using PZT NPs. The difference between S2 and S3 samples could be from the number of domains between two electrodes as well as their sizes from the nanostructures. However, it should be noted that the film quality and roughness could affect the photovoltaic properties of devices using S2 and S3 materials. This result shows a promising property of the PZT NPs that can potentially increase open circuit voltage when they are used with a solution based photovoltaic devices such as organic or colloidal quantum dot based photovoltaic cells, with wide choices of substrates.

6.5 Conclusion

We have demonstrated a successful synthesis of PZT nanoparticles using a modified sol-gel method, and ferroelectric properties of the devices using the synthesized PZT nanoparticles. The two-step annealing process under inert and oxygen rich ambient enabled to create PZT nanoparticles. We also successfully controlled the PZT NPs size by ultrasonication time. Using PZT NPs synthesized in a new method, we successfully fabricated ferroelectric devices on the transparent ITO substrates, using a solution-based fabrication process without high-temperature annealing process. The fabricated devices using PZT NPs exhibit superior ferroelectric and photosensitive characteristics to the PZT bulk film device. Moreover, the fabricated PZT NP photovoltaic devices show increased open circuit voltage due to its increased number of ferroelectric crystals across the device. The PZT NPs can offer low cost, a solution-based fabrication process that can be used in various applications such as NFERAM, hybrid solar cell devices and other ferroelectric device that can be fabricated on amorphous or flexible substrates. It opens the great possibility to fabricate a new concept of devices with nano-scale mixture. It also predicts a possibility of the hybrid device with various materials, such as organic materials and semiconductor nanocrystals. To the best of our knowledge, this is the first demonstration of ferroelectric devices using PZT NPs.

Chapter 7. Improvement of Efficiency of Ferroelectric PZT Photovoltaic Device with PbS Quantum Dots

7.1 Overview

Ferroelectric Pb(Zr, Ti)O₃ (PZT) thin films and PbS quantum dots (QDs) hybrid device are made for photovoltaic application, using an solution based fabrication process. The wide band gap of ferroelectric PZT can enables a high open circuit voltage. The colloidal PbS quantum dot provides a tailored absorption spectrum and an excellent light harvesting property, resulting in increased short circuit current. We present a hybrid photovoltaic device based on PZT thin film with a PbS quantum dot layer. With combination of PZT and PbS QDs, the short circuit current has increased by 8000 times, while maximizing the open circuit voltage. The overall power conversion efficiency was 0.75 % and this is more than 50 times higher than a PZT film only photovoltaic device.

7.2 Background

Upon discovery of the ferroelectric photovoltaic effect, [1, 2] ferroelectric photovoltaic (PV) have attracted increasing interest. [3-5] Recent studies have reported that the power conversion efficiency (PCE) of ferroelectric PV devices can be considerably enhanced by engineering the ferroelectric domain architectures and interfaces. [3, 6, 7] However, the

ferroelectric PV effect remained a scientific study rather than any application for PV devices, because of the low conductivity of ferroelectric materials and comparably poor PCE. There have been several reports that shows improved photovoltaic properties using a hybrid approach with ferroelectric materials and organic/inorganic materials.[3, 8] These works shows that the ferroelectric materials can boost the open circuit voltage of the photovoltaic device while increasing the short circuit current using a well matched light harvesting material.

Colloidal quantum dots offer several advantages for photovoltaic applications such as wide and tunable spectrum [9, 10] low fabrication costs associated with solution processing, [11, 12] high electron mobility compared to polymer base PV, [13] broad absorption in the near-infrared, [14] and carrier multiplication. [15-17] PbS QDs have been well studied due to its broad spectrum for light harvesting. [13, 15, 18-21] PbS based photovoltaic device showed a great potential using surface treatment [22] or structure engineering, such as funnel structure [23] or energy bandgap engineering. [16, 24] However, the small bandgap of PbS QDs limits its open circuit voltage, which is typically less than 0.3 V. [25]

In this report, we present a new approach to fabricate a hybrid PV device using ferroelectric $\text{Pb}(\text{Zr}, \text{Ti})\text{O}_3$ (PZT) and colloidal PbS QDs. Both PZT and PbS QDs can be prepared by chemical synthesis methods and they offer all solution based processes for device fabrication. This approach addresses the issues of poor light harvesting property of PZT and the small open circuit voltage of PbS PV device by taking advantages of two different materials. Our novel hybrid structure demonstrates a great improvement in PCE compared to the conventional ferroelectric photovoltaic devices.

7.3 Experiment

7.3.1 PZT Synthesis by Sol-Gel Method

Among the various fabrication method for PZT thin film, we chose a 2-methoxyethanol based sol-gel method. The sol-gel method has attracted due to its advantages of inexpensive, easy control of Zr and Ti morphology ratio and control of hydrolysis. [152] The 2-methoxyethanol reacts with the metal alkoxides to act effectively as a chelating (multi-ligand) agent which prevents the complete hydrolysis of the metal alkoxides with the addition of water. For this method, it is comparably easy to control the hydrolysis and condensation reactions. So we put in more focus on the 2-methoxyethanol based sol-gel method. In this study, all the PZT thin film was made by 2-methoxyethanol based sol-gel method.

Sol-gel derived PZT ratio was Zr : Ti = 53% : 47%, which was chosen from the ratio which would show the best ferroelectric properties. [32] The precursor materials were lead acetate trihydrate, zirconium propoxide and titanium isopropoxide. These precursors were dissolved into 2-methoxyethanol. A typical synthesis was started with dissolving 0.4 M of lead acetate trihydrate ($\text{Pb}(\text{CH}_3\text{COO})_2 \cdot 3\text{H}_2\text{O}$; 99.5%, SigmaAldrich, USA) in 2-methoxyethanol at 80 °C for 2 hours. We weighed 0.4 M of lead acetate and added 10 % more to recover the evaporation loss. [97, 108] Before dissolving in the 2-methoxyethanol solution, lead acetate powder was weighed and dried at 125 °C for 1 hour to remove the water from the acetate. After that, 2-methoxyethanol was injected with a syringe into a vacuumed flask. Vigorous magnetic stirring was used for 30 min to get a uniform solution.

After lead acetate is dissolved into the solution, 0.4 M titanium isopropoxide ($\text{Ti}[\text{OCH}(\text{CH}_3)_2]_4$; Aldrich, USA) was added to the lead-dissolved solution. In order to make sure that all titanium and the lead solution was well mixed, the mixture was stirred vigorously. When all the lead and titanium dissolved in the 2-methoxy ethanol, then only a transparent solution remained. This transparent liquid was the lead titanate precursor solution. Using the same method, 0.4 M of zirconium propoxide ($\text{Zr}(\text{OCH}_2\text{CH}_2\text{CH}_3)_4$, 70 wt. %; Aldrich, USA) was mixed into the lead titanate precursor solution. The solution was stirred at 80 °C until it turned into a transparent and uniform solution. Finally, a 2-methoxyethanol based sol-gel solution was prepared for the device fabrication, without any hydrolysis or additives.

7.3.2 Synthesis of PbS Quantum Dots

We used inexpensive, solution processed and a colloidal method for PbS QDs synthesis. In the present work, lead sulfide (PbS) QDs capped by oleic acid (OA) were synthesized by a method similar to that described by Hines and Scholes [77]. Figure 7. 1 shows the apparatus and process of colloidal synthesis for PbS QDs, explained above. (1) In a three-necked flask, a mixture of lead oxide (PbO) and oleic acid dissolved in octadecene (ODE) was heated to 125 °C for 1 hour to form lead oleate. (2) After the solution is melt well and transparent, a solution of bis(trimethylsilyl) sulfide (TMS) in octadecene was rapidly injected to lead oleate to induce nucleation and growth of the PbS quantum dots. (3) After waiting for about 15 – 20 seconds, the flask was quenched in the iced water bath with vigorous stirring. Resulting PbS QDs was centrifuged several times to get PbS QDs capped

by OA. The colloidal PbS QDs with a core diameter of approximately 3.4 nm and capped by OA were synthesized by a colloidal method and dried in the N_2 atmosphere. Finally, the dried QDs were mixed with chloroform again and ready for the device fabrication.

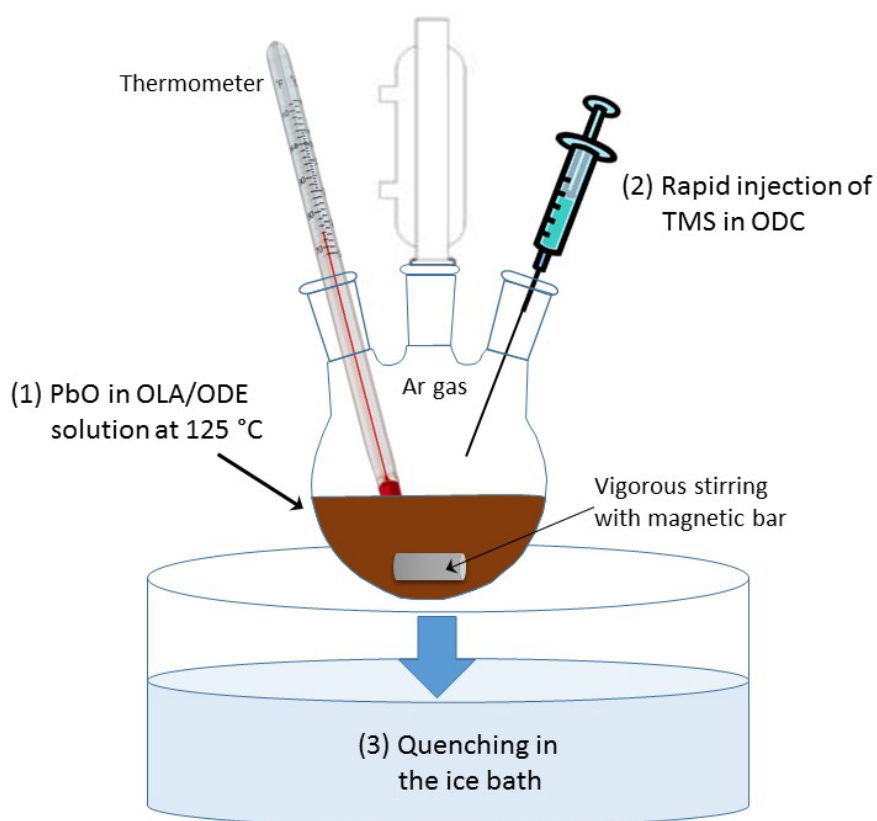


Figure. 7. 1. A cartoon that explains the brief process of colloidal synthesis for PbS QDs.

(1) PbO is melted in OA and ODE solution, resulting lead oleate solution, (2) TMS in ODC solution is rapidly injected in the lead oleate solution while vigorous stirring, (3) Quenching in the ice bath for QD size control.

7.3.3 Fabrication of PbS QD and PZT Hybrid Photovoltaic Device

The patterned indium tin oxide (ITO) coated glass substrates were purchased from Thin Film Devices, Inc. (sheet resistance of 15 ohms-cm²) and cleaned sequentially before use. The ITO-coated glass substrates were cleaned with acetone and methanol before it is treated ozone cleaning.

For the PZT PbS hybrid photovoltaic devices, prepared PZT sol-gel solution was then spin cast at 3500 rpm for 30 sec on the pre-cleaned ITO. Uniformly coated thin film PZT was annealed at 600 °C for 15 min for PZT crystallization. On the top of the perovskite PZT layer, a thin layer of poly(3,4-ethylenedioxythiophene):poly(styrene sulfonate) (PEDOT:PSS, Baytron PVP AI 4083) was spin-coated at 5000 rpm for 30 sec onto the PZT/ITO glass and then baked at 120 °C for 30 min. Then PbS QD solution was spin-cast on the substrates at 1500 rpm for 15 sec. 1,2-ethanedithiol (EDT) solution were spin-cast by passing them through a 0.45 µm filter and spin-cast at 1500 rpm for 15 sec after the PbS deposition. The concentration of the EDT is 40 µl in 1 ml acetonitrile solution, and this concentration was optimized after the several trials in various concentrations. EDT treated PbS film was followed by a rinse with pure acetonitrile. On the top of the PbS QDs thin film, we deposited a diluted PbS QD solution again. EDT treatment procedure was repeated in order to make a dense film of an ITO/PZT/PbS/Al structure. The top electrode was deposited by thermal evaporation of the 100 nm thick film of Al. A shadow mask with an area of 0.06 cm² was aligned perpendicular to the patterned ITO. [153] For the reference devices, ITO/PZT/Al and ITO/PbS/Al photovoltaic devices were fabricated with the same method explained above. Figure 7. 2 shows the cartoon of step by step fabrication process of PZT thin film and PbS QDs double layer.

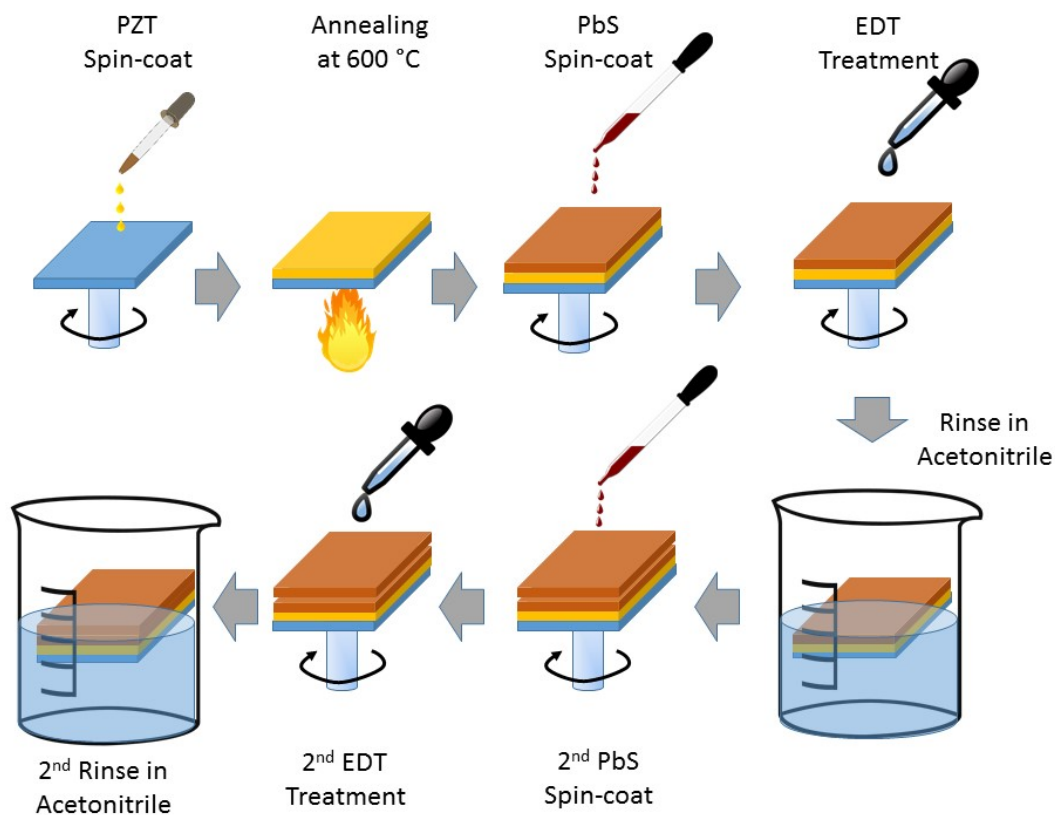


Figure. 7. 2 Schematic of the standard layer-by-layer spin-coating process starting from PZT thin film to 1st, 2nd PbS and following EDT treatment.

We applied the EDT ligand exchange, because treating with EDT concentrations lower than 0.25 M led to a dramatic improvement in both Voc and Jsc. It is believed that EDT treatment leads to replacing from oleic-acid-capped nanocrystal to thiol capped nanocrystal. This ligand exchange will lead to shrinkage in the film while EDT is replacing OA and making cracks on the nanocrystal thin film. [82] These cracks may become filled with Al during top contact deposition, leading to shorting in the device. So

when we make PbS photovoltaic device, we spin coat twice in order to prevent these cracks.

7.3.4 Electrical and Optical Characterization and Measurement

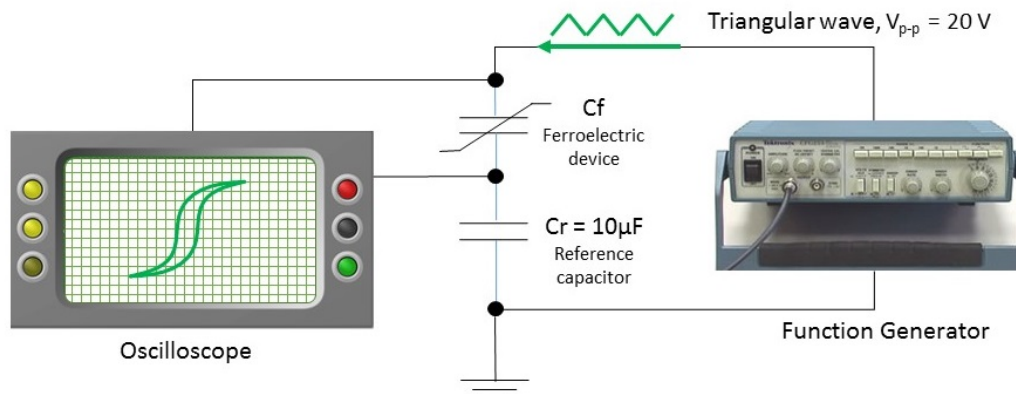


Figure. 7. 3 Schematic of the Sawyer-Tower measurement system for P-E hysteresis. In this thesis, a reference capacitor, C_r is $10\ \mu\text{F}$ with 20 V_{p-p} triangular waves from the function generator.

To investigate the crystalline structures of the synthesized ferroelectric PZT, X-ray diffraction (XRD) was performed on a Siemens 500D X-ray Diffractometer with high-

intensity CuK α radiation and 2θ step interval of 0.02. The measured X-ray peak was compared to JCPDS card and confirm the material structure.

For the absorption of the PZT/PbS-QDs and PZT photovoltaic devices, Spectrophotometer (Stellar Net Inc.) with a halogen lamp was used. A blank spectrum was taken before each measurement and subtracted from the experimental spectrum. Transmission electron microscopy (TEM) images were taken with a Phillips CM-200 using an acceleration voltage of 200 kV. Field emission scanning electron microscopy (FESEM) images were taken with a JEOL 6330F scanning electron microscope.

To investigate the PZT/PbS-QDs hybrid power conversion efficiency (PCE) characteristics, all device characterizations were performed under ambient conditions. Photovoltaic devices are measured with a Keithley 2600 under a Xe arc lamp equipped with filters to simulate the AM 1.5G (100 mW/cm²) spectrum using a solar simulator (Oriol). The current–voltage characteristics were recorded using a LabView based custom data acquisition program. For EQE measurement, devices were illuminated by a monochromator (SpectraPro-275, Acton Research Corporation) in steps of 10 nm.

7.4 Results and Discussion

7.4.1 Material Properties

A. Ferroelectric PZT

To confirm the perovskite structure of PZT thin film on TCO substrates, Indium Tin Oxide (ITO) or Fluorine doped Tin Oxide (FTO), XRD and P-E hysteresis were

measured using a TCO/PZT/Al device. As shown in Figure 7. 4 (a), we confirmed the crystalline structure of the PZT film on TCO. The bulk PZT powder (top) from the same sol-gel solution shows clear peaks. We also observed XRD peaks (middle and bottom) from an 800 nm-thick and a 140 nm-thick PZT films on a TCO/glass substrates, respectively. The upper XRD pattern in Figure 7. 4 (a) shows that (101) is the main peak from the PZT powders, which represent the crystal is rhombohedra structure. (JCPDS card No. 70-4260) [30] The lower XRD pattern shows the main peaks with (100) and (101) which is the mixture of rhombohedra and tetragonal in the film. It should be noted that the weak XRD data is due to the very thin sample thickness. Meanwhile, XRD pattern of the middle shows a more crystalized pattern, but this device showed poor current generation compared to the thin PZT layers, when we measured J-V characteristics. We presume that the higher crystallization of the thick PZT film enhanced the insulating characteristics of the ferroelectric PZT on the TCO substrates. PZT thickness of 140 nm shows the best current-voltage generation. Therefore, we chose thin PZT films (140 nm) on ITO substrate for the photovoltaic device.

Figure 7. 4 (b) is the P-E hysteresis from the PZT thin film on the ITO/glass substrate. Polarization is $0.9 \mu\text{C}/\text{cm}^2$, where the coercive field, E_c is 180 kV/cm. This result is comparable to the result from another research group. [117] Hysteresis loop is not saturated at the electric field higher than E_c . We think this non-saturated hysteresis loop is because of the lattice mismatch between the PZT and ITO/glass structure. PZT thin film is not easy to be made because of the lattice mismatch between PZT and ITO lattice constant. [147] However, we confirmed that the PZT/ITO glass device we fabricated shows a perovskite PZT properties.

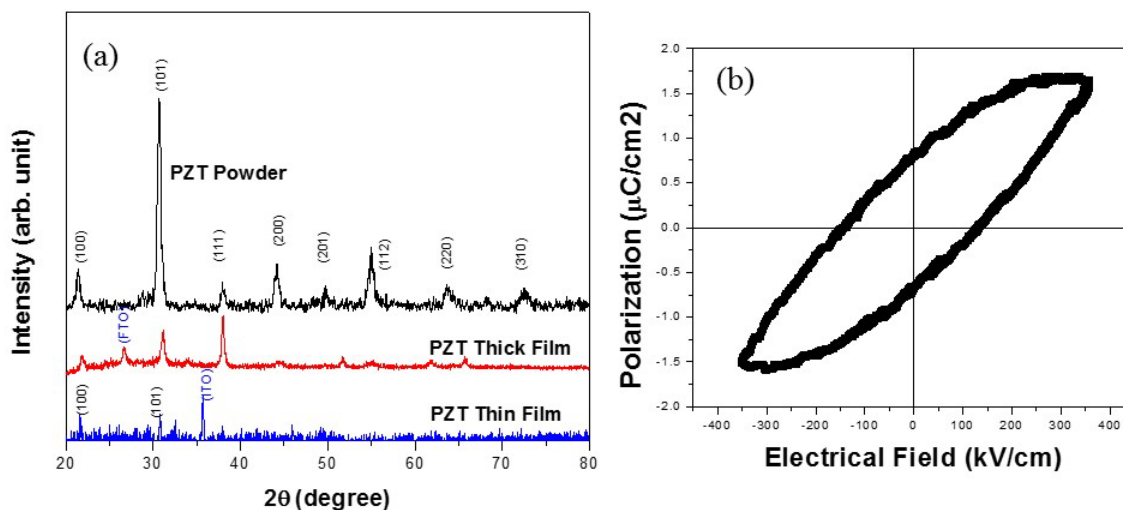


Figure 7. 4 (a) XRD comparison between PZT crystalline powder, thin film on FTO and ITO/glass substrate, (b) P-E Hysteresis form PZT thin film on ITO substrate.

B. PbS Quantum Dots

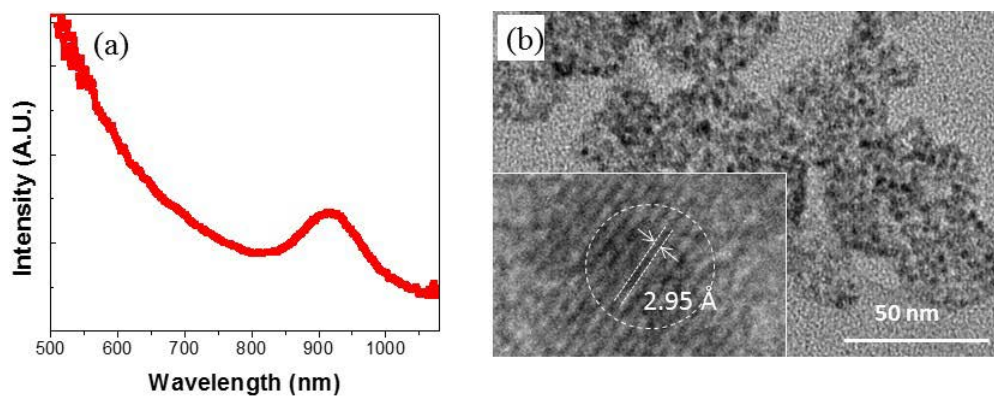


Figure 7. 5 (a) Absorption spectra of PbS QDs, where the QD absorption peak is located at 970 nm. (b) TEM image of PbS QDs, which is the size of 3.4 – 4.0 nm scale. The inset is the High-resolution TEM image of one of the QDs shown in (b) and the atomic distance represents 2.95 Å.

To confirm that the synthesized PbS QDs are the nano-crystallized semiconductor for PZT/PbS-QDs hybrid device, we measured an absorption spectroscopy and took transmission electron microscopy (TEM) images. Figure 7. 5 (a) shows the absorption spectrum of PbS QDs capped with OA. Peak absorption point from the PbS QDs is 970 nm. Since the absorption spectrum of QD depends on the quantum dot size, we calculated the diameter of the PbS quantum dots. With the optical band gap ($1.28 \text{ eV} = 1240/970 \text{ nm}$) of synthesized PbS QDs, we calculated the diameter (d in nm) of PbS QDs following the empirical equation developed by Iwan Moreels et al. [154] The diameter size of the quantum dots calculated from the absorption peak is 3.2 nm. The measured diameter from TEM image is around 3.4 – 4.0 nm with OA capped PbS QDs (Figure 7. 5 (b)), which is a little larger diameter than absorption spectrum. We think that the size difference is from the ligand surround of PbS QDs, and the size seems a little bigger from the TEM images. [62] We measured the distance between the PbS atomic crystals, which is 2.95 \AA from the inset of the high resolution TEM images. This reveals its high-crystalline nature and it is matched with bulk PbS crystal. [155]

7.4.2 Device Structures

Figure 7. 6 (a), (b) shows schematics of a PbS QDs deposited on the conventional PZT thin film and a ferroelectric PZT photovoltaic device, and PZT thin film device for reference. For the PZT/PbS-QDs hybrid device, PZT thin film with a thickness of 140 nm was prepared on transparent ITO coated glass by a sol-gel and spin-casting method, and then a PbS QDs thin film with a thickness of 200 nm was deposited on the PZT/ITO/glass structure by spin-coating, as shown in Figure 7. 6 (c).

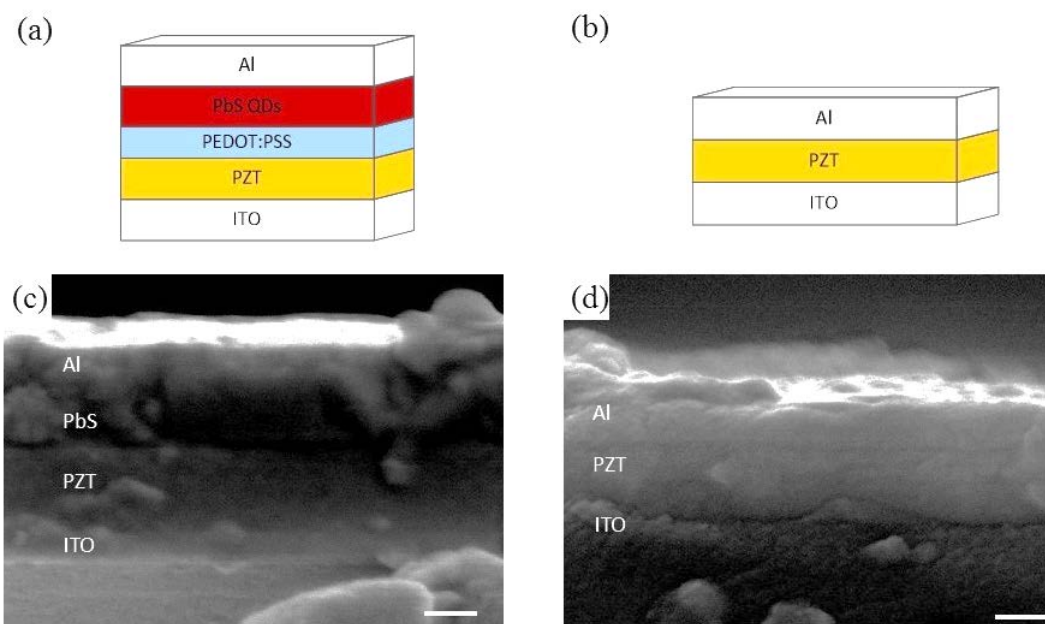


Figure 7. 6 Device structure cartoons of (a) ITO/PZT/PbS/Al hybrid device, and (b) single layer PZT on ITO substrate, respectively. Cross-sectional SEM images of (c) ITO/PZT/PbS/Al multi-layer, and (d) single layer PZT photovoltaic device.

The ITO layer is adopted here not only to act as a window layer for the incident light but also to form a Schottky barrier at the PZT/ITO interface. [19, 156] For the collection of the light-induced charges, Al electrodes were thermally evaporated on the top surface of the PbS-QDs/PZT/ITO/glass sample. As a reference sample, a typical Al/PZT/ITO/glass capacitor was prepared under identical conditions, as shown in Figure 7. 6 (d). When optoelectrical properties are measured, all the light source is incident from ITO/glass side.

Figure 7. 6 (c), (d) shows cross-sectional scanning electron microscopy (SEM) images of the two structures. The SEM imaging reveals each thin layer of PZT and PbS QDs. Since PbS QDs layer was spin-cast two times, double layer from the SEM image was observed in Figure 7. 6 (c). Because of the lattice mismatch between the PZT and ITO/glass structure, we could not observe a large grain structure from the PZT thin film. However, the PZT film shows a well-coated layer, and crystallization, which was also checked by XRD and P-E hysteresis in Figure 7. 4.

7.4.3 Photovoltaic Properties of PZT/PbS-QDs Hybrid Device

Using the same devices, J-V (current density-voltage) characteristics were measured under AM1.5G illumination at 100 mW/cm². Figure 7. 7 (a) shows the best performing J-V characteristics of each device and it is summarized at Table 1. The PCE of ferroelectric PZT only device is comparably low as anticipated (0.8×10^{-4} %), and J_{sc} and V_{oc} were 0.68 μA/cm² and 0.6 V with a fill factor (FF) of 18.5 %, respectively. We believe that the lowest efficiency is originated from the limited light absorption due to its wide bandgap (3.1 eV) and the ferroelectric insulating property. The PbS QD only device shows 0.37 % of PCE, with J_{sc} = 10.6 mA/cm², V_{oc} = 0.1 V and a FF of 35.5 %. It should be noted that the low efficiency compared to the best reported PbS only device is due to the non-optimized device structure and the fabrication process. Compared to the PZT only device, the PZT/PbS-QDs hybrid device shows a significant increase of J_{sc} (from 0.68 μA/cm² to 6.0 mA/cm²), while not much degrading high V_{oc}.

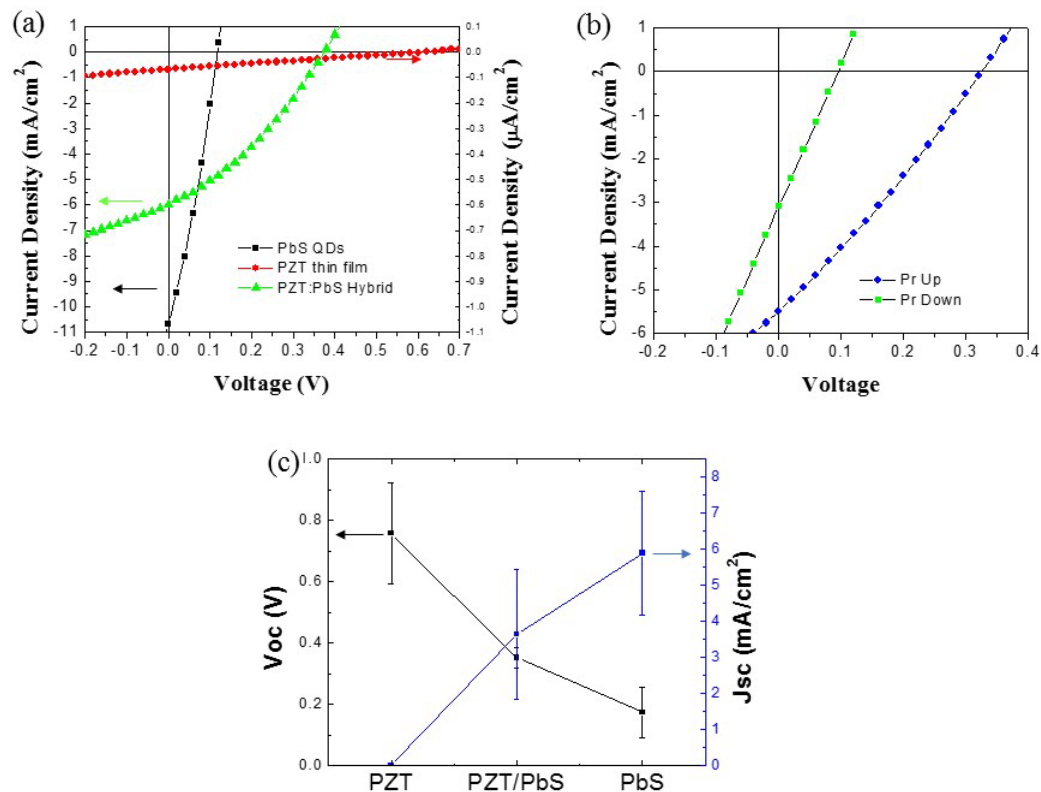


Figure 7. 7 J-V characterization of (a) PZT/PbS-QDs hybrid devices, and that of PZT, PbS for comparison. J–V characteristics measured in AM 1.5G solar simulated light for the best-performing results. (b) J-V hysteresis of PZT/PbS-QDs hybrid devices, when the polarization is up and down. (c) Plots of Voc and Jsc by each device of PZT, PbS and PZT/PbS-QDs.

We achieved almost 4 orders of magnitude larger current than the PZT only device by taking advantages from ferroelectric PZT and PbS-QDs. The measured PCE was 0.75 % and this corresponds to an improvement by more than 5 orders of magnitude compared to the best device based on a PZT only device, and by 60 % to the PbS QD only device. Figure 7. 7 (c) shows the average values of Voc and Jsc, with error bar from a dozen of devices.

The average V_{oc} of PZT only, PZT/PbS hybrid and PbS only devices are ~ 0.8 V, ~ 0.4 V and ~ 0.2 V, respectively. And the average J_{sc} of PbS only, PZT/PbS hybrid and PZT only devices are ~ 6 mA/cm², ~ 0.35 mA/cm² and a few hundred nA/cm² respectively. Overall, we achieved a 0.75 % of PCE using the hybrid structure and it is more than 50 times larger value compared to the reported PCE from an ITO/PZT/Pt device (0.011%). [3]

Table 1. Device performance for single and hybrid solar cells and respective reference devices

Device Structure	PZT Thickness [nm]	PbS Thickness [nm]	V_{oc} [V]	J_{sc} [mA/cm ²]	FF	PCE
PbS	-	198	0.1	10.6	0.35	0.37%
PZT	140	-	0.6	0.00068	0.19	0.00008%
PZT/PbS	140	198	0.38	6.00	0.33	0.75%

Figure 7. 7 (b) shows the J-V curve by the polarization up and down. A decreased photocurrent (square-line in Figure. 7. 7 (b)) can be observed when the PZT/PbS-QDs thin film is in a remnant polarization-down state, in this case, the direction of the depolarization field due to the alignment of remnant polarization is downward. On the contrary, an increased photocurrent (circle-line in Figure. 7. 7 (b)) occurs when the PZT/PbS-QDs thin film is in the remnant polarization-up state. The maximum values of the V_{oc} and J_{sc} were measured from the polarization-up state in this study. This result implies that the hybrid device can be applied not only for the photovoltaic device but also for the ferroelectric memory devices, under the light illumination. (or photovoltaic and ferroelectric memory properties at the same time)

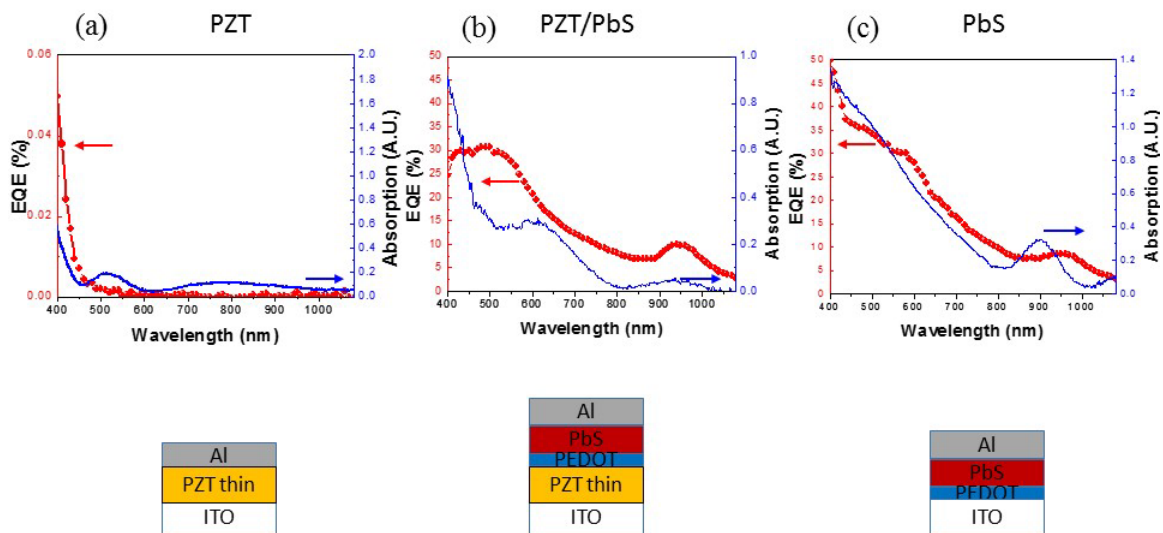


Figure 7. 8. Comparison of absorption (blue line) and external quantum efficiency (EQE, red dots) for the (a) single layer PZT, (b) PZT/PbS-QDs hybrid and (c) single layer PbS-QD devices respectively. The hybrid device consists of PZT thin film and PbS quantum dots, which is ITO/PZT/PbS-QDs/Al structure.

Figure 7. 8 (a), (b) and (c) shows the absorption spectra and the external quantum efficiency (EQE) from PZT only, PZT/PbS-QD hybrid and PbS QD only devices, respectively. The PZT/PbS-QDs device consists of a 140 nm PZT thin film and a 194 nm PbS QD film on the transparent ITO coated glass. The transparent ITO layer serves as a window for the incident light and creates a Schottky barrier at the PZT/ITO interface. [33, 34] The other reference samples were fabricated under the same condition and compared. In Figure 7. 8 (a), due to the wide bandgap of PZT (3.1 eV) and poor electrical conductivity, the PZT only device shows a very low EQE value at its absorption spectrum. Figure 7. 8 (c) shows the measured data from PbS only device and it shows well matched EQE corresponding to its excitonic peak at 970nm. The PZT/PbS-QDs

hybrid device (Figure 7. 8 (b)) shows a similar EQE curve to the PbS only device. However, it has a reduction of EQE value in its shorter wavelength range. We believe the PZT layer absorbs most of the light at the shorter wavelength regime and these generate very small photocurrent current ($0.68 \mu\text{A}/\text{cm}^2$). However, one should note that the EQE extends to NIR, primarily due to the absorption of the PbS QDs. This shows that light absorbed by both PZT thin film (UV) and PbS QDs (NIR), contribute to the photocurrent. Comparing PCE from home-made ITO/PZT/Al device (0.00005%), the novel device was improved about 10,000 times. When we compared with ITO/PZT/Pt device (0.011%), PCE was improved more than 50 times. [118]

7.5 Conclusion

In summary, we have introduced the PZT/PbS-QDs hybrid device as a novel architectural platform for ferroelectrics and solution-processed quantum dots optoelectronics and solar cells. Using solution based PZT thin film and PbS QDs, we demonstrated a simple and inexpensive fabrication method with improved photo-carrier efficiency. This approach enables to take advantages of ferroelectric PZT materials and PbS QDs for the high open circuit voltage and short circuit current, respectively. The hybrid device showed a significant improvement in short circuit current compared to PZT only device and achieved the best power conversion efficiency of 0.75 %.

Chapter 8. Summary and Future Work

Ferroelectrics are very attractive materials because they have remnant polarization, piezo electric properties and photosensitivity with high open circuit voltages. Quantum dots also interest a lot recently because of its wide absorption range, tunable wavelengths by its sizes, soluble process and easy, inexpensive synthesis method. This thesis discussed our investigations of the ferroelectric thin films, ferroelectric nanoparticles and quantum dots on their hybrid devices and a variety of functional properties. We have suggested novel devices using PZT nanoparticles and hybrid photovoltaic devices made by ferroelectric PZT and PbS quantum dots on ITO substrates. Considering the potential applications, the major functional properties of PZT thin films and nanoparticles have been carefully examined focusing on their structural, electrical and optical properties where ferroelectric and photosensitive behaviors of PZT nanoparticle films and semiconductor properties of PZT/PbS Quantum Dots device were put many efforts in most of the study.

In this thesis, we have shown mainly two devices to achieve solar power via very low cost techniques. First device is PZT nanoparticle photosensitive device which has advantages of low temperature, low cost and soluble process. The second device is PZT/PbS-QDs hybrid photovoltaic device introducing the possibility of the high V_{oc} from ferroelectric materials and high current from semiconductor nanocrystals, which showed the enhancement of power conversion efficiency. To understand the background and underlying physics related to our approach, we reviewed the theoretical aspects of the

ferroelectric and semiconductor nanocrystal materials, and its properties and applications in Chapter 2 and Chapter 3 respectively. Then, in the following chapter, several growth parameters are discussed to explain their specific influences on the growth of ferroelectric thin films and ferroelectric nanoparticles. Furthermore, the importance of growth temperature and surface treatment of the quantum dots are emphasized that the photovoltaic efficiency was influenced by the quantum dots growth and the surface conditions.

In chapter 5, we demonstrated a simple PZT based device and its characteristics. perovskite PZT thin film photovoltaic devices have been fabricated by the sol-gel method, with 600 °C under oxygen-rich environment, in order to compare the conventional technology to the following PZT nanoparticles we introduced in the next chapter. Basic optical and electrical properties were measured and analyzed. With those basic data, we could understand material and device properties like ferroelectric hysteresis, energy bandgap, and photosensitive properties of the PZT materials and its devices. We also showed a Schottky metal contact between ferroelectric and ITO layers provides a high Voc at the interface of PZT and ITO.

Then, we extended our research to a low-temperature device fabrication method using PZT. Our approach was to prepare a nanostructured PZT materials that is prepared in a solution. Sol-gel synthesis has been used successfully to produce PZT nano-size powders having a 30 – 100 nm size and a narrow particle size distribution (Chapter 6). It has been found that the chemical hydrolysis condition from a sol-gel process, inert gas treatment, the treating temperature and ultra-sonication energy given to the nanoparticles are the most important parameters in determining the nano-phase formation and particle size.

With synthesized PZT nanoparticles, we introduced novel photosensitive device and showed that the new aspect of the PZT materials when it is in the nano-size particles, for the first time. Ferroelectric characterization clearly exhibited the abrupt polarization switch near the coercive fields even in the nano-scale, and values of remnant polarization with $+Pr = \sim 1 \text{ nC/cm}^2$ and $Ec = \sim 10 \text{ kV/cm}$. Ferroelectric nanoparticle films have shown the potential for the applications of a novel or new generation devices, with great potential for low temperature fabrication as a substrate-free device, such as a flexible or an organic substrate devices, without considering lattice matching.

Finally, in Chapter 7, the combination of attractive properties of PZT/PbS-QDs systems prospects for a potentially novel or new generation devices. Novel studies on the integration of those two materials showed the great improvement of photo-generated current due to quantum dots and V_{oc} improvement due to ferroelectric PZT layer. Resulting efficiency improvement was more than 50 times compared to the conventional PZT photosensitive device. In this chapter, we also describe the growth of highly oriented PbS quantum dots by a colloidal method. We have also shown the feasibility for a high open circuit voltage formed at the interface between the ferroelectric thin film and ITO substrate.

Consequently, future research work embraces investigations on PZT nanoparticles since it has more interesting properties such as piezoelectricity and pyroelectricity. Furthermore, nano-scale ferroelectric materials can be applied any micro or nano size devices such as FET, MEMs, acoustic and photosensing devices. We showed the PZT nanoparticles are synthesized with pre-heating and it can be fabricated on any room-temperature substrates without considering the substrated lattice match which is

important for the ferroelectric crystallization. For example, PZT NPs can be made on a flexible substrates such as a conductive tape, or on a nano-scale substrates such as FET channels, MEMs cantilevers and inside organic nanostructures.

Especially, we showed that ferroelectric-quantum dots (FE-QDs) device for the first time, as we know of, further efficient power conversion structure and the device could be accomplished, taking advantages from ferroelectrics and quantum dots. If we can control more sophisticated way, the nano-scale heterojunction device also could be interesting. We showed not only the advantages from the photovoltaic efficiency, we also showed that the device have a ferroelectric polarization effect from the device. I think that it also can be researched dynamic devices using the polarization effect. For example, FET device is a switch using gate and source/drain voltages. However, if we use ferroelectric materials for the gate insulator layer, then we have another controlling factor of the FET device using its ferroelectric polarization effect.

References

1. 2010 *Solar technologies market report*. NREL, 2010.
2. Weickert, J., et al., *Nanostructured organic and hybrid solar cells*. *Advanced Materials*, 2011. **23**(16): p. 1810-1828.
3. Nozik, A.J., *Quantum dot solar cells*. *Physica E: Low-dimensional Systems and Nanostructures*, 2002. **14**(1–2): p. 115-120.
4. Schaller, R.D. and V.I. Klimov, *High efficiency carrier multiplication in PbSe nanocrystals: Implications for solar energy conversion*. *Physical Review Letters*, 2004. **92**(18): p. 186601.
5. Kim, S.J., et al., *Multiple exciton generation and electrical extraction from a PbSe quantum dot photoconductor*. *Applied Physics Letters*, 2008. **92**(3): p. 031107-3.
6. Graetzel, M., et al., *Materials interface engineering for solution-processed photovoltaics*. *Nature*, 2012. **488**(7411): p. 304-312.
7. Michalet, X., et al., *Quantum dots for live cells, in vivo imaging, and diagnostics*. *Science*, 2005. **307**(5709): p. 538-544.
8. Gao, J., et al., *n-Type transition metal oxide as a hole extraction layer in PbS quantum dot solar cells*. *Nano Letters*, 2011. **11**(8): p. 3263-3266.
9. Luther, J.M., et al., *Schottky solar cells based on colloidal nanocrystal films*. *Nano Letters*, 2008. **8**(10): p. 3488-3492.
10. Yang, S.Y., et al., *Above-bandgap voltages from ferroelectric photovoltaic devices*. *Nat Nano*, 2010. **5**(2): p. 143-147.
11. Devi, P.I. and K. Ramachandran, *Hybridized PVDF/PbS nanocomposites for solar cell applications*. *AIP Conference Proceedings*, 2010. **1276**(1): p. 183-188.
12. Nalwa, K.S., et al., *Enhanced charge separation in organic photovoltaic films doped with ferroelectric dipoles*. *Energy & Environmental Science*, 2012. **5**(5): p. 7042-7049.
13. Yuan, Y., et al., *Efficiency enhancement in organic solar cells with ferroelectric polymers*. *Nat Mater*, 2011. **10**(4): p. 296-302.
14. Huang, H., *Solar energy: Ferroelectric photovoltaics*. *Nat Photon*, 2010. **4**(3): p. 134-135.

15. Busch, G., *Early history of ferroelectricity*. *Ferroelectrics*, 1987. **74**(1): p. 267-284.
16. Chilibon, I. and J. Marat-Mendes, *Ferroelectric ceramics by sol-gel methods and applications: a review*. *Journal of Sol-Gel Science and Technology*, 2012. **64**(3): p. 571-611.
17. Dawber, M., K.M. Rabe, and J.F. Scott, *Physics of thin-film ferroelectric oxides*. *Reviews of Modern Physics*, 2005. **77**(4): p. 1083-1130.
18. Fridkin, V.M., *Bulk photovoltaic effect in noncentrosymmetric crystals*. *Crystallography Reports*, 2001. **46**(4): p. 654-658.
19. Cao, D., et al., *High-efficiency ferroelectric-film solar cells with an n-type Cu₂O cathode buffer Layer*. *Nano Letters*, 2012. **12**(6): p. 2803-2809.
20. Chen, B., et al., *Tunable photovoltaic effects in transparent Pb(Zr_{0.53}Ti_{0.47})O₃ capacitors*. *Applied Physics Letters*, 2012. **100**(17): p. 173903-4.
21. Cuadras, A., M. Gasulla, and V. Ferrari, *Thermal energy harvesting through pyroelectricity*. *Sensors and Actuators A: Physical*, 2010. **158**(1): p. 132-139.
22. Delimova, L.A. and V.S. Yuferev, *High retention of the polarization and depolarization field in polycrystalline metal/Pb(ZrTi)O₃/metal capacitors*. Vol. 108. 2010: *Journal of Applied Physics*. 084110.
23. Qin, M., K. Yao, and Y.C. Liang, *High efficient photovoltaics in nanoscaled ferroelectric thin films*. *Applied Physics Letters*, 2008. **93**(12): p. 122904-3.
24. Zhang, J., et al., *Enlarging photovoltaic effect: combination of classic photoelectric and ferroelectric photovoltaic effects*. *Sci. Rep.*, 2013. **3**: p. 2109-6.
25. Haertling, G.H., *Ferroelectric ceramics: History and technology*. *Journal of the American Ceramic Society*, 1999. **82**(4): p. 797-818.
26. Damjanovic, D., *Comments on origins of enhanced piezoelectric properties in ferroelectrics*. *Ultrasonics, Ferroelectrics, and Frequency Control, IEEE Transactions on*, 2009. **56**(8): p. 1574-1585.
27. Tao, W., S.B. Desu, and T.K. Li, *Direct liquid injection MOCVD of high quality PLZT films*. *Materials Letters*, 1995. **23**(4-6): p. 177-180.
28. Schmitt, L.A., et al., *The impact of heat treatment on the domain configuration and strain behavior in Pb[Zr,Ti]O₃ ferroelectrics*. *Journal of the American Ceramic Society*, 2015. **98**(1): p. 269-277.

29. Defay, E., *Integration of ferroelectric and piezoelectric thin films*. Wiley, 2011: p. 32.
30. Lang, X.Y. and Q. Jiang, *Size and interface effects on Curie temperature of perovskite ferroelectric nanosolids*. Journal of Nanoparticle Research, 2007. **9**(4): p. 595-603.
31. Kanno, I., et al., *Crystallographic characterization of epitaxial Pb(Zr,Ti)O₃ films with different Zr/Ti ratio grown by radio-frequency-magnetron sputtering*. Journal of Applied Physics, 2003. **93**(7): p. 4091-4096.
32. Noheda, B., et al., *The monoclinic phase in PZT: New light on morphotropic phase boundaries*. AIP Conference Proceedings, 2000. **535**(1): p. 304-313.
33. Sangsubun, C., A. Watcharapasorn, and S. Jiansirisomboon, *Sol-Gel derived PZT and PZTN ceramics: A role of sintering temperature*. Ferroelectrics, 2009. **382**(1): p. 147-152.
34. Chae, B.G., et al., *Comparative analysis for the crystalline and ferroelectric properties of Pb(Zr,Ti)O₃ thin films deposited on metallic LaNiO₃ and Pt electrodes*. Thin Solid Films, 2002. **410**(1-2): p. 107-113.
35. Jie, W., et al., *Ferroelectric polarization effects on the transport properties of graphene/PMN-PT field effect transistors*. The Journal of Physical Chemistry C, 2013. **117**(26): p. 13747-13752.
36. Glass, A.M., D. von der Linde, and T.J. Negran, *High-voltage bulk photovoltaic effect and the photorefractive process in LiNbO₃*. Applied Physics Letters, 1974. **25**(4): p. 233-235.
37. Noginova, N., et al., *Photoinduced electric current in Fe-doped KNbO₃*. Journal of the Optical Society of America B, 1997. **14**(6): p. 1390-1395.
38. Dalba, G., et al., *Giant bulk photovoltaic effect under linearly polarized X-ray synchrotron radiation*. Physical Review Letters, 1995. **74**(6): p. 988-991.
39. Yang, Y.S., et al., *Schottky barrier effects in the photocurrent of sol-gel derived lead zirconate titanate thin film capacitors*. Applied Physics Letters, 2000. **76**(6): p. 774-776.
40. Poosanaas, P., et al., *Influence of sample thickness on the performance of photostrictive ceramics*. Journal of Applied Physics, 1998. **84**(3): p. 1508-1512.
41. Pintilie, L., et al., *Short-circuit photocurrent in epitaxial lead zirconate-titanate thin films*. Journal of Applied Physics, 2007. **101**(6): p. 064109-8.
42. Choi, T., et al., *Switchable ferroelectric diode and photovoltaic effect in BiFeO₃*. Science, 2009. **324**(5923): p. 63-66.

43. Yang, Y.S., et al., *Schottky barrier effects in the electronic conduction of sol-gel derived lead zirconate titanate thin film capacitors*. Journal of Applied Physics, 1998. **84**(9): p. 5005-5011.
44. Muralt, P., *Ferroelectric thin films for micro-sensors and actuators: a review*. Journal of Micromechanics and Microengineering, 2000. **10**(2): p. 136.
45. al., G.A.S.e., *Ferroelectricity and related materials*. Gordon and Breach Science Publishers, 1984(New York): p. 18.
46. Randall, C.A., et al., *Intrinsic and extrinsic size effects in fine-grained morphotropic-phase-boundary lead zirconate titanate ceramics*. Journal of the American Ceramic Society, 1998. **81**(3): p. 677-688.
47. B. Jaffe, W.R.C., H. Jaffe, *Piezoelectric Ceramics*, 1971(Academic Press, London): p. 136.
48. Sambur, J.B., T. Novet, and B.A. Parkinson, *Multiple exciton collection in a sensitized photovoltaic system*. Science, 2010. **330**(6000): p. 63-66.
49. Ma, W., et al., *Photovoltaic performance of ultras-small PbSe quantum dots*. ACS Nano, 2011. **5**(10): p. 8140-8147.
50. Kuo, C.-Y., et al., *Ligands affect the crystal structure and photovoltaic performance of thin films of PbSe quantum dots*. Journal of Materials Chemistry, 2011. **21**(31): p. 11605-11612.
51. Rafailov, E.U., *The physics and engineering of compact quantum dot-based laser for biophotonics*. Wiley-VCH, 2014.
52. Richard, L., *Introductory quantum mechanics*. Addison-Wesley, 1980. **4th**.
53. Murray, C.B., D.J. Norris, and M.G. Bawendi, *Synthesis and characterization of nearly monodisperse CdE (E = sulfur, selenium, tellurium) semiconductor nanocrystallites*. Journal of the American Chemical Society, 1993. **115**(19): p. 8706-8715.
54. Pinaud, F., et al., *Advances in fluorescence imaging with quantum dot bio-probes*. Biomaterials, 2006. **27**(9): p. 1679-1687.
55. Dai, X., et al., *Solution-processed, high-performance light-emitting diodes based on quantum dots*. Nature, 2014. **515**(7525): p. 96-99.
56. Sugawara, M., et al., *Effect of homogeneous broadening of optical gain on lasing spectra in self-assembled In Ga As / GaAs quantum dot lasers*. Physical Review B, 2000. **61**(11): p. 7595-7603.

57. Ledentsov, N.N., *Quantum dot laser*. Semiconductor Science and Technology, 2011. **26**(1): p. 014001.
58. Richter, A., et al., *Improved quantitative description of Auger recombination in crystalline silicon*. Physical Review B, 2012. **86**(16): p. 165202.
59. Nozik, A.J., et al., *Semiconductor quantum dots and quantum dot arrays and applications of multiple exciton generation to third-generation photovoltaic solar cells*. Chemical Reviews, 2010. **110**(11): p. 6873-6890.
60. Chuang, C.-H.M., et al., *Improved performance and stability in quantum dot solar cells through band alignment engineering*. Nat Mater, 2014. **13**(8): p. 796-801.
61. Kim, J.Y., et al., *25th anniversary article: Colloidal quantum dot materials and devices: A quarter-century of advances*. Advanced Materials, 2013. **25**(36): p. 4986-5010.
62. Xu, F., et al., *Impact of different surface ligands on the optical properties of PbS quantum dot solids*. Materials, 2015. **8**(4): p. 1858.
63. Cooney, R.R., et al., *Breaking the phonon bottleneck for holes in semiconductor quantum dots*. Physical Review Letters, 2007. **98**(17): p. 177403.
64. PREZHDO, O.V., *Photoinduced dynamics in semiconductor quantum dots: Insights from time-domain ab initio studies*. Acc. Chem. Res, 2009. **42**: p. 2005.
65. Sukhovatkin, V., et al., *Colloidal quantum-dot photodetectors exploiting multiexciton generation*. Science, 2009. **324**(5934): p. 1542-1544.
66. Semonin, O.E., et al., *Peak external photocurrent quantum efficiency exceeding 100% via MEG in a quantum dot solar cell*. Science (New York, N.Y.), 2011. **334**(6062): p. 1530-1533.
67. Padilha, L.A., et al., *Carrier multiplication in semiconductor nanocrystals: Influence of size, shape, and composition*. Accounts of Chemical Research, 2013. **46**(6): p. 1261-1269.
68. Bartnik, A.C., et al., *Electronic states and optical properties of PbSe nanorods and nanowires*. Physical Review B, 2010. **82**(19): p. 195313.
69. Mahler, B., et al., *Towards non-blinking colloidal quantum dots*. Nat Mater, 2008. **7**(8): p. 659-664.
70. Nirmal, M., et al., *Observation of the "dark exciton" in CdSe quantum dots*. Physical Review Letters, 1995. **75**(20): p. 3728-3731.

71. Katz, E. and I. Willner, *Integrated nanoparticle-biomolecule hybrid systems: Synthesis, properties, and applications*. Angewandte Chemie-International Edition, 2004. **43**(45): p. 6042-6108.
72. Peng, X., et al., *Shape control of CdSe nanocrystals*. Nature, 2000. **404**(6773): p. 59-61.
73. Zhitomirsky, D., et al., *Engineering colloidal quantum dot solids within and beyond the mobility-invariant regime*. Nat Commun, 2014. **5**.
74. LaMer, V.K. and R.H. Dinegar, *Theory, production and mechanism of formation of monodispersed hydrosols*. Journal of the American Chemical Society, 1950. **72**(11): p. 4847-4854.
75. C. B. Murray, S.S., W. Gaschler, H. Doyle, T. A. Betley, C.R. Kagan, *Colloidal synthesis of nanocrystals and nanocrystal superlattices*. IBM J. Res. & Dev., 2001. **45**: p. 47.
76. Xu, J., J.-P. Ge, and Y.-D. Li, *Solvothermal synthesis of monodisperse PbSe nanocrystals*. The Journal of Physical Chemistry B, 2006. **110**(6): p. 2497-2501.
77. Hines, M.A. and G.D. Scholes, *Colloidal PbS nanocrystals with size-tunable near-infrared emission: Observation of post-synthesis self-narrowing of the particle size distribution*. Advanced Materials, 2003. **15**(21): p. 1844-1849.
78. Jincheng, L., et al., *Size-tunable near-infrared PbS nanoparticles synthesized from lead carboxylate and sulfur with oleylamine as stabilizer*. Nanotechnology, 2008. **19**(34): p. 345602.
79. Hines, M.A. and P. Guyot-Sionnest, *Synthesis and characterization of strongly luminescing ZnS-capped CdSe nanocrystals*. The Journal of Physical Chemistry, 1996. **100**(2): p. 468-471.
80. Johnston, K.W., et al., *Schottky-quantum dot photovoltaics for efficient infrared power conversion*. Applied Physics Letters, 2008. **92**(15): p. 151115-3.
81. Koleilat, G.I., et al., *Efficient, stable infrared photovoltaics based on solution-cast colloidal quantum dots*. ACS Nano, 2008. **2**(5): p. 833-840.
82. Barkhouse, D.A.R., et al., *Thiols passivate recombination centers in colloidal quantum dots leading to enhanced photovoltaic device efficiency*. ACS Nano, 2008. **2**(11): p. 2356-2362.
83. Sun, S., et al., *Monodisperse FePt nanoparticles and ferromagnetic FePt nanocrystal superlattices*. Science, 2000. **287**(5460): p. 1989-1992.

84. Steckel, J.S., et al., *1.3 μm to 1.55 μm tunable electroluminescence from PbSe quantum dots embedded within an organic device*. *Advanced Materials*, 2003. **15**(21): p. 1862-1866.
85. Wang, X., et al., *Tandem colloidal quantum dot solar cells employing a graded recombination layer*. *Nat Photon*, 2011. **5**(8): p. 480-484.
86. Kang, Q., et al., *Fabrication of PbS nanoparticle-sensitized TiO₂ nanotube arrays and their photoelectrochemical properties*. *ACS Applied Materials & Interfaces*, 2011. **3**(3): p. 746-749.
87. Tang, J., et al., *Schottky quantum dot solar cells stable in air under solar illumination*. *Advanced Materials*, 2010. **22**(12): p. 1398-1402.
88. Konstantatos, G., et al., *Ultrasensitive solution-cast quantum dot photodetectors*. *Nature*, 2006. **442**(7099): p. 180-183.
89. Kramer, I.J., et al., *Solar cells using quantum funnels*. *Nano Letters*, 2011. **11**(9): p. 3701-3706.
90. Tang, J., et al., *Colloidal-quantum-dot photovoltaics using atomic-ligand passivation*. *Nat Mater*, 2011. **10**(10): p. 765-771.
91. Konstantatos, G. and E.H. Sargent, *PbS colloidal quantum dot photoconductive photodetectors: Transport, traps, and gain*. *Applied Physics Letters*, 2007. **91**(17): p. 173505.
92. Ip, A.H., et al., *Hybrid passivated colloidal quantum dot solids*. *Nat Nano*, 2012. **7**(9): p. 577-582.
93. Uprety, K.K., L.E. Ocola, and O. Auciello, *Growth and characterization of transparent Pb(Zr,Ti)O₃ capacitor on glass substrate*. Vol. 102. 2007: AIP. 084107.
94. Zhu, Y., et al., *Laser-assisted low temperature processing of Pb(Zr,Ti)O₃ thin film*. Vol. 73. 1998: Journal of Applied Physics. 1958-1960.
95. Liu, S.W. and M. Xiao, *Electro-optic switch in ferroelectric thin films mediated by surface plasmons*. *Applied Physics Letters*, 2006. **88**(14).
96. Zhang, M., et al., *Composition dependence of the photochemical reduction of Ag⁺ by as-grown Pb(Zr_xTi_{1-x})O₃ films on indium tin oxide electrode*. *Applied Physics Letters*, 2013. **103**(10): p. 102902-4.
97. Zhang, X.Y., et al., *Synthesis and piezoresponse of highly ordered Pb(Zr_{0.53}Ti_{0.47})O₃ nanowire arrays*. *Applied Physics Letters*, 2004. **85**(18): p. 4190-4192.

98. Ricote, J., et al., *Fabrication of continuous ultrathin ferroelectric films by chemical solution deposition methods*. Journal of Materials Research, 2008. **23**(10): p. 2787-2795.
99. Kidoh, H., et al., *Ferroelectric properties of lead-zirconate-titanate films prepared by laser ablation*. Applied Physics Letters, 1991. **58**(25): p. 2910-2912.
100. Kim, Y.-M., W.-J. Lee, and H.-G. Kim, *Deposition of PZT films by MOCVD at low temperature and their change in properties with annealing temperature and Zr/Ti ratio*. Thin Solid Films, 1996. **279**(1-2): p. 140-144.
101. Livage, J., M. Henry, and C. Sanchez, *Sol-gel chemistry of transition metal oxides*. Progress in Solid State Chemistry, 1988. **18**(4): p. 259-341.
102. Zhenxing, B., Z. Zhisheng, and F. Panfeng, *Characterization of PZT ferroelectric thin films by RF-magnetron sputtering*. Journal of Physics: Conference Series, 2007. **61**(1): p. 120.
103. Smith, H.M. and A.F. Turner, *Vacuum deposited thin films using a ruby laser*. Applied Optics, 1965. **4**(1): p. 147-148.
104. Dijkkamp, D., et al., *Preparation of Y-Ba-Cu oxide superconductor thin films using pulsed laser evaporation from high Tc bulk material*. Applied Physics Letters, 1987. **51**(8): p. 619-621.
105. Jones, A.C., *MOCVD of electroceramic oxides: A precursor manufacturer's perspective*. Chemical Vapor Deposition, 1998. **4**(5): p. 169-179.
106. Krupanidhi, S.B., et al., *rf planar magnetron sputtering and characterization of ferroelectric Pb(Zr,Ti)O₃ films*. Journal of Applied Physics, 1983. **54**(11): p. 6601-6609.
107. Liu, C., et al., *Sol-gel synthesis of free-standing ferroelectric lead zirconate titanate nanoparticles*. Journal of the American Chemical Society, 2001. **123**(18): p. 4344-4345.
108. Zak, A.K. and W.H. Abd Majid, *Effect of solvent on structure and optical properties of PZT nanoparticles prepared by sol-gel method, in infrared region*. Ceramics International, 2011. **37**(3): p. 753-758.
109. Pern, J., APP International PV Reliability Workshop, 2008. **Dec. 4-5**(SJTU).
110. Yang, X., et al., *Enhancement of photocurrent in ferroelectric films via the incorporation of narrow bandgap nanoparticles*. Advanced Materials, 2012. **24**(9): p. 1202-1208.
111. Yuan, Y., et al., *Arising applications of ferroelectric materials in photovoltaic devices*. Journal of Materials Chemistry A, 2014. **2**(17): p. 6027-6041.

112. Kakegawa, K., et al., *A compositional fluctuation and properties of Pb(Zr, Ti)O₃*. Solid State Communications, 1977. **24**(11): p. 769-772.
113. Ghasemifard, M., et al., *Microstructural and optical characterization of PZT nanopowder prepared at low temperature*. Physica E: Low-dimensional Systems and Nanostructures, 2009. **41**(3): p. 418-422.
114. Ji, W., K. Yao, and Y.C. Liang, *Bulk photovoltaic effect at visible wavelength in epitaxial ferroelectric BiFeO₃ thin films*. Advanced Materials, 2010. **22**(15): p. 1763-1766.
115. Shur, M., *Physics of semiconductor devices*. Prentice-Hall 1990.
116. Scott, J.F., *In advanced microelectronics series*. Springer-Verlag, 2000(Berlin).
117. Pandey, S.K., et al., *Structural, ferroelectric and optical properties of PZT thin films*. Physica B: Condensed Matter, 2005. **369**(1-4): p. 135-142.
118. Zheng, F., et al., *Above 1% efficiency of a ferroelectric solar cell based on the Pb(Zr,Ti)O₃ film*. Journal of Materials Chemistry A, 2014. **2**(5): p. 1363-1368.
119. Vu Ngoc, H., et al., *Improvement of electrical property for Pb(Zr 0.53 Ti 0.47)O₃ ferroelectric thin film deposited by sol-gel method on SRO electrode*. Journal of Physics: Conference Series, 2009. **187**(1): p. 012063.
120. Teen-Hang Meen, S.P., Artde Donald Kin-Tak Lam, *Innovation in design, communication and engineering*. Proceedings of the 2014 3rd international conference on innovation, communication and engineering (ICICE 2014), 2014: p. 914.
121. Evans, J.T. and R. Womack, *An experimental 512-bit nonvolatile memory with ferroelectric storage cell*. Solid-State Circuits, IEEE Journal of, 1988. **23**(5): p. 1171-1175.
122. Setter, N., et al., *Ferroelectric thin films: Review of materials, properties, and applications*. Journal of Applied Physics, 2006. **100**(5): p. 051606.
123. Wang, Z.L., *Progress in piezotronics and piezo-phototronics*. Advanced Materials, 2012. **24**(34): p. 4632-4646.
124. Bin, C., et al., *Effect of top electrodes on photovoltaic properties of polycrystalline BiFeO₃ based thin film capacitors*. Nanotechnology, 2011. **22**(19): p. 195201.
125. Naber, R.C.G., et al., *High-performance solution-processed polymer ferroelectric field-effect transistors*. Nat Mater, 2005. **4**(3): p. 243-248.

126. Glass, A.M., D. von der Linde, and T.J. Negran, *High-voltage bulk photovoltaic effect and the photorefractive process in LiNbO₃*. Applied Physics Letters, 1974. **25**(4): p. 233-235.
127. Yang, S.Y., et al., *Above-bandgap voltages from ferroelectric photovoltaic devices*. Nat Nano. **5**(2): p. 143-147.
128. Zhenghu, Z., et al., *Preparation and ferroelectric properties of freestanding Pb(Zr,Ti)O₃ thin membranes*. Journal of Physics D: Applied Physics, 2012. **45**(18): p. 185302.
129. Pontes, D.S.L., et al., *Synthesis, optical and ferroelectric properties of PZT thin films: experimental and theoretical investigation*. Journal of Materials Chemistry, 2012. **22**(14): p. 6587-6596.
130. Alexe, M. and D. Hesse, *Self-assembled nanoscale ferroelectrics*. Journal of Materials Science, 2006. **41**(1): p. 1-11.
131. Faheem, Y. and M. Shoaib, *Sol-gel processing and characterization of phase-pure lead zirconate titanate nano-powders*. Journal of the American Ceramic Society, 2006. **89**(6): p. 2034-2037.
132. Chen, S.-Y. and I.W. Chen, *Temperature–time texture transition of Pb(Zr_{1-x}Ti_x)O₃ thin films: II, heat treatment and compositional effects*. Journal of the American Ceramic Society, 1994. **77**(9): p. 2337-2344.
133. Yu, J.-C., et al., *Compatibility of material processing and fabrication of sol-gel derived PZT based devices*. Ferroelectrics, 2009. **383**(1): p. 127-132.
134. Law, C.W., et al., *Effect of oxygen content and thickness of sputtered RuO_x electrodes on the ferroelectric and fatigue properties of sol–gel PZT thin films*. Thin Solid Films, 1999. **354**(1–2): p. 162-168.
135. Neurgaonkar, R.R., et al., *Grain oriented ferroelectric PZT thin films on lattice-matched substrates*. Materials Research Bulletin, 1993. **28**(7): p. 719-727.
136. Bernal, A., et al., *Free-standing ferroelectric nanotubes processed via soft-template Infiltration*. Advanced Materials, 2012. **24**(9): p. 1160-1165.
137. Yuriy, G., Z. Olena, and G. Anatoliy, *Emerging applications of ferroelectric nanoparticles in materials technologies, biology and medicine*. 2012.
138. Joshi, U.A. and J.S. Lee, *Template-free hydrothermal synthesis of single-crystalline barium titanate and strontium titanate nanowires*. Small, 2005. **1**(12): p. 1172-1176.

139. Varghese, J., R.W. Whatmore, and J.D. Holmes, *Ferroelectric nanoparticles, wires and tubes: synthesis, characterisation and applications*. Journal of Materials Chemistry C, 2013. **1**(15): p. 2618-2638.
140. Michael, T., S. Trimper, and J.M. Wesselinowa, *Size and doping effects on the coercive field of ferroelectric nanoparticles: A microscopic model*. Physical Review B, 2006. **74**(21): p. 214113.
141. Basun, S.A., et al., *Dipole moment and spontaneous polarization of ferroelectric nanoparticles in a nonpolar fluid suspension*. Physical Review B, 2011. **84**(2): p. 024105.
142. Xu, G., et al., *Hydrothermal synthesis of lead zirconate titanate nearly free-standing nanoparticles in the size regime of about 4 nm*. Crystal Growth & Design, 2009. **9**(1): p. 13-16.
143. Faheem, Y. and K.S. Joya, *Phase transformation and freestanding nanoparticles formation in lead zirconate titanate derived by sol-gel*. Applied Physics Letters, 2007. **91**(6): p. 063115-3.
144. Izyumskaya, N., et al., *Processing, structure, properties, and applications of PZT thin films*. Critical Reviews in Solid State and Materials Sciences, 2007. **32**(3-4): p. 111-202.
145. Cao, W. and C.A. Randall, *Grain size and domain size relations in bulk ceramic ferroelectric materials*. Journal of Physics and Chemistry of Solids, 1996. **57**(10): p. 1499-1505.
146. Li, D.B., et al., *Polarization reorientation in ferroelectric lead zirconate titanate thin films with electron beams*. Journal of Materials Research, 2006. **21**(04): p. 935-940.
147. Nadaud, N., et al., *Structural studies of Tin-doped Indium Oxide (ITO) and In₄Sn₃O₁₂*. Journal of Solid State Chemistry, 1998. **135**(1): p. 140-148.
148. Speck, J.S., et al., *Domain configurations due to multiple misfit relaxation mechanisms in epitaxial ferroelectric thin films. II. Experimental verification and implications*. Journal of Applied Physics, 1994. **76**(1): p. 477-483.
149. Wang, Y., et al., *Ultrathin ferroelectric films: growth, characterization, physics and applications*. Materials, 2014. **7**(9): p. 6377.
150. Koch, W.T.H., et al., *Bulk photovoltaic effect in BaTiO₃*. Solid State Communications, 1975. **17**(7): p. 847-850.
151. Pintilie, L., et al., *Ferroelectric polarization-leakage current relation in high quality epitaxial Pb(Zr, Ti)O₃ films*. Physical Review B, 2007. **75**(10): p. 104103.

152. Bruncková, H., et al., *Influence of hydrolysis conditions of the acetate sol-gel process on the stoichiometry of PZT powders*. *Ceramics International*, 2004. **30**(3): p. 453-460.
153. Zhao, N., et al., *Colloidal PbS quantum dot solar cells with high fill factor*. *ACS Nano*, 2010. **4**(7): p. 3743-3752.
154. Moreels, I., et al., *Size-dependent optical properties of colloidal PbS quantum dots*. *ACS Nano*, 2009. **3**(10): p. 3023-3030.
155. Yang, J., et al., *A top-down strategy towards monodisperse colloidal lead sulphide quantum dots*. *Nat Commun*, 2013. **4**: p. 1695.
156. Zhang, P., et al., *Enhanced photocurrent in Pb(Zr_{0.2}Ti_{0.8})O₃ ferroelectric film by artificially introducing asymmetrical interface Schottky barriers*. *Materials Chemistry and Physics*, 2012. **135**(2-3): p. 304-308.